Copy 592

[redacted] NASA TM X-111

X62-~~[illegible]~~
71935

NASA TM X-111

[redacted]

TECHNICAL MEMORANDUM

X-111

FORCE, MOMENT, AND FLOW-FIELD CHARACTERISTICS OF TWO WING-BODY-NACELLE COMBINATIONS AT MACH NUMBERS 2 AND 3

By William A. Hill, Jr.

Ames Research Center
Moffett Field, Calif.

N65 12691 (ACCESSION NUMBER)
(THRU)
92 (PAGES)
1 (CODE)
(NASA CR OR TMX OR AD NUMBER)
01 (CATEGORY)
FACILITY FORM 602

DECLASSIFIED - EFFECTIVE 1-15-64
Authority: Memo Geo. Drobka NASA HQ.
Code ATSS-A Dtd. 3-12-64 Subj: Change
in Security Classification Marking.

Hard copy (HC) $3.15
Microfiche (MF) $0.75

X-703

[redacted]

NATIONAL AERONAUTICS AND SPACE ADMINISTRATION

WASHINGTON January 1960

[redacted]

1E

DECLASSIFIED

[redacted]

DECLASSIFIED - EFFECTIVE 1-15-64
Authority: Memo Geo. Drobka NASA HQ.
Code ATSS-A Dtd. 3-12-64 Subj: Change
in Security Classification Marking

NATIONAL AERONAUTICS AND SPACE ADMINISTRATION

TECHNICAL MEMORANDUM X-111

FORCE, MOMENT, AND FLOW-FIELD CHARACTERISTICS OF TWO WING-BODY-NACELLE COMBINATIONS AT MACH NUMBERS 2 AND 3*

By William A. Hill, Jr.

A
1
7
6

SUMMARY

12691

Flow-field data and force and moment coefficients of wing, body, and engine nacelle combinations were obtained at angles of attack up to 23° and angles of sideslip of 0° and 5°. The Reynolds numbers, based on body length, were 5.9 and 10.4 million for the flow and force data, respectively. Two cylindrical bodies of fineness ratio 10 were employed. One, combined with an aspect-ratio-3/8 wing, had a tangent-ogive nose of fineness ratio 3, and the other, combined with an aspect-ratio-1 wing which extended to the body apex, had a Newtonian minimum-drag nose of fineness ratio 5. The engine nacelle, which was attached above or below the bodies, consisted of a straight-through duct of circular cross section. The length of the nacelle was 48 percent of the length of the bodies, and the maximum diameter of the nacelle was 80 percent of the diameter of the bodies.

The results of the investigation show that placement of the engine nacelle above or below the wing-body combinations provided an increase in directional stability, decreased the maximum lift-drag ratios by approximately 5 percent, and increased the minimum-drag coefficients by 15 to 20 percent. Fairly good estimates of these effects of the nacelle were obtained by available theory. A favorable engine inlet location for both models was on the windward side of the bodies and between 4 and 5 body diameters from the apex of the nose. At angles of attack corresponding to maximum lift-drag ratio this location resulted in a 20-percent increase in average dynamic pressure and a 0.25 decrease in average Mach number over the inlet face compared with free-stream conditions.

The shape of the body-alone nose shock in the vertical plane of symmetry can be predicted for the angle-of-attack case with generally good accuracy by a simple extension of the zero-angle-of-attack results

---

*Title, Unclassified

[redacted]

[redacted]

of NACA TN 4167. Good estimates of the flow-field characteristics for the windward side of the bodies alone in the vertical plane of symmetry are obtained by the generalized shock expansion method of NACA TN 3349 and by an approximate method developed herein.

INTRODUCTION

For proper placement of an air-breathing engine on a supersonic aircraft, a knowledge of the effects of the mutually interfering flow fields of engine and airframe is necessary. The flow conditions at the engine inlet which directly affect the engine's performance vary with the position of the inlet in the flow field of the airframe. In turn, engine nacelle location affects the external aerodynamic characteristics of the airframe. The problem is thus to place the engine in such a position that the most desirable characteristics of both engine and airframe are achieved. Experimental characteristics of a wide variety of airframe and airframe-engine combinations are available in the literature. This information, however, includes little experimental flow-field data. An objective of the present study, therefore, is to provide experimental data on flow fields about wing, body, and engine nacelle combinations having triangular wings of aspect ratios 3/8 and 1. An additional objective is to determine the principal effects of aerodynamic interaction between engine nacelle and airframe. Also, comparison of the results with theory is made.

SYMBOLS

Coefficients are referred to body axis.

A	reference area, $\frac{\pi d^2}{4}$
a,h,x	survey coordinates (see fig. 2(b))
C_D	drag coefficient, $\frac{D}{q_\infty A}$
C_L	lift coefficient, $\frac{L}{q_\infty A}$
C_m	pitching-moment coefficient, $\frac{\text{pitching moment}}{q_\infty Ad}$
C_n	yawing-moment coefficient, $\frac{\text{yawing moment}}{q_\infty Ad}$

[redacted]

[redacted]

C_Y	side-force coefficient, $\frac{\text{side force}}{q_\infty A}$
D	drag (excluding base drag)
d	diameter of body
f_n	fineness ratio, length/diameter
L	lift
$\left(\frac{L}{D}\right)_{max}$	maximum lift-drag ratio
M	local Mach number
p_p	local pitot pressure
$\frac{p_p}{p_{p_\infty}}$	pitot-pressure ratio
q	local dynamic pressure
r	radius of body
α	angle of attack, deg
α'	local angle of attack, deg
β	angle of sideslip, deg
β'	local angle of sideslip, deg

A176

Subscript

∞	free-stream conditions

APPARATUS AND PROCEDURE

Wind Tunnels

The investigation was conducted in the Ames 1- by 3-foot supersonic wind tunnels nos. 1 and 2. Force and moment measurements were made in the no. 2 tunnel and flow surveys in the no. 1 tunnel. Tunnel no. 1 is a closed-circuit, variable-pressure, continuous-operation type with a

[redacted]

[redacted]

Mach number range from 1.4 to 4.0. Tunnel no. 2 is a nonreturn, variable-pressure intermittent-operation type and has a Mach number range from 1.4 to 3.8. The Mach number of either tunnel can be changed by varying the contour of flexible steel plates which form the upper and lower walls of the tunnel.

Models and Instrumentation

The geometric details of the models investigated are presented in figure 1(a). Two cylindrical bodies of over-all fineness ratio 10 were employed. One, designated B_1, had a tangent-ogive nose of fineness ratio 3, and the other, designated B_2, had a 3/4 power or approximate Newtonian minimum-drag nose of fineness ratio 5. Wing-body combination B_1W_1 was composed of the two halves of a triangular wing of aspect ratio 3/8 attached to the cylindrical portion of B_1. This model, without an engine nacelle, was one of a series of low-aspect-ratio missile-type configurations which had previously demonstrated desirable stability characteristics (ref. 1). Model B_2W_2 had a triangular wing of aspect ratio 1 attached to B_2 such that the leading edge of the wing extended to the nose apex. This model was designed to represent a long-range aircraft capable of developing a relatively high lift-drag ratio. The wing sections of the models were flat plates with leading and trailing edges beveled and rounded. The engine nacelle, which could be attached either above or below the bodies alone or the body-wing combinations, consisted of a straight-through duct of circular cross section. The shape of the nacelle was designed from engine performance analyses of references 2 and 3 for a ram-jet engine operating at a Mach number of 3 with an inlet recovery factor of 0.75. The ratio of nacelle inlet to base diameter was 0.728 and the ratio of nacelle length to base diameter was 6. The base diameter was 0.8 of the body diameter. For model B_2W_2N the ratio of inlet area to total plan area (0.0126) corresponded to that typical for a long-range interceptor missile. A view of model B_2W_2N is shown in the photograph of figure 1(b). All of the models were sting supported from the rear.

The flow survey apparatus is depicted in figure 2(a). The basic measuring instrument consisted of a rake of three cone-cylinders having included angles of 40° (see figs. 2(b) and (c)). Each cone was machined from brass with a diameter of 0.130 inch. Four equally spaced static-pressure orifices were located on the surface of each cone and a pitot-pressure orifice was located at each apex. The cones were oriented about their axes so that the centers of the opposed static-pressure orifices were in horizontal or vertical planes. The axes of the cones were parallel with the body axis and pitched and rotated with the model. The center cone was positioned in the vertical plane of symmetry of the models and the outboard cones were located symmetrically with respect to the center cone and in vertical planes 1.06 body radii outboard from the vertical

[redacted]

[redacted]

plane of symmetry. Vertical and horizontal positioning of the cones was provided by moving the rake vertically with respect to the cylindrical support tube or by extending the support tube horizontally with respect to the model.

Tests

Force tests.- Lift, drag, and pitching moment at $\beta = 0^\circ$ and side force and yawing moment at $\beta = 5^\circ$ were measured at angles of attack up to 23°. The Mach numbers were 1.97 and 2.94, and the Reynolds number, based on body length, was 10.4 million. Static pressures at the base of the bodies and the base of the nacelle were recorded. Data were obtained with the nacelle above and below the body.

Flow surveys.- Local values of pitot pressure, Mach number, and angles of attack and sideslip (see fig. 3) were obtained in the flow fields below models B_1, B_1W_1, B_2, and B_2W_2 at a Mach number of 2.95 and a Reynolds number, based on body length, of 5.9 million. The measurements were made at 3, 5, and 9 diameters from the nose apex (see fig. 2(b)). The angle-of-attack range was -15° to +15° for $\beta = 0^\circ$ and 5°. Because of possible effects of local variations in tunnel stream angle as well as inaccuracies in the alinement of the cones with respect to the models local flow angles were obtained by taking differences between values measured with and without the models present.

A check on the possibility of interference between adjacent cones was made at all the test angles and without a model present by obtaining data with and without the center cone present. Comparison of data measured by the two outboard cones for both cases showed no influence of the pressure field of the center cone on the two outboard cones.

Vapor screen tests.- Tests employing the vapor screen method (for a description of this technique see ref. 1) were made for models B_2 and B_2W_2 at $M_\infty = 2.95$. With the models at approximately 15° angle of attack and 0° and 5° angle of sideslip, vortex patterns were photographed with a camera mounted inside the wind tunnel and downstream from the base of the models. For models B_1 and B_1W_1, photographs of the vortex patterns at $\alpha = 15^\circ$ were obtained from reference 1 for a Mach number of 3.3. (In ref. 1, model B_1W_1 with a second wing in the vertical plane is designated B_1W_3 and the vortex patterns are shown for this cruciform arrangement.)

[redacted]

[redacted]

Data Reduction

<u>Force tests</u>.- The force and moment data obtained from balance measurements have been reduced to coefficient form and are referred to the area and diameter of the body base. The drag coefficients were adjusted to a condition of free-stream static pressure on the base of the body and the base of the nacelle when the nacelle was present. The internal drag coefficient of the nacelle was subtracted from the measured drag coefficients of the models with nacelles. The internal drag coefficient was calculated as that due only to a skin friction force on the inside surface of the nacelle. It was assumed that a condition of turbulent boundary-layer flow existed over the entire nacelle surface. A substantiation of this approach was obtained at $\alpha = 0^\circ$ by finding that the experimental drag of the nacelle and supporting strut was equal to the sum of the calculated turbulent skin friction drags of the strut and the inside and outside surfaces of the nacelle (external wave drag was negligible). The internal drag coefficient calculated on this basis was 0.034 at $M_\infty = 1.97$ and 0.027 at $M_\infty = 2.94$. The contribution of the internal flow to the measured pitching and yawing moments was negligible.

<u>Flow surveys</u>.- Cone static and pitot pressures measured in the flow fields of the models were reduced to pitot-pressure ratio (p_p/p_{p_∞}), Mach number, and local angles of attack and sideslip from calibrations made of the cones. The effects of Mach number on the calibrations were determined from measurements of the cone characteristics at free-stream Mach numbers of 1.77, 2.43, 2.95, and 3.88.

Regarding the cone calibrations, the following remarks should be made. The only extensive published data of experimental characteristics of cones at large angles of attack are those of reference 4 for the Mach number range 1.72 to 2.43. Those cones and the ones of the present investigation were similar in that both had 40° included angles. However, the two sets of cones did differ in several respects. The diameter of the present cones was less than half the diameter of the cones of reference 4. Also, the orifices of the present cones were 30 percent larger in terms of cone diameters, and the static-pressure orifices were 30 percent closer to the pitot-pressure orifice in terms of orifice diameters.

Comparison of the characteristics of the two sets of cones at similar Mach numbers showed no effects of their differences in geometry on the calibration curves for determining stream angle or pitot-pressure ratio. The only important difference between the two calibrations was in the determination of Mach number at zero inclination by the ratio of surface static pressure to pitot pressure. The present calibration of smaller cones agreed with cone theory (obtained from tables and charts of ref. 5),

[redacted]

[redacted]

whereas, the calibration of reference 4 showed agreement with theory only at $M = 1.72$, and at higher Mach numbers gave indicated Mach numbers somewhat larger than theory.

The calculation of Mach number for flow inclinations other than zero was accomplished by an iterative procedure as suggested in reference 4. This was necessary since the ratio of average static pressure to pitot pressure depends on the inclination of the local flow with respect to the cone axis. This dependence is negligible at low Mach numbers, but at $M_\infty = 2.4$ it is important and it was found to increase in importance as the Mach number was increased above 2.4.

A check to determine any effects of Reynolds number on the cone calibrations was made at $M_\infty = 2.95$. Calibration data were obtained at Reynolds numbers per inch of 0.11, 0.22, and 0.46 million (the latter corresponded to the Reynolds number at which the flow surveys were made). The calibrations were found to be identical at the three Reynolds numbers.

Precision

The total uncertainties in the force and moment coefficients were determined from estimated uncertainties in the measurements of the forces and moments, repeatability of the data, and estimated effects of tunnel stream asymmetry determined from comparisons of data measured at positive and negative angles of attack. The maximum estimated uncertainties are listed as follows:

Coefficient	Uncertainty
C_L	±0.10
C_m	±0.20
C_D	±0.02
L/D	±0.20
C_Y	±0.10
C_n	±0.20

The accuracy in measuring angles of attack and sideslip is within ±0.1°. The variation in free-stream Mach number in the region occupied by the models was less than ±0.01 at $M_\infty = 1.97$ and ±0.02 at $M_\infty = 2.94$.

The estimated uncertainties in the flow survey data were determined from the individual uncertainties in the measurements of the cone static and pitot pressures, angles of attack and sideslip, and the estimated accuracy of the cone calibrations. The maximum uncertainties are shown below.

[redacted]

[redacted]

Quantity	Uncertainty
p_p/p_{p_∞}	±0.02
M	±0.03
α',β'	±0.2°
α,β	±0.1°

RESULTS

Lift, drag, and pitching-moment coefficients, and lift-drag ratio at $\beta = 0^\circ$, and side-force and yawing-moment coefficients at $\beta = 5^\circ$ are presented as functions of angles of attack in figures 4 to 9 for Mach numbers of 1.97 and 2.94. Data for the models with nacelle are shown for the nacelle mounted above and below the bodies. Local values of pitot-pressure ratio, Mach number, and angles of attack and sideslip measured in the flow fields of the models are presented in figures 10 to 23 for a Mach number of 2.95. For convenience of presentation and discussion, these latter results are presented as applying to the region below the models, and therefore are shown at both positive and negative angles of attack. However, if the reader desires to consider the models inclined only at positive α, as in the case of the force data, then the negative-angle data may be interpreted as applying to the region above the models. Schlieren and vapor-screen photographs of the flow-fields are included in figures 24 and 25. Comparisons of inlet flow conditions provided by the models are presented in figures 26 and 27. Figures 28 and 29 present comparisons between theory and experiment of the flow characteristics of the bodies alone. Table I is an index to the basic data figures.

DISCUSSION

Force and Moment Characteristics

Lift.- Placing a nacelle above or below the bodies alone increased the lift by about the same amount (figs. 4 and 5) for angles of attack up to 10°. This result indicates interference effects between body and nacelle were either compensating or negligible at these angles of attack. In this same range of angles, the figures show that the value of the nacelle lift increment is approximately that calculated by slender-body theory neglecting cross-flow separation effects on the nacelle (see ref. 6). It is of interest to note that the ratio of the lift coefficient of the nacelle alone to that of the body alone, as calculated by slender-body theory, is 0.98. However, this value is realized experimentally only at very low angles of attack where cross-flow separation effects are

[redacted]

small. Although not fully understood, the addition of wings to the bodies and nacelle tended to reduce or cancel the additional lift of the nacelle obtained with the body-nacelle configurations.

Pitching moment.- Pitching-moment coefficient (figs. 4 and 5) is presented with respect to the reference locations shown in figure 1(a). These positions give a static stability margin of 10 percent of the body diameter at a Mach number of 2.94 for each wing-body combination.

At $\alpha = 0^\circ$ a nonzero pitching-moment coefficient is shown by all configurations with nacelle. The nacelle below produced a negative increment in pitching moment, and the nacelle above, a positive increment. Both nacelle drag and aerodynamic interference between nacelle and body and nacelle and wing contribute to this moment increment. For the body-nacelle combinations these increments are approximately constant throughout the angle-of-attack range. However, for the wing-body-nacelle combinations, it can be seen that the increments approximately doubled between $\alpha = 0^\circ$ and 10° when the nacelle was above the body; whereas, when the nacelle was below the body the increments decreased to zero, generally at about $\alpha = 10^\circ$.

Drag and lift-drag ratio.- At $\alpha = 0^\circ$ the increase in drag coefficient (figs. 6 and 7) due to the addition of the nacelle was approximately 0.03 in all cases, or about 15 to 20 percent of the minimum-drag coefficients of the body-wing models. This value corresponds to the theoretical value for a condition of turbulent boundary-layer flow over almost the entire nacelle surface. While only this indirect indication was obtained of the condition of the boundary layer over the nacelle, direct methods were employed to determine the type of boundary-layer flow over the bodies and wings at $\alpha = 0^\circ$. Sublimation tests of B_1 and B_1W_1 showed at $M_\infty = 1.97$ and 2.94 that laminar flow existed for about 4-1/2 diameters downstream of the nose apex. On the wings, however, complete turbulent boundary-layer flow existed. Sublimation tests of B_2 at $M_\infty = 2.94$ (ref. 7) and comparison of force data for fixed and natural transition on B_2W_2 at $M_\infty = 1.97$ and 2.94 showed that laminar flow existed over only a small portion near the body apex.

For all models the variation of drag coefficient with angle of attack is essentially that given by $C_L\alpha$.

The change in maximum lift-drag ratios due to the addition of the nacelle to the bodies alone was, in general, small and indicates that the nacelle was as efficient a lifting device as the body. For the body-wing-nacelle combinations $(L/D)_{max}$ was reduced by approximately 5 percent because of the addition of the nacelle. This value is slightly less than would be calculated using experimental body-wing data plus a 0.03 increment in drag coefficient due to the nacelle.

[redacted]

[redacted]

Side force and yawing moment.- With the models at angle of sideslip the effect of the nacelle at the rear of the body is similar to that of a vertical stabilizer in providing directional stability; and as for a vertical stabilizer significant effects of model geometry would be expected.

Comparisons of the data for the combinations with and without a nacelle (figs. 8 and 9) show that at $\alpha = 0^\circ$ the side-force coefficient was increased by an amount approximately three times the value of the side-force coefficient of the body alone by adding the nacelle either above or below the body. This increment produced a stabilizing yawing moment which, for the body-nacelle combinations, was only slightly dependent on angle of attack and generally independent of nacelle location. This latter effect is interesting in that it indicates negligible adverse interference from body vortices for the nacelle located above the body. The effectiveness of a vertical tail in this location, on the other hand, is generally decreased by body vortex interference. For the combinations with wings, however, significant effects of both angle of attack and nacelle location on the yawing-moment increment are shown. The loading on the nacelle when located above the body was decreased by the wing-generated expansion field, and resulted in a decreasing positive yawing-moment coefficient with increasing angle of attack. When the nacelle was located below the body the opposite effect occurred as a result of the high dynamic pressure and low Mach number field created by the wing. These effects were more pronounced at the higher Mach number and for model B_2W_2N which had a larger wing relative to the body than model B_1W_1N.

The theoretical values of side-force and yawing-moment coefficients appearing in the figures were calculated by the method employed in reference 8 for predicting the contribution of vertical tails to the characteristics in yaw of various wing-body-tail configurations. For the present calculations it was assumed that the nacelle and supporting strut could be represented by a vertical tail surface. The side force of the assumed tail of the same total height as the nacelle and strut was calculated by slender-body theory and then modified by a factor to account for body-tail interference (see ref. 8). Except for the relatively small internal component of side force on the nacelle lip, the side force was arbitrarily assumed to act at the centroid of volume of the strut and nacelle (1.55 d forward of nacelle base). Effects of angle of attack and nacelle location were assumed due only to the presence of the wing and were obtained by multiplying the calculated values of side force and yawing-moment increments for $\alpha = 0^\circ$ by the expression $1 + \left\{\frac{q/q_\infty}{[(M^2-1)/(M_\infty^2-1)]^{1/2}}\right\} K$ (ref. 8). The factors without subscripts in the bracket refer to average local conditions in the region occupied by the nacelle and were obtained by a two-dimensional expansion or compression of the free-stream flow through the

[redacted]

angle α. The factor K is a correction for wing plan form and is equal to the linear theory ratio of loading coefficient at the root chord of the wing to loading coefficient for a two-dimensional wing. The calculated increments in side-force and yawing-moment coefficients were added to the corresponding experimental coefficients of the body alone and body-wing combinations to obtain the total coefficients of the configurations with nacelle.

Generally, good agreement between theory and experiment is shown by the comparison of side-force coefficients. Comparison of yawing-moment coefficients shows that the predicted variations with angle of attack are generally in accordance with the experimental trend. At $\alpha = 0^{\circ}$, however, experiment shows that the center of side loading increment moved forward with increase in free-stream Mach number, whereas, in the theory it was assumed to remain stationary.

A176

Details of Flow Fields About the Models

Vertical plane of symmetry, $\beta = 0^{\circ}$.- Figures 10 through 12 present local pitot-pressure ratio, Mach number, and angle of attack as functions of survey location and angle of attack for a free-stream Mach number of 2.95. The filled symbols represent the flow quantities just behind the nose shock as obtained from the experimental local slope of the shock wave (fig. 24) and the two-dimensional oblique shock relation for $M_\infty = 2.95$. The precision in determining these values, which are considered valid data points, equalled that of the physically measured quantities.

At Mach numbers above 2 the ratio of local pitot pressure to free-stream pitot pressure (p_p/p_{p_∞}) may, for all practical purposes, be assumed equivalent to the ratio of local dynamic pressure to free-stream dynamic pressure. Between $M_\infty = 2$ and 3 these ratios will differ by no more than 4 percent. From the viewpoint of increasing engine thrust, a high dynamic pressure and therefore a high value of pitot-pressure ratio at the engine inlet is desirable. For models B_1 and B_1W_1 (fig. 10(a)), the highest values of pitot-pressure ratio occurred near the nose shock. Downstream of the shock the attenuating effect of the expansion field generated by the ogive nose is shown at positive α to extend for approximately one nose length (three diameters). Increases in positive α resulted in significant increases in pitot-pressure ratio above 1, and are evident as approximately constant displacements of the pitot-pressure ratio curves by amounts equal to the increases in pitot-pressure ratio at the shock. In contrast, at negatives angles of attack the pitot-pressure ratio was generally below 1 and showed only small effects of changes in α and h/r. The effect of the wing is indicated at $x/d = 9$ by a slight increase in pitot-pressure ratio over that of the body alone at positive α and a slight decrease at negative α.

[redacted]

The data of models B_2 and B_2W_2 (fig. 10(b)) reflect again the dominating influence of the body nose. In this case, the slender Newtonian nose produced only a slight change in pitot-pressure ratio downstream of the nose shock. The effect of the expansion field about the body shoulder (see fig. 24) resulted in a decrease in pitot-pressure ratio in the region between 5 and 9 diameters from the nose apex. Comparison of the data for the two models (see also fig. 26) shows that the aspect-ratio-1 wing extended to the nose apex of the body increased the strength of the body-nose shock. Downstream of the shock at $\alpha = 10^\circ$ and 15° the pitot-pressure ratio for the body-wing model was about 0.10 larger at $x/d = 5$ and 0.20 larger at $x/d = 9$ than that for the body alone. At negative angles of attack, however, the expansion field of the wing caused a significant decrease in pitot-pressure ratio below free-stream conditions with increasing distance from the nose apex.

The trends shown by the local Mach number and angle-of-attack data of figures 11 and 12 are, in general, the inverse of those discussed above for pitot-pressure ratio. Thus, for models B_1 and B_1W_1, large positive longitudinal gradients in M and α' occurred downstream of the nose shock. In this same region the data of models B_2 and B_2W_2 exhibit only small gradients in M and α' except for conditions of large negative angles of attack and locations near the body.

Outboard vertical plane, $\beta = 0^\circ$.- Data obtained in the two outboard vertical planes at $\beta = 0^\circ$ are compared in figures 13 to 15 with data at corresponding locations in the vertical plane of symmetry. The comparisons are made for locations which are approximately the same radial distance from the body axis (see fig. 2(b)).

At positive angles of attack these comparisons are assumed to show directly the variation in the flow quantities over the spanwise distance between the outboard planes and plane of symmetry. At negative angles, however, the results are interpreted with regard to the vortex positions indicated by the photographs of figures 24-25, for it is well known that extremely nonlinear spanwise variations in the flow characteristics will be measured when a survey traverses close to or through the center of a vortex (ref. 12). These photographs show that the vortex locations were significantly affected by changes in model geometry. For example, addition of wings to the bodies tended to move the vortex centers down and outboard. This is particularly evident for model B_2W_2 at $x/d = 9$. The wings, in this case, provide a vortex-free region for an engine inlet located on the leeward side of the body.

Except for the survey location closest to the body $(h/r = 1.6)$, pitot-pressure ratio and Mach number (figs. 13-14) measured in the outboard plane were not greatly different from those in the plane of symmetry. At the closest location in the outboard plane pitot-pressure ratio was decreased and Mach number increased with respect to the values in the plane of symmetry.

[redacted]

Comparisons of angle-of-attack data in the two planes (fig. 15) show that at both $h/r = 2.16$ and 1.60 the local angle of attack in the outboard plane was generally higher at positive α and lower at negative α than the corresponding local angle of attack in the plane of symmetry. On the leeward side of the wing-body models (negative α) at $x/d = 9$ the data show the effects of an outboard movement of the body vortices. At this location large differences between the local angles of attack in the two planes are indicated for B_1 and B_2, whereas only small differences are indicated for B_1W_1 and B_2W_2.

Local sideslip angles measured in the outboard vertical plane are presented in figure 16. The data are shown as applying to the left outboard plane. Positive angles represent flow away from the body axis, and negative angles, flow toward the axis (see fig. 3(b)). At positive α only slight effects of model geometry on local sideslip angle are apparent. The largest effects of α are shown for the location closest to the body. At large negative α, the effects of the vortices on β', as influenced by model geometry, are similar to those discussed above for local angle of attack.

A176

Vertical plane of symmetry and outboard planes, $\beta = 5^\circ$.- For the vertical plane of symmetry, figures 17 to 19 show that local pitot-pressure ratio, Mach number, and angle of attack were generally unaffected by changes in β from 0° to 5°.

Changes in local sideslip angle which occurred with changes in β throughout the α range are shown in figure 20. In this case the net change in sideslip angle due to $\beta = 5^\circ$ is plotted. The data are presented both for the vertical plane of symmetry and the outboard vertical planes. Between $\alpha = 15^\circ$ and -5° each survey location experienced a change in sideslip angle which is approximately the same as or somewhat larger than the 5° change in β. At $\alpha = -15^\circ$, however, the change in sideslip angle varied considerably with location. This apparently was associated with the vortices being asymmetrically arranged with respect to the vertical plane of symmetry, as shown in figure 25 for model B_2W_2.

Local pitot-pressure ratio, Mach number, and angle of attack measured in the outboard vertical planes at $\beta = 0^\circ$ and 5° are compared in figures 21 to 23. For all models at positive α, the pitot pressure measured by the windward cone (right outboard plane) was increased with respect to the corresponding value for $\beta = 0^\circ$ by approximately the same increment that the pressure was decreased at the leeward cone (left outboard plane). This incremental change in pitot pressure due to $\beta = 5^\circ$ was generally uniform over the length of the models and attenuated radially in a direction away from the models. The changes in M and β' due to $\beta = 5^\circ$ are evident as the inverse of the change in pitot pressure. At negative angles of attack and between 3 and 9 diameters from the nose apex, a reversal is shown in the sign of the incremental change in pitot-pressure ratio and Mach number. This reversal probably resulted from the increase

[redacted]

in local body vorticity between these two stations. This effect is more pronounced at $\alpha = -15^\circ$ where large variations with model plan form are also indicated.

Comparisons of Inlet Conditions for the Models

In figure 26 comparisons are made to show the possible advantages or disadvantages of each of the various models over the others in providing favorable inlet conditions of high pitot-pressure ratio, low Mach number, and low local angles of attack. Comparisons are made for the vertical plane of symmetry and $\beta = 0^\circ$. The most significant differences between the models occurred on the windward side (positive α), where B_2 and, particularly, B_2W_2 provided higher values of pitot-pressure ratio, lower Mach numbers, and generally lower local angles of attack over a considerably longer portion of the afterbody than did B_1 and B_1W_1.

In figure 27 cross plots of the wing-body data in the vertical plane of symmetry are presented for several x/d stations to indicate the more favorable inlet locations on the windward side of the winged models corresponding to the condition of maximum lift-drag ratio ($\alpha \approx 10^\circ$ for B_1W_1 and $\alpha \approx 5^\circ$ for B_2W_2). Since the range in the ordinate h/r of 1.60 to 2.77 coincides with the inlet location of the nacelle in the vertical plane of symmetry, the plots thus present the local flow variation across the inlet diameter of the nacelle. The higher angle of attack necessary for B_1W_1 to achieve $(L/D)_{max}$, as compared with B_2W_2, is seen to result in both models having similar average Mach numbers and pitot-pressure ratios at the inlet plane when interference from the nose shock was absent. The intersection of the nose shock with the inlet plane is indicated at $x/d = 3$ for B_1W_1 and $x/d = 3$ and 4 for B_2W_2 by the discontinuous change in the flow parameters to free-stream values.

For conditions of maximum lift-drag ratio, high local pitot-pressure ratio, low local Mach number, and small local angles of attack, figure 27 indicates that the most favorable inlet locations are at about $x/d = 4$ for B_1W_1 and $x/d = 5$ for B_2W_2. Corresponding to these locations the average local pitot-pressure ratio is approximately 20 percent above the free-stream value of 1 and the average local Mach number is about 0.25 below free-stream Mach number 2.95. The average local angle of attack is approximately 3.5° for B_1W_1 and 0° for B_2W_2. Model B_2W_2 is shown to provide less distortion in pitot-pressure ratio and Mach number and slightly more distortion in local angle of attack over the inlet diameter than B_1W_1.

[redacted]

Comparison of Body-Alone Flow-Field Data With Theory

In this section comparisons are made between theory and experiment for the flow field in the vertical plane of symmetry at $\beta = 0^\circ$. The comparisons are restricted to the bodies alone since no methods were available for calculating the effects of the wings. The bodies, however, have been shown experimentally to contribute the dominating characteristics of the flow in the vertical plane of symmetry.

The flow-field characteristics were calculated by the generalized shock-expansion method employed by Savin in reference 9, and by an approximate method described in appendix A. Both of these methods utilize the assumption that the flow field is locally two-dimensional in nature downstream of the body apex. The generalized shock expansion method was shown by Savin to give good estimates of surface quantities and shock wave coordinates of nose shapes for hypersonic similarity parameters, M_∞/f_n, ranging from 0.6 to 1.68. Further, it was indicated that the method should give equally good results at points in the flow field between the shock and surface boundaries. The approximate method (appendix A) was devised to give a rapid estimate of the flow characteristics in the vertical plane of symmetry, and utilizes the results of Love and Long (ref. 11) in estimating shock-wave shape for the angle-of-attack case (appendix B). This method was used for both B_1 and B_2 at $\alpha = 0^\circ$, 10°, 15°, and the generalized shock expansion method was used for B_1 at $\alpha = 10^\circ$. (Since neither of the two methods accounts for effects of flow separation on the leeward side of the bodies, calculations of flow quantities were made only for the windward side.)

Shock-wave shape.- Comparisons of calculated and experimental shock-wave coordinates are presented in figure 28. For body B_1 (upper half of figure) at $\alpha = 0^\circ$, the shock obtained by the method of Love and Long follows closely the experimental shape. Similar agreement between experimental and calculated shapes is shown by the comparisons for $\alpha \neq 0^\circ$, where the calculated shapes have been obtained from equation (B2) and the generalized shock-expansion method (for $\alpha = 10^\circ$).

Shock-wave coordinates obtained for body B_2 are presented in the lower half of figure 28. The calculated curves are shown to emanate from a point slightly upstream of the apex of B_2. This point represents the apex of the circular arc nose assumed to represent the contour of B_2 in the shock-wave calculation. In determining the shape of the shock for a given nose contour, it is necessary to assume a circular arc nose tangent to the forward portion of the true contour. Since the slope of B_2 is infinite at the apex, and varies as $(x/d)^{-1/4}$, the circular arc in this case could be assumed tangent at only one point. The tangent point chosen was at 5 percent of the nose length $(x/d = 0.25)$. The resulting contour had approximately the same ordinates and slopes as the true contour up

[redacted]

to x/d of about 2. At $\alpha = 0^\circ$ very good agreement between the experimental and calculated shock-wave shapes is shown. At angles other than zero the comparisons indicate that the slope of the shock is predicted, but the position of the shock is displaced forward of the true position.

Flow-field characteristics.- Mach number and pitot-pressure ratio calculated for the vertical plane of symmetry of B_1 and B_2 are presented in figure 29. The initial point of each theoretical curve represents the value of the ordinate behind the shock. The discontinuity occurring in the curves obtained by the method of the present report is primarily a result of the assumptions of the method (see appendix A). The location of this discontinuity is dependent on the calculated position of the Mach line from the juncture of the nose and afterbody. The good agreement shown between theory and experiment, however, indicates that the region of influence of the discontinuity is small.

The theoretical curve obtained by the generalized shock expansion method for B_1 at $\alpha = 10^\circ$ is shown in figure 29 to give a lower Mach number and higher pitot-pressure ratio than those of the approximate method in a region between the shock and the Mach line from the nose-cylinder juncture. In addition, the Mach line is indicated to be inclined more to the rear. Aft of the Mach line both methods give approximately the same values of Mach number and pitot-pressure ratio.

Local angles of attack calculated by the generalized shock expansion method (no values were obtainable by the approximate method) for B_1 at $\alpha = 10^\circ$ are presented in figure 12(a). Except for the location closest to the body, good agreement with the measured angles is shown. At $h/r = 1.60$ the calculated values are higher than the experimental by several degrees. This result demonstrates a failure of the method to describe the flow field very close to the body surface.

CONCLUSIONS

Flow-field characteristics and force and moment coefficients of two triangular wing, body, and engine nacelle combinations have been obtained at Mach numbers 2 and 3. An analysis of these data has led to the following conclusions:

1. Placement of the engine nacelle above or below the wing-body combinations provided an increase in directional stability, decreased the maximum lift-drag ratios by approximately 5 percent, and increased the minimum drag coefficients 15 to 20 percent. Fairly good estimates of these effects of the nacelle were obtained by available theory.

[redacted]

[redacted]

2. A favorable nacelle inlet location for both models was on the windward side of the body and between 4 and 5 body diameters from the apex of the nose. At angles of attack corresponding to maximum lift-drag ratio this location resulted in a 20-percent increase in average dynamic pressure and a 0.25 decrease in average Mach number over the inlet face compared with free-stream conditions.

3. The shape of the body-alone nose shock in the vertical plane of symmetry can be predicted for the angle-of-attack case with generally good accuracy by a simple extension of the zero-angle-of-attack results of NACA TN 4167.

4. Good estimates of the flow-field characteristics for the windward side of the bodies alone in the vertical plane of symmetry are obtained by the generalized shock expansion method of NACA TN 3349 and by an approximate method developed herein.

Ames Research Center
National Aeronautics and Space Administration
Moffett Field, Calif., Aug. 4, 1959

[redacted]

[redacted]

APPENDIX A

APPROXIMATE METHOD FOR CALCULATING MACH NUMBER AND PITOT-PRESSURE RATIO IN FLOW FIELD ON WINDWARD SIDE OF BODY IN VERTICAL PLANE OF SYMMETRY,

$\beta = 0^\circ$

Outline of Method

Consider an axisymmetric nose and cylindrical afterbody combination inclined at an angle α to a supersonic stream (sketch (a)). The shock

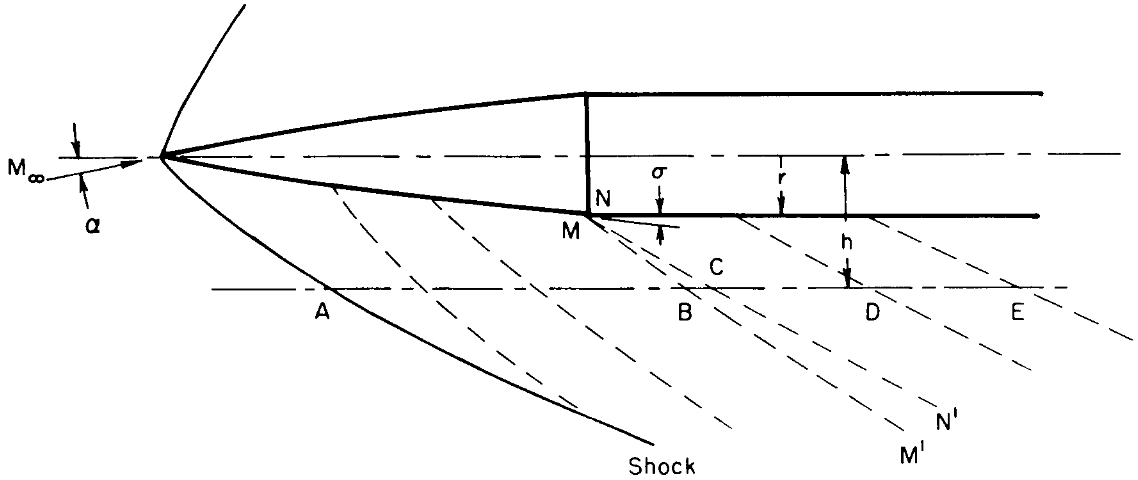

Sketch (a)

wave attached to the nose apex and Mach lines in the flow field on the windward side are shown schematically. Line AE is drawn parallel to the body axis. Angle σ defines the local turning angle at the juncture of the nose and afterbody; thus when $\sigma = 0$, MM' = NN'. In the approximate method developed herein the local Mach number along line AE is assumed to vary linearly between A and B, B and C, C and D, etc. Effects of any turning of the flow between A and B are neglected. Hence, calculation of the flow Mach number is dependent on calculation of the Mach number immediately downstream of the shock and at each of the Mach lines considered, in addition to specification of the location of the shock and

[redacted]

[redacted]

Mach lines. The shock-wave characteristics may be determined from equation (B2) in appendix B and the two-dimensional oblique shock relations. Calculation of the Mach lines is outlined as follows.

Details of the method will be presented for Mach line MM'; however, the same procedure was employed for all other Mach lines considered. A first approximation to Mach line MM' is obtained by constructing MM'' (sketch (b)), a line of constant slope, $\mu_m + \sigma$, where μ_m is the Mach

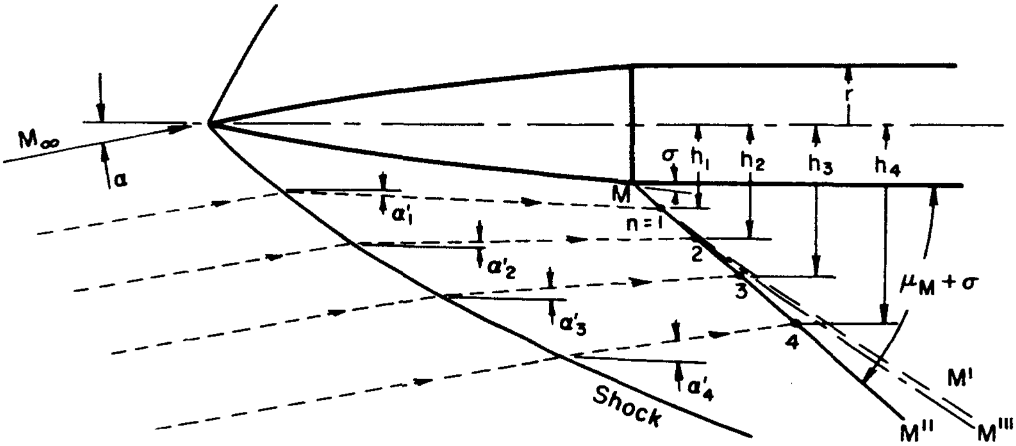

Sketch (b)

angle corresponding to the surface Mach number immediately ahead of point M (on nose). Next, approximate streamlines bent by an angle α' at the nose shock are extended from the shock at a constant inclination corresponding to α' until they intersect line MM''. Along the Mach line at each intersection point $n = 1, 2, \ldots$, the local Mach number M_n is obtained from the ratio of local static to total pressure, p_n/p_{t_n}. The local total pressure p_{t_n} is assumed constant along each approximate stream line, and the local static pressure, p_n, is approximated by applying a result of projectile theory (ref. 10) which states that the pressure coefficients, $(p_n - p_\infty)/q_\infty$, at points not near the body axis along a Mach line vary inversely with the square root of the vertical displacements of the points from the axis. The local pressure coefficient along Mach line MM'' is thus assumed to be related to its corresponding value at the surface by

[redacted]

[redacted]

$$\frac{p_n - p_\infty}{q_\infty} = \frac{1}{(h_n/r)^{1/2}}\left(\frac{p_M - p_\infty}{q_\infty}\right)$$

The pitot-pressure ratio corresponding to M_n is calculated from

$$\frac{p_{p_n}}{p_{p_\infty}} = \left(\frac{p_{p_n}}{p_{t_n}}\right)\left(\frac{p_{t_n}}{p_{t_\infty}}\right)\left(\frac{p_{t_\infty}}{p_{p_\infty}}\right)$$

A second, closer approximation to Mach line MM' may now be constructed as line MM''' (see sketch (b)) along which the flow properties calculated for line MM'' are assumed to apply. The average slope of line MM''' between two consecutive points is obtained by

$$\tan(\overline{\mu - \alpha'}) = \tan \frac{1}{2}\left[(\mu - \alpha')_n + (\mu - \alpha')_{n+1}\right]$$

In applying the above method to the models of the present investigation, at most four streamlines were employed to obtain Mach line MM'''. Sketch (b) typifies the spacing of the streamlines. In view of the approximations involved in the method, additional intermediate streamlines were considered unnecessary.

Surface Characteristics

The surface characteristics needed in the preceding flow calculations were obtained as follows. For the models at zero angle of attack surface pressures were obtained from references 15 and 16 for B_1 and B_2, respectively. At $\alpha > 0$, the pressure at the nose apex was obtained from the conical flow theories of reference 9 for B_1 and reference 13 for B_2. (For the latter case a small conical tip was assumed tangent to the true contour of B_2 at a point 5 percent of the nose length.) Pressures downstream of the apex were then obtained by a Prandtl-Meyer expansion of the surface flow. The pressures on the cylindrical afterbody of B_1 were assumed equal to the value at the nose-cylinder juncture. The pressures on the afterbody of B_2 were not obtained beyond the juncture.

[redacted]

[redacted]

APPENDIX B

METHOD FOR ESTIMATING SHOCK SHAPE IN VERTICAL PLANE OF SYMMETRY FOR NOSE AT ANGLE OF ATTACK

The method of Love and Long (ref. 11) assumes that the local ordinate of the shock attached to a pointed axisymmetric nose at zero angle of attack may be obtained from the following simple expression:

$$y = K_O \left\{ \tan \theta_O \left[ln \left(1 + \frac{x}{K_O} \right) \right] + \tan \mu_\infty \left[\frac{x}{K_O} - ln \left(1 + \frac{x}{K_O} \right) \right] \right\} \qquad (B1)$$

A
1
7
6

where

x,y coordinates of shock

K_O scale factor which relates scale of shock to scale of a circular arc tangent to forward portion of nose

$\tan \theta_O$ initial slope of shock at nose apex $(x = y = 0)$

$\tan \mu_\infty$ slope of shock at $x = \infty$ $(\mu_\infty = \sin^{-1}(1/M_\infty))$

Factor K_O, which was determined by trial and error from comparison of shock shapes calculated by equation (B1) and the method of characteristics, is presented graphically in reference 11 as a function of free-stream Mach number and nose semiapex angle.

When the nose is inclined at an angle α to the stream axis, the shape of the attached shock in the vertical plane of symmetry (see sketch (c)) becomes asymmetric with respect to the body axis. To obtain

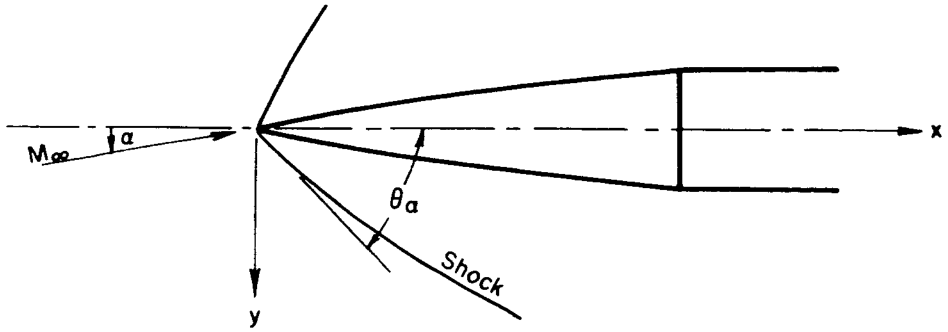

Sketch (c)

[redacted]

[redacted]

the local ordinate for this case, equation (B1) may be generalized to the form

$$y = K_\alpha \left\{ \tan\theta_\alpha \left[ln\left(1 + \frac{x}{K_\alpha}\right)\right] + \tan\left(\mu_\infty - \alpha\right)\left[\frac{x}{K_\alpha} - ln\left(1 + \frac{x}{K_\alpha}\right)\right]\right\} \tag{B2}$$

Here, factor K_α specifies the scale for a particular angle of attack. No values of K_α are available; however, in the present investigation it was found that the assumption

$$K_\alpha = K_o$$

yielded satisfactory predictions of the shock shape for the angle range, $-15^\circ \leq \alpha \leq 15^\circ$. Angle θ_α is determined from the second-order cone solutions of Stone (ref. 13) as tabulated in reference 14, or the conical flow theory of Savin developed in reference 9. The latter theory provides results over a range of cone angles and Mach numbers not treated in reference 14. For the present models, reference 9 was used for B_1 and reference 14 for B_2.

[redacted]

REFERENCES

1. Jorgensen, Leland H., and Katzen, Elliott D.: Wing-Body Combinations With Wings of Very Low Aspect Ratio at Supersonic Speeds. NACA RM A56G16, 1956.

2. Evans, Phillip J., Jr.: Analytical Investigation of Ram-Jet-Engine Performance in Flight Mach Number Range From 3 to 7. NACA RM E51H02, 1951.

3. Weber, Richard J., and Luidens, Roger W.: Analysis of Ram-Jet Engine Performance Including Effects of Component Changes. NACA RM E56D20, 1956.

4. Centolanzi, Frank J.: Characteristics of a 40° Cone for Measuring Mach Number, Total Pressure, and Flow Angles at Supersonic Speeds. NACA TN 3967, 1957.

5. Ames Research Staff: Equations, Tables, and Charts for Compressible Flow. NACA Rep. 1135, 1953.

6. Moskowitz, Barry: Approximate Theory for Calculation of Lift of Bodies, Afterbodies, and Combinations of Bodies. NACA TN 2669, 1952.

7. Jorgensen, Leland H.: Experimental Lift-Drag Ratios for Two Families of Wing-Body Combinations at Supersonic Speeds. NACA RM A58A08.

8. Kaattari, George E.: Estimation of Directional Stability Derivatives at Moderate Angles and Supersonic Speeds. NASA MEMO 12-1-58A, 1959.

9. Savin, Raymond C.: Application of the Generalized Shock-Expansion Method to Inclined Bodies of Revolution Traveling at High Supersonic Airspeeds. NACA TN 3349, 1955.

10. Whitham, G. B.: The Flow Pattern of a Supersonic Projectile. Communications on Pure and Applied Math, vol. 5, no. 3, Aug. 1952, pp. 301-348.

11. Love, Eugene S., and Long, Ronald H.: A Rapid Method for Predicting Attached-Shock Shape. NACA TN 4167, 1957.

12. Jorgensen, Leland H., and Perkins, Edward W.: Investigation of Some Wake Vortex Characteristics of an Inclined Ogive-Cylinder Body at Mach Number 2. NACA Rep. 1371, 1958.

[redacted]

13. Stone, A. H.: On Supersonic Flow Past a Slightly Yawing Cone. II. Jour. Math. and Phys., vol. XXX, no. 4, Jan. 1952, pp. 200-213.

14. Staff of the Computing Section (under the direction of Zdeněk Kopal): Tables of Supersonic Flow Around Cones of Large Yaw. Tech. Rep. no. 5, Center of Analysis, Mass. Inst. of Tech., Cambridge, Mass., 1949.

15. Rossow, Vernon J.: Applicability of the Hypersonic Similarity Rule to Pressure Distributions Which Include the Effects of Rotation for Bodies of Revolution at Zero Angle of Attack. NACA TN 2399, 1951.

16. Jorgensen, Leland H.: Correlation by the Hypersonic Similarity Rule of Pressure Distributions and Wave Drags for Minimum-Drag Nose Shapes at Zero Angle of Attack. NACA RM A53F12, 1953.

[redacted]

DECLASSIFIED [redacted]

TABLE I.- INDEX TO BASIC DATA

(a) Force Data

M_∞	β, deg	Quantity	Figure number for model			
			B_1,B_1N	B_1W_1,B_1W_1N	B_2,B_2N	B_2W_2,B_2W_2N
1.97	0	C_L,C_m	4(a)	4(a)	4(b)	4(b)
2.94	↓	C_L,C_m	5(a)	5(a)	5(b)	5(b)
1.97		C_D,L/D	6(a)	6(a)	6(b)	6(b)
2.94		C_D,L/D	7(a)	7(a)	7(b)	7(b)
1.97	5	C_Y,C_n	8(a)	8(a)	8(b)	8(b)
2.94	↓	C_Y,C_n	9(a)	9(a)	9(b)	9(b)

(b) Survey Data

M_∞	β, deg	Survey location	Quantity	Figure number for model			
				B_1	B_1W_1	B_2	B_2W_2
2.95	0	^{1}VPS	p_p/p_{p_∞}	10(a)	10(a)	10(b)	10(b)
↓	↓	↓	M	11(a)	11(b)	11(c)	11(d)
			α'	12(a)	12(b)	12(c)	12(d)
		^{2}OVP & VPS	p_p/p_{p_∞}	13(a)	13(a)	13(b)	13(b)
		↓	M	14(a)	14(a)	14(b)	14(b)
			α'	15(a)	15(a)	15(b)	15(b)
			β'	16(a)	16(a)	16(b)	16(b)
	5	VPS	p_p/p_{p_∞}	17(a)	17(a)	17(b)	17(b)
	↓	↓	M	18(a)	18(a)	18(b)	18(b)
			α'	19(a)	19(a)	19(b)	19(b)
		VPS & OVP	β'	20(a)	20(b)	20(c)	20(d)
	0 & 5	OVP	p_p/p_{p_∞}	21(a)	21(b)	21(c)	21(d)
	↓	↓	M	22(a)	22(b)	22(c)	22(d)
			α'	23(a)	23(b)	23(c)	23(d)

[1] Vertical plane of symmetry

[2] Outboard vertical plane

[redacted]

DECLASSIFIED

[redacted]

A-176

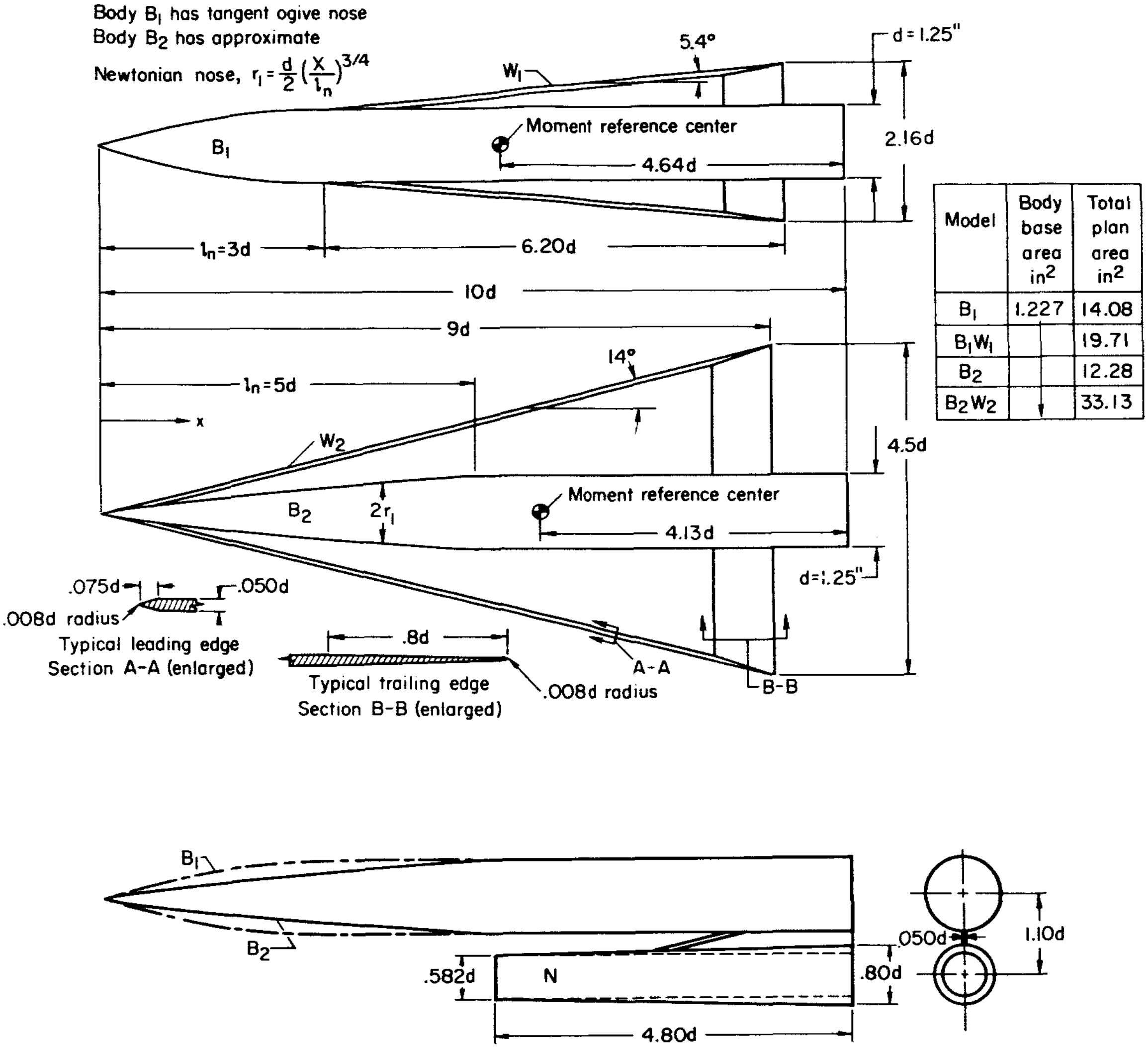

Model	Body base area in^2	Total plan area in^2
B_1	1.227	14.08
B_1W_1	│	19.71
B_2	│	12.28
B_2W_2	↓	33.13

(a) Wing-body-nacelle details.

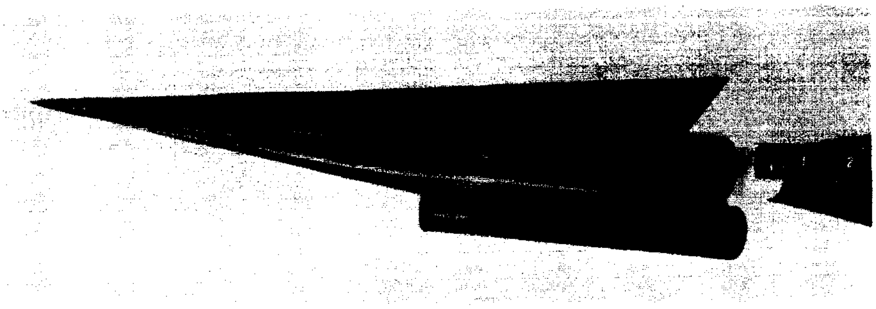

(b) View of model B_2W_2N.

Figure 1.- Model geometry.

[redacted]

[redacted]

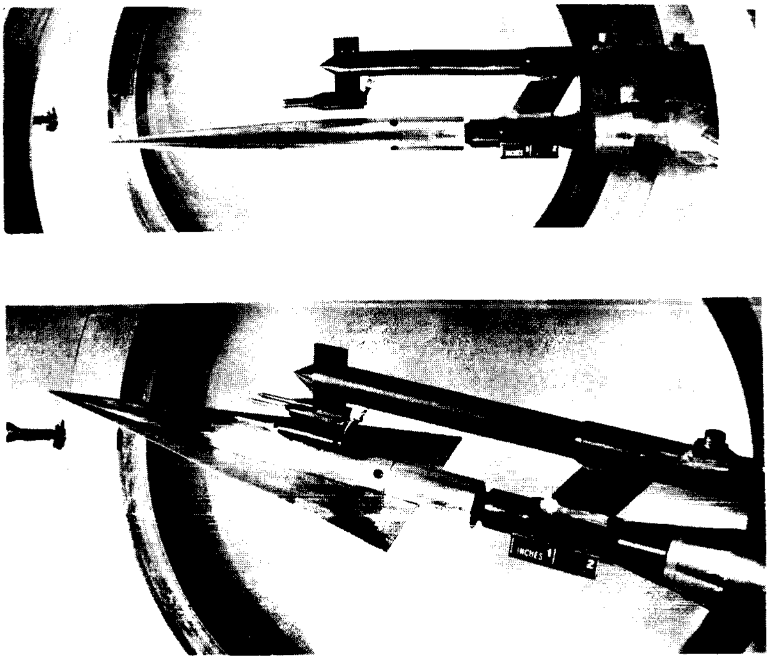

(a) Two views of survey apparatus and model B_2W_2 shown inverted in wind tunnel.

Vert. pos.	a/r	h/r
1	1.68	1.60
2	2.16	2.16
3	2.70	2.77

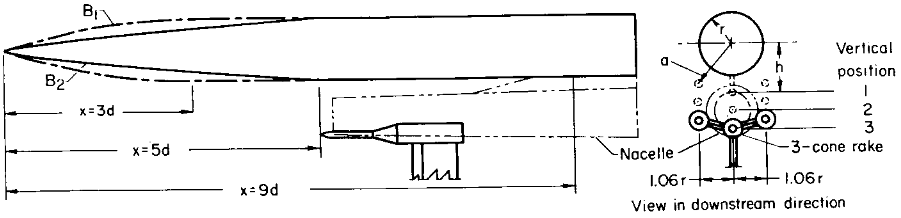

(b) Flow survey rake; horizontal and vertical locations of survey.

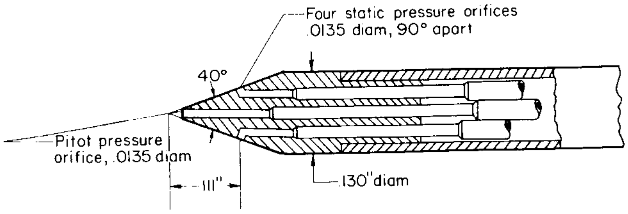

(c) Cone details.

Figure 2.- Flow survey apparatus and locations.

[redacted]

DECLASSIFIED

[redacted]

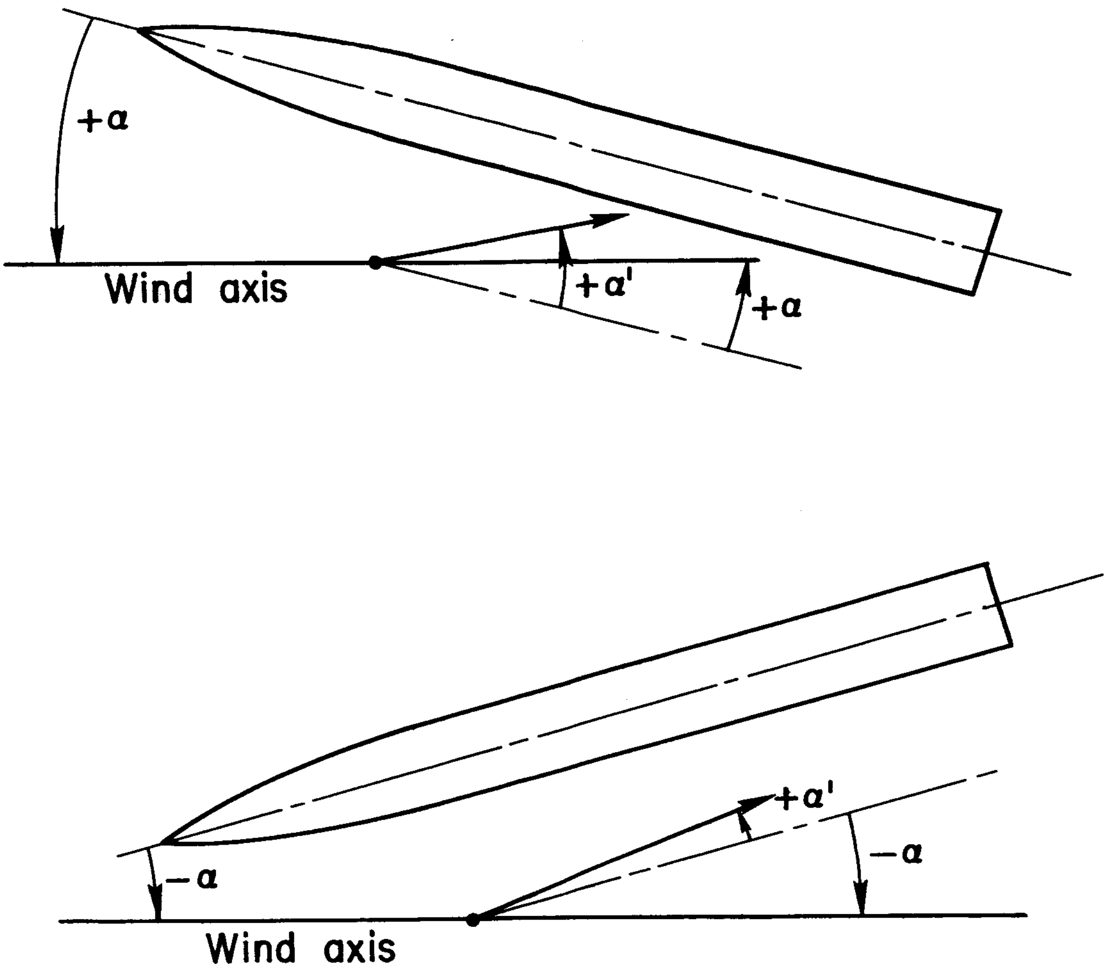

(a) Vertical plane of body.

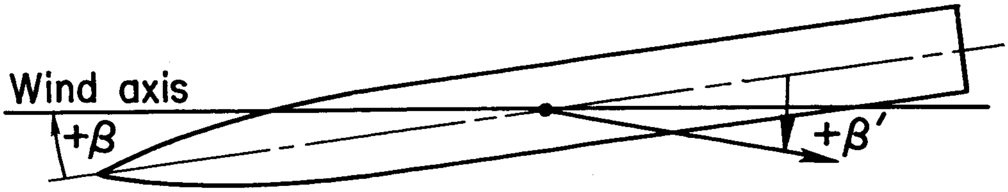

(b) Horizontal plane of body.

Figure 3.- Angle designation and sign convention of local flow vector.

[redacted]

[redacted]

[redacted]

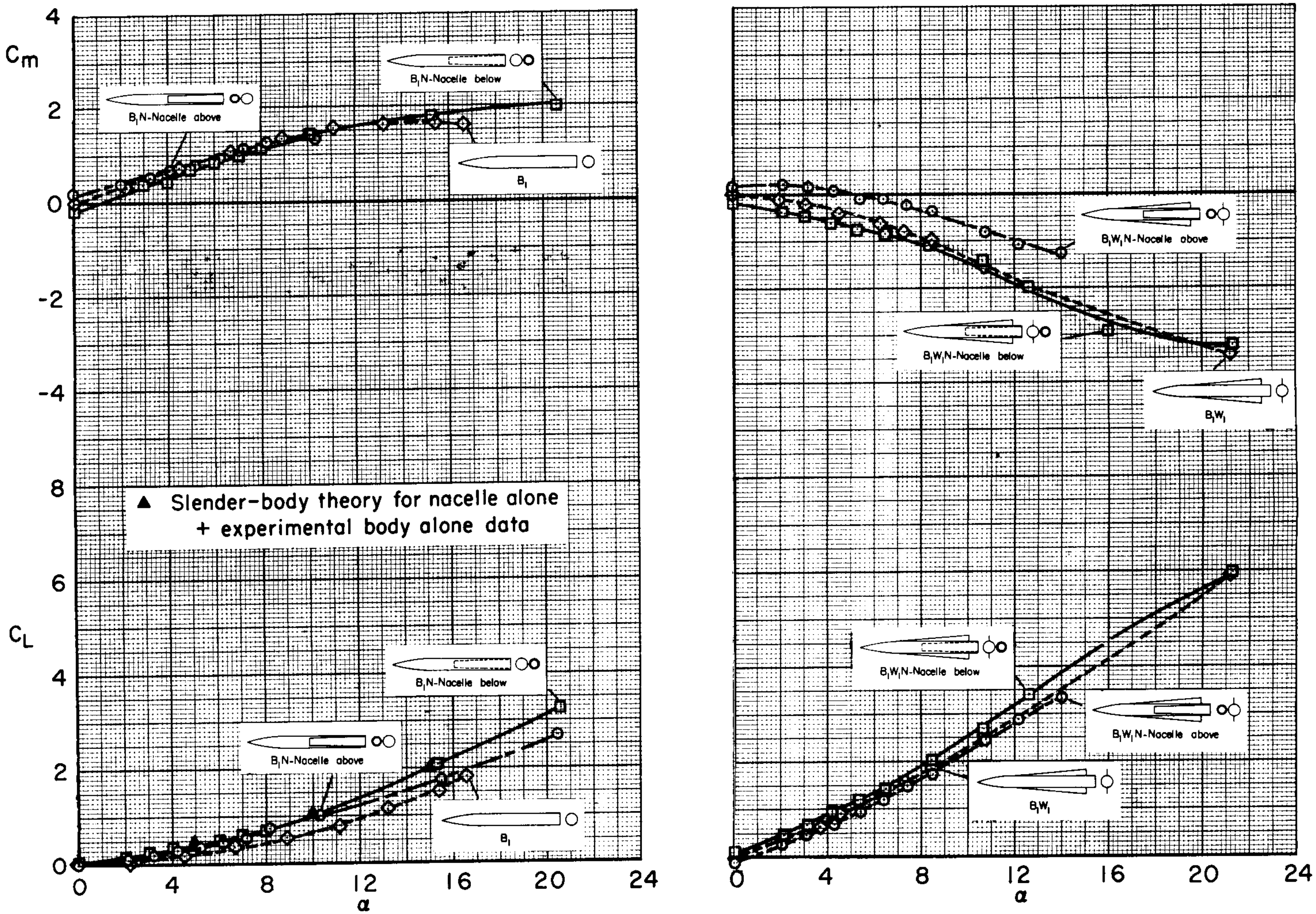

(a) B_1 and B_1N

(b) B_1W_1 and B_1W_1N

Figure 4.- Lift and pitching moment at $M_\infty = 1.97$ and $\beta = 0^\circ$.

[redacted]

[redacted]

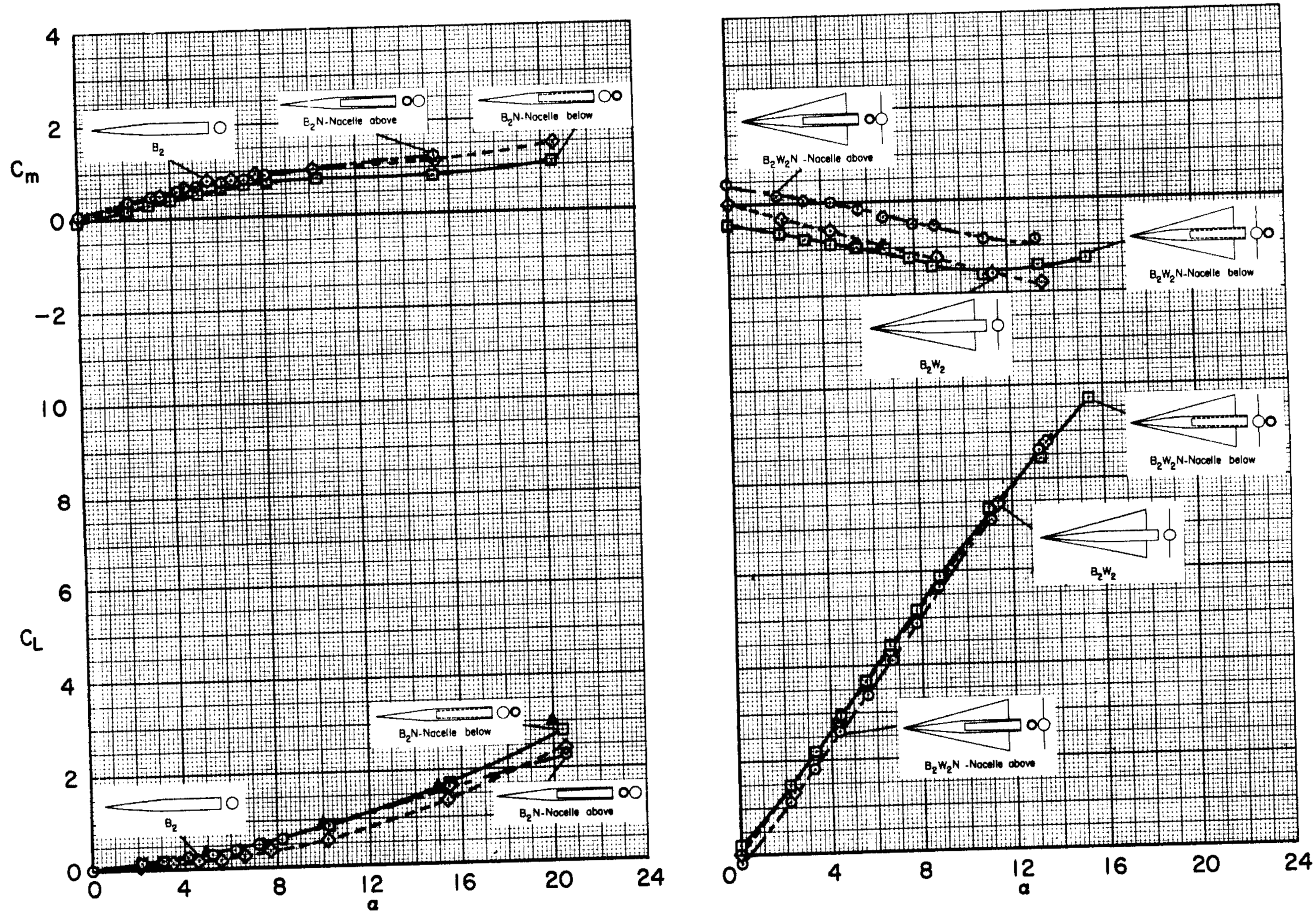

(c) B_2 and B_2N

(d) B_2W_2 and B_2W_2N

Figure 4.- Concluded.

[redacted]

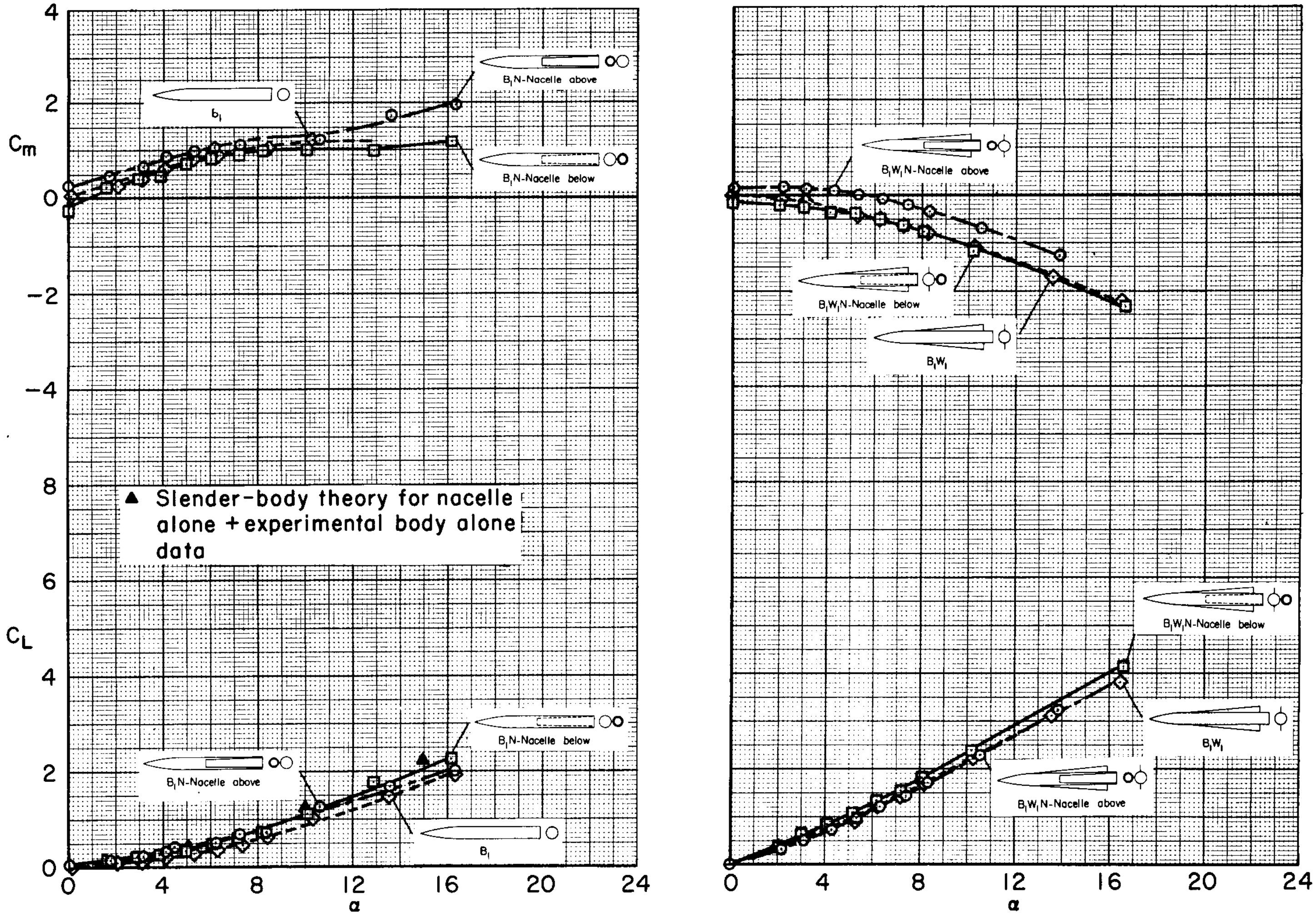

(a) B_1 and B_1N

(b) B_1W_1 and B_1W_1N

Figure 5.- Lift and pitching moment at $M_\infty = 2.94$ and $\beta = 0^\circ$.

[redacted]

[redacted]

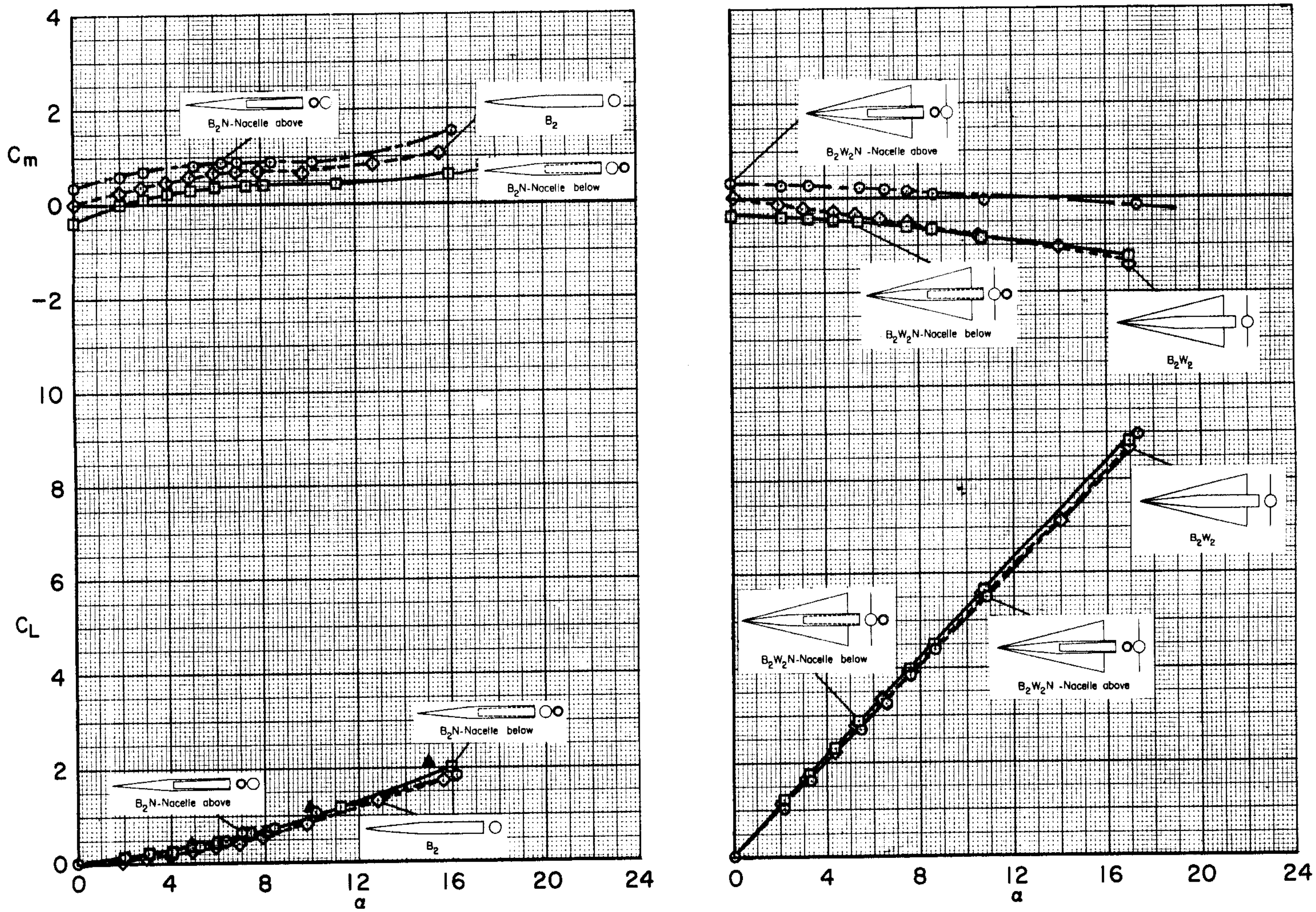

(c) B_2 and B_2N

(d) B_2W_2 and B_2W_2N

Figure 5.- Concluded.

[redacted]

[redacted]

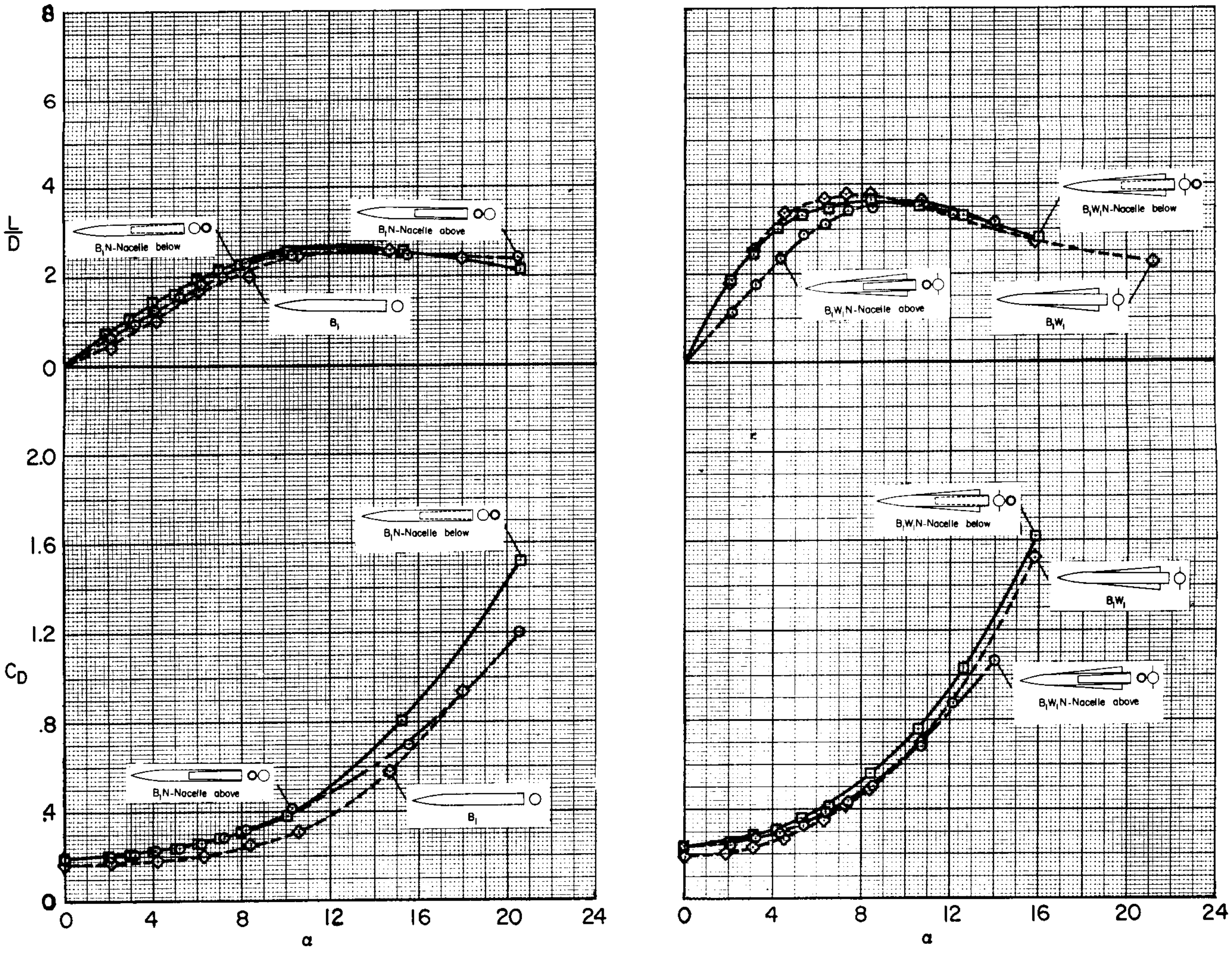

(a) B_1 and B_1N

(b) B_1W_1 and B_1W_1N

Figure 6.- Drag and lift-drag ratio at $M_\infty = 1.97$ and $\beta = 0^\circ$.

[redacted]

[redacted]

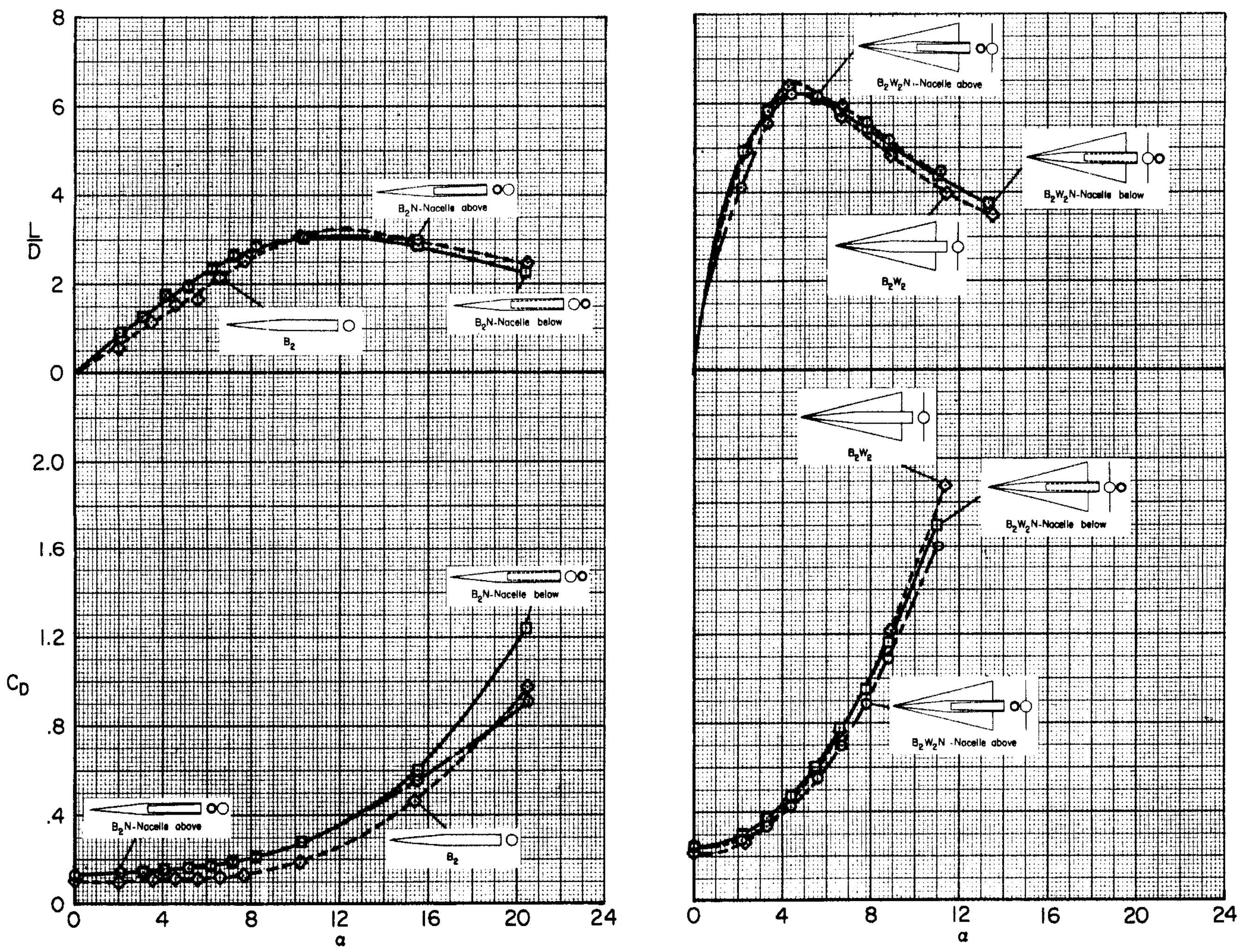

(c) B_2 and B_2N

(d) B_2W_2 and B_2W_2N

Figure 6.- Concluded.

[redacted]

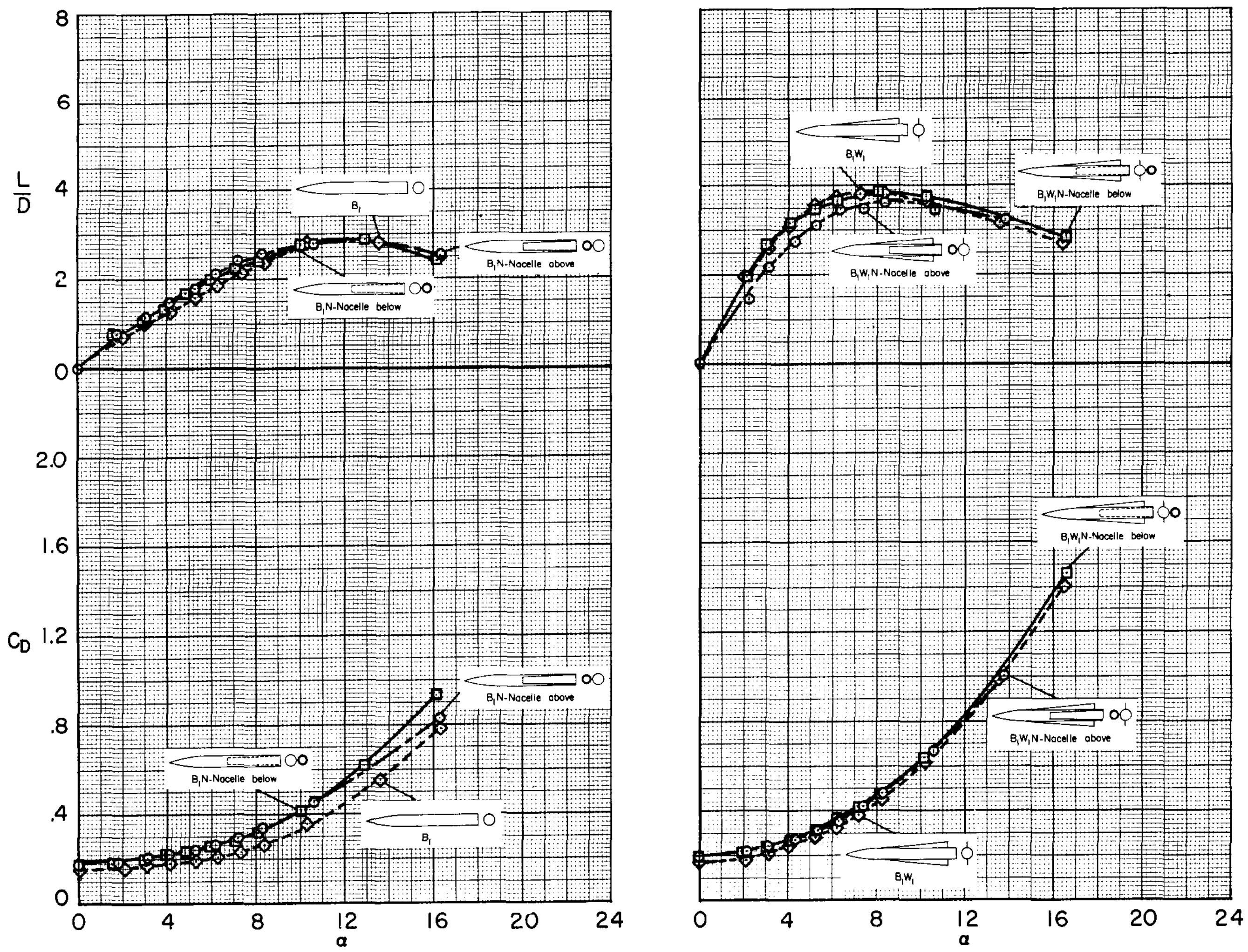

(a) B_1 and B_1N

(b) B_1W_1 and B_1W_1N

Figure 7.- Drag and lift-drag ratio at $M_\infty = 2.94$ and $\beta = 0^\circ$.

[redacted]

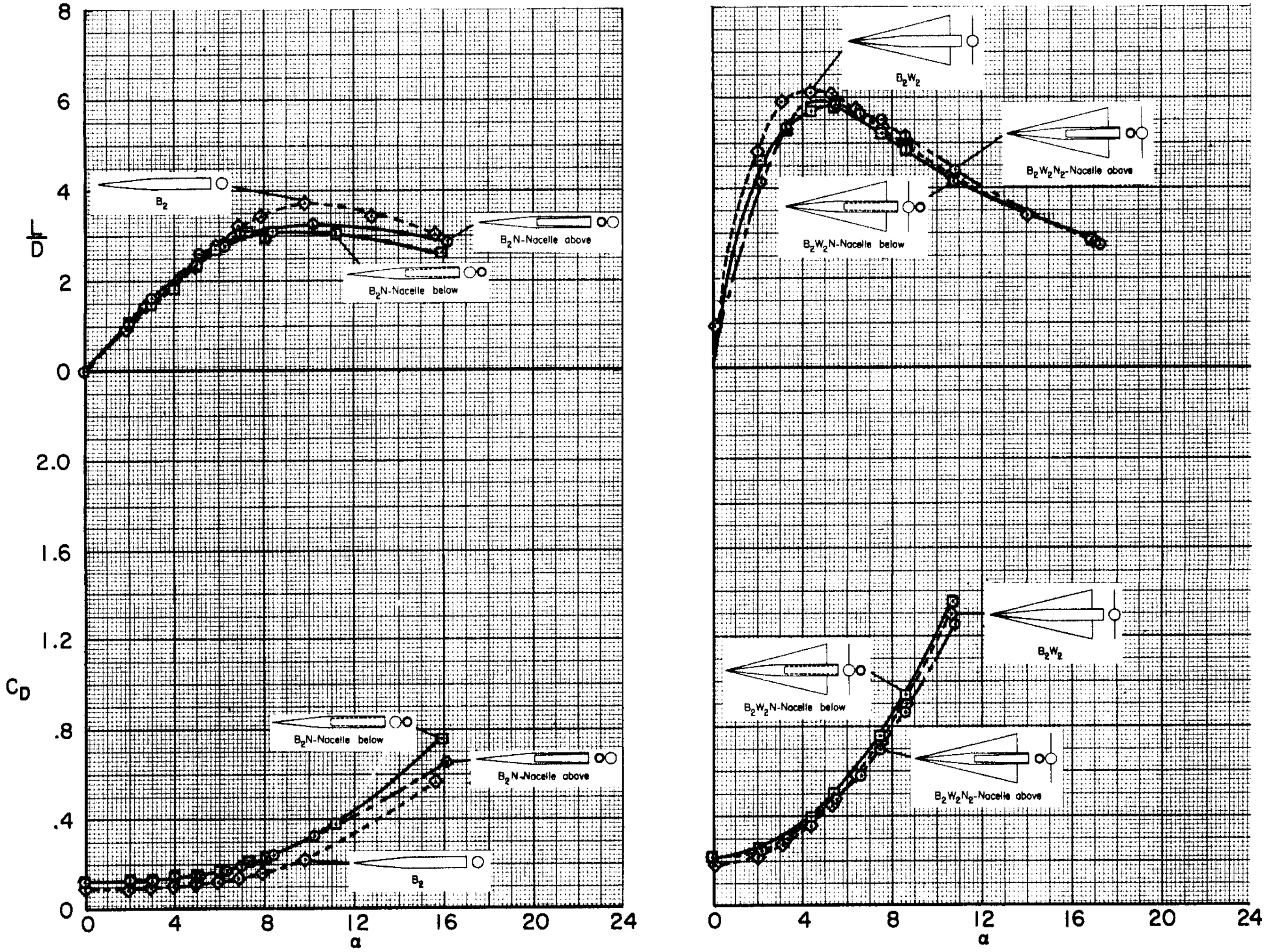

(c) B_2 and B_2N

(d) B_2W_2 and B_2W_2N

Figure 7.- Concluded.

[redacted]

[redacted]

[redacted]

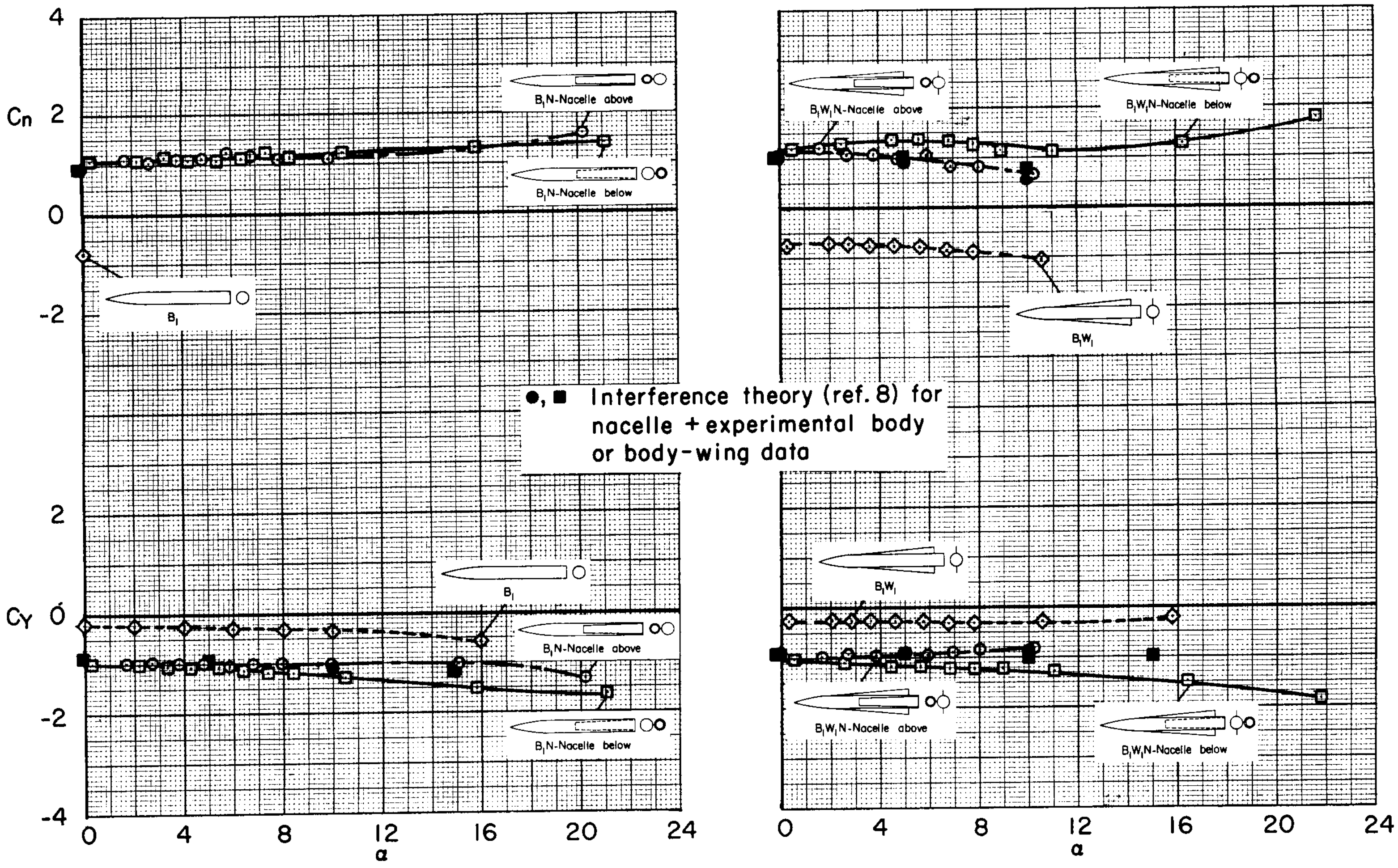

(a) B_1 and B_1N

(b) B_1W_1 and B_1W_1N

Figure 8.- Side force and yawing moment for $\beta = 5^{\circ}$ and $M_{\infty} = 1.97$.

[redacted]

[redacted]

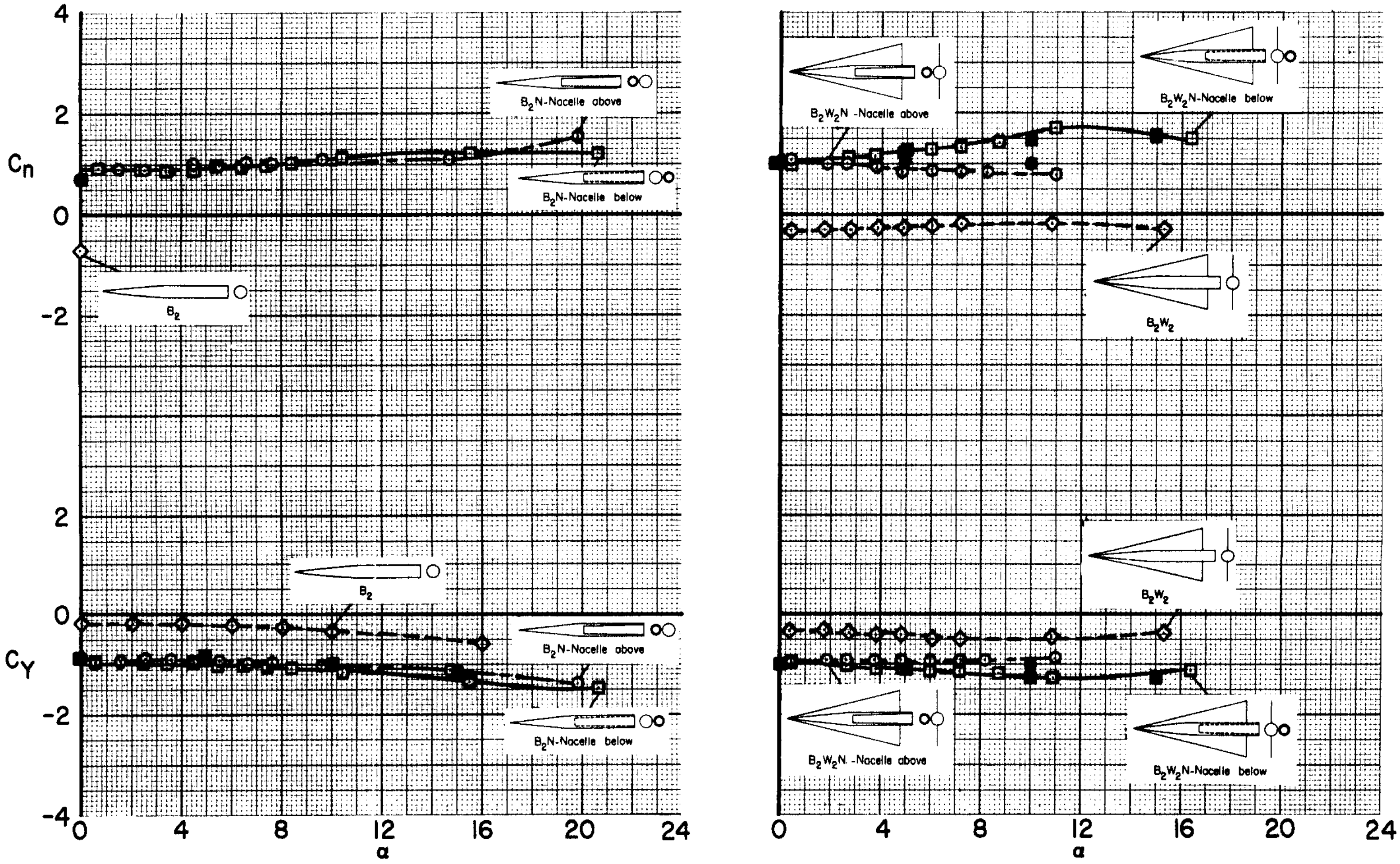

(c) B_2 and B_2N

(d) B_2W_2 and B_2W_2N

Figure 8.- Concluded.

[redacted]

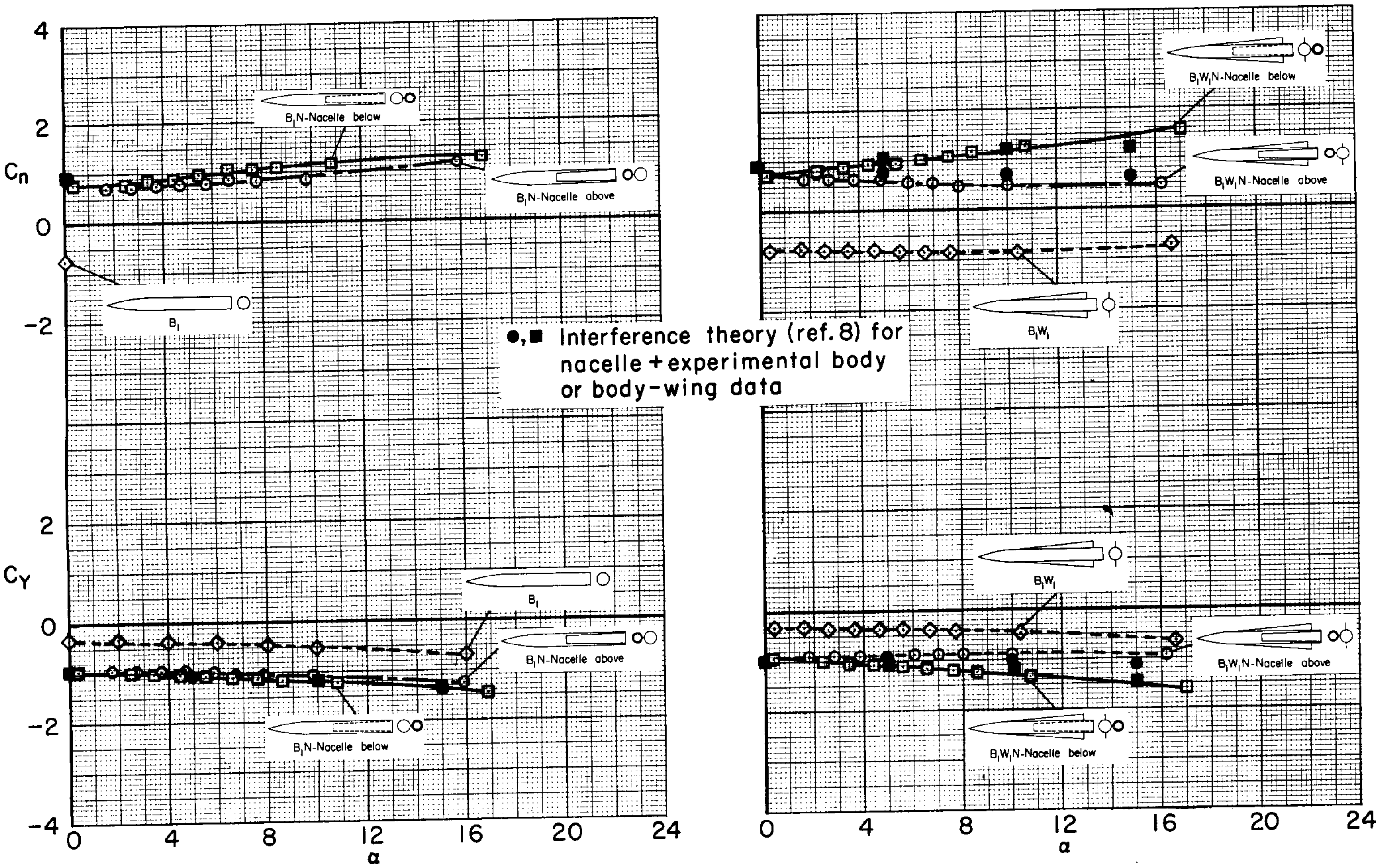

(a) B_1 and B_1N

(b) B_1W_1 and B_1W_1N

Figure 9.- Side force and yawing moment for $\beta = 5^{\circ}$ and $M_{\infty} = 2.94$.

[redacted]

[redacted]

[redacted]

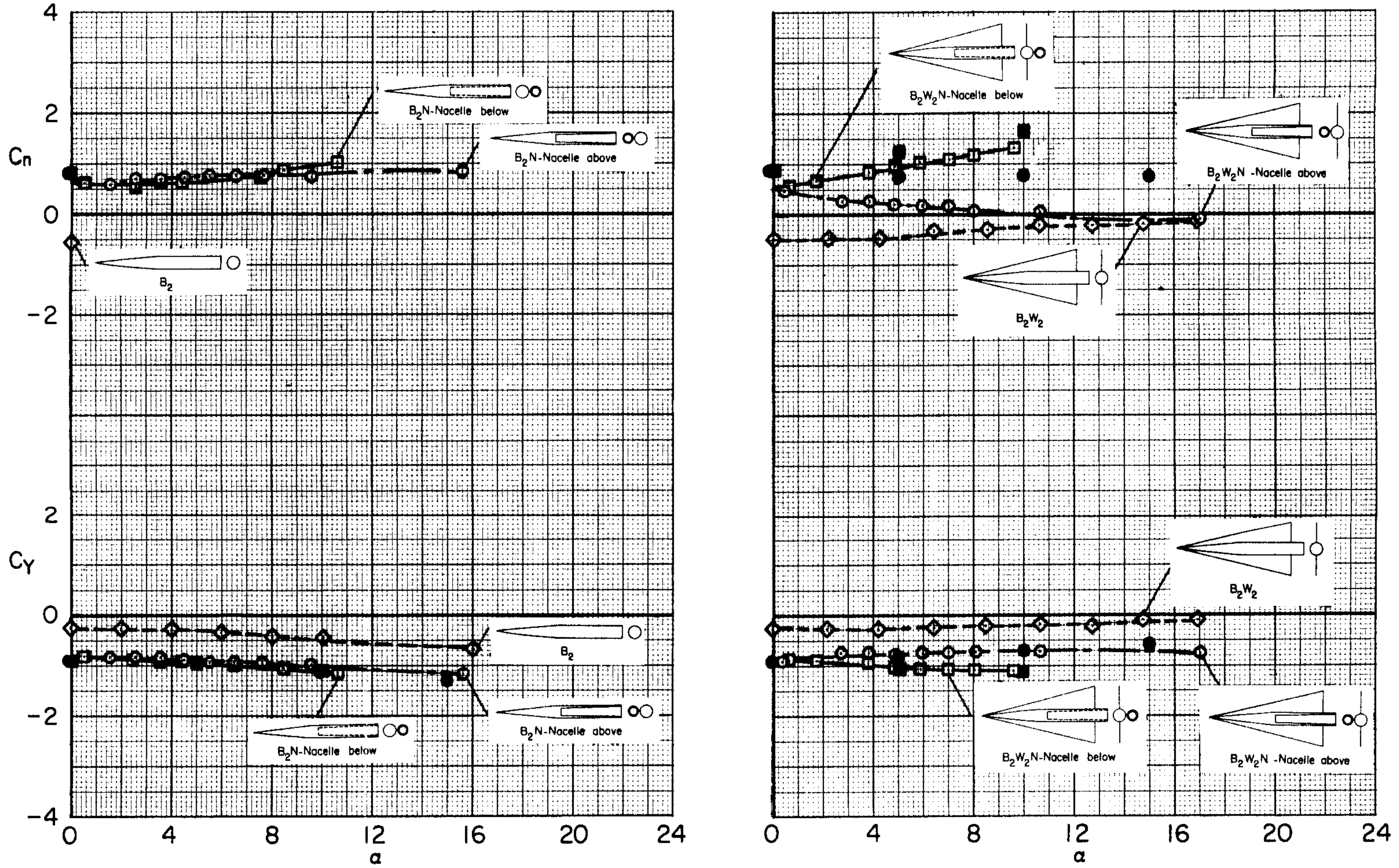

(c) B_2 and B_2N

(d) B_2W_2 and B_2W_2N

Figure 9.- Concluded.

UNCLASSIFIED [redacted]

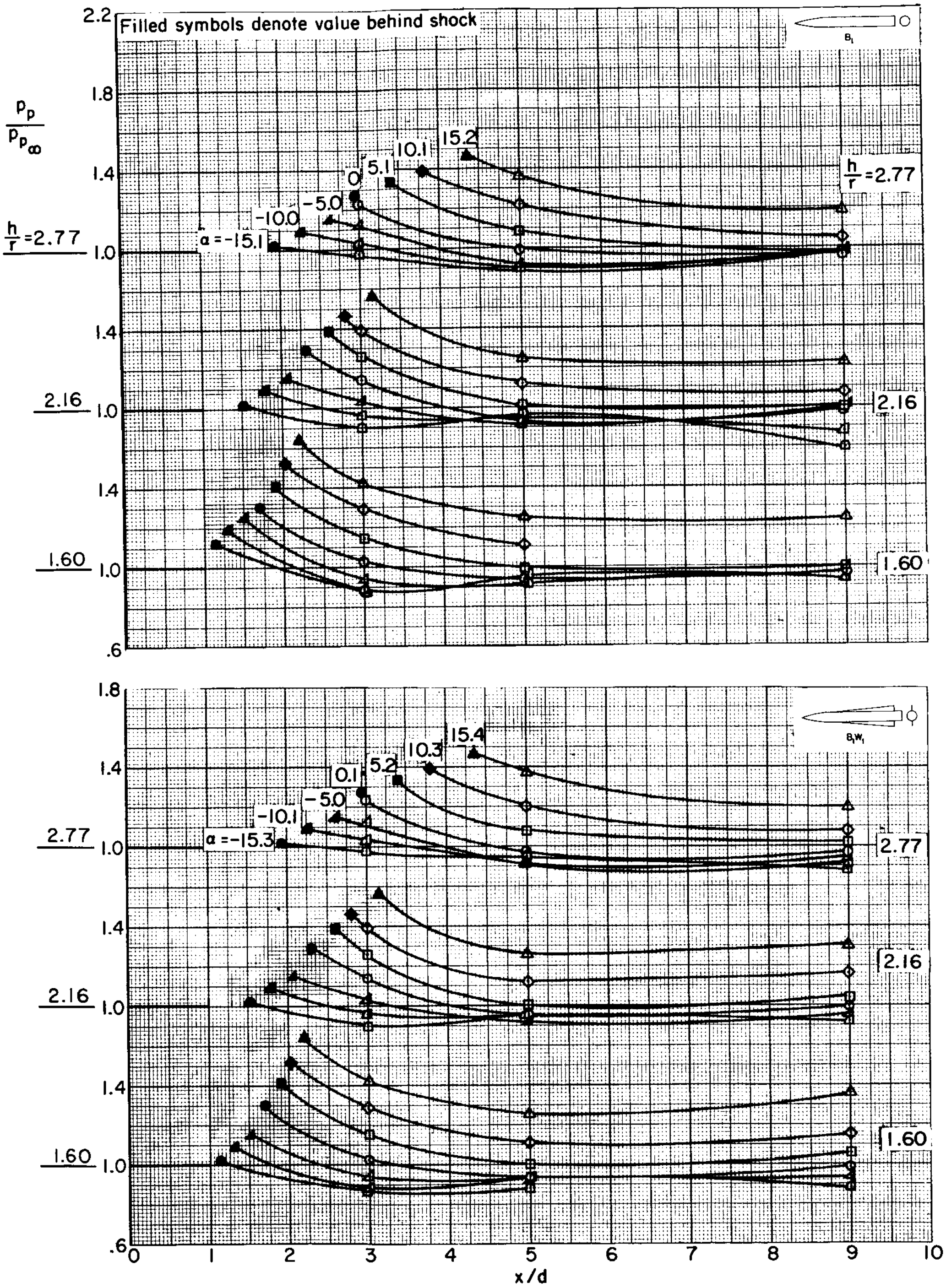

(a) B_1 and B_1W_1

Figure 10.- Pitot-pressure ratio in vertical plane of symmetry for $\beta = 0^o$ and $M_\infty = 2.95$.

[redacted]

DECLASSIFIED

[redacted]

A-176

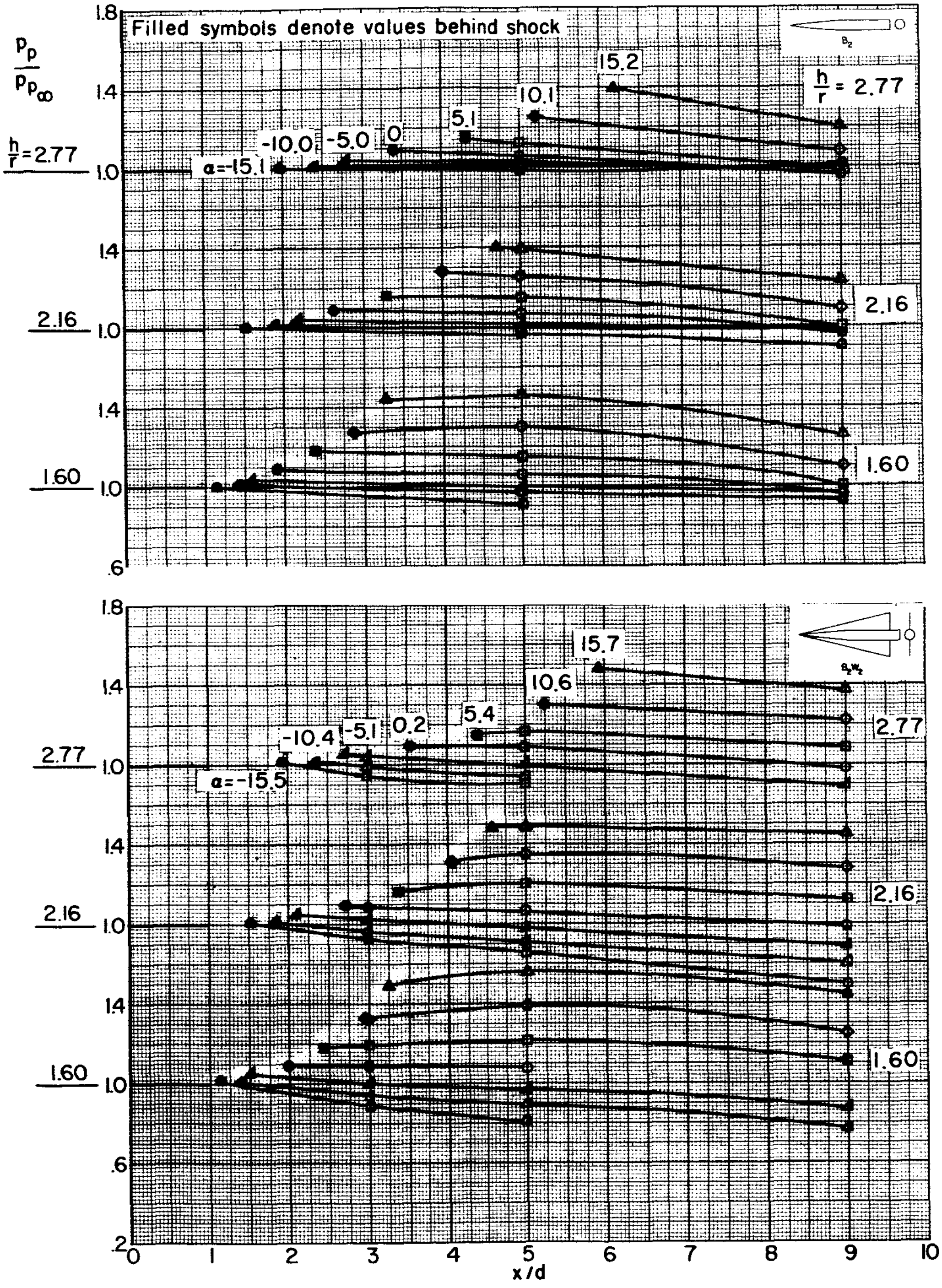

(b) B_2 and B_2W_2

Figure 10.- Concluded.

[redacted]

[redacted]

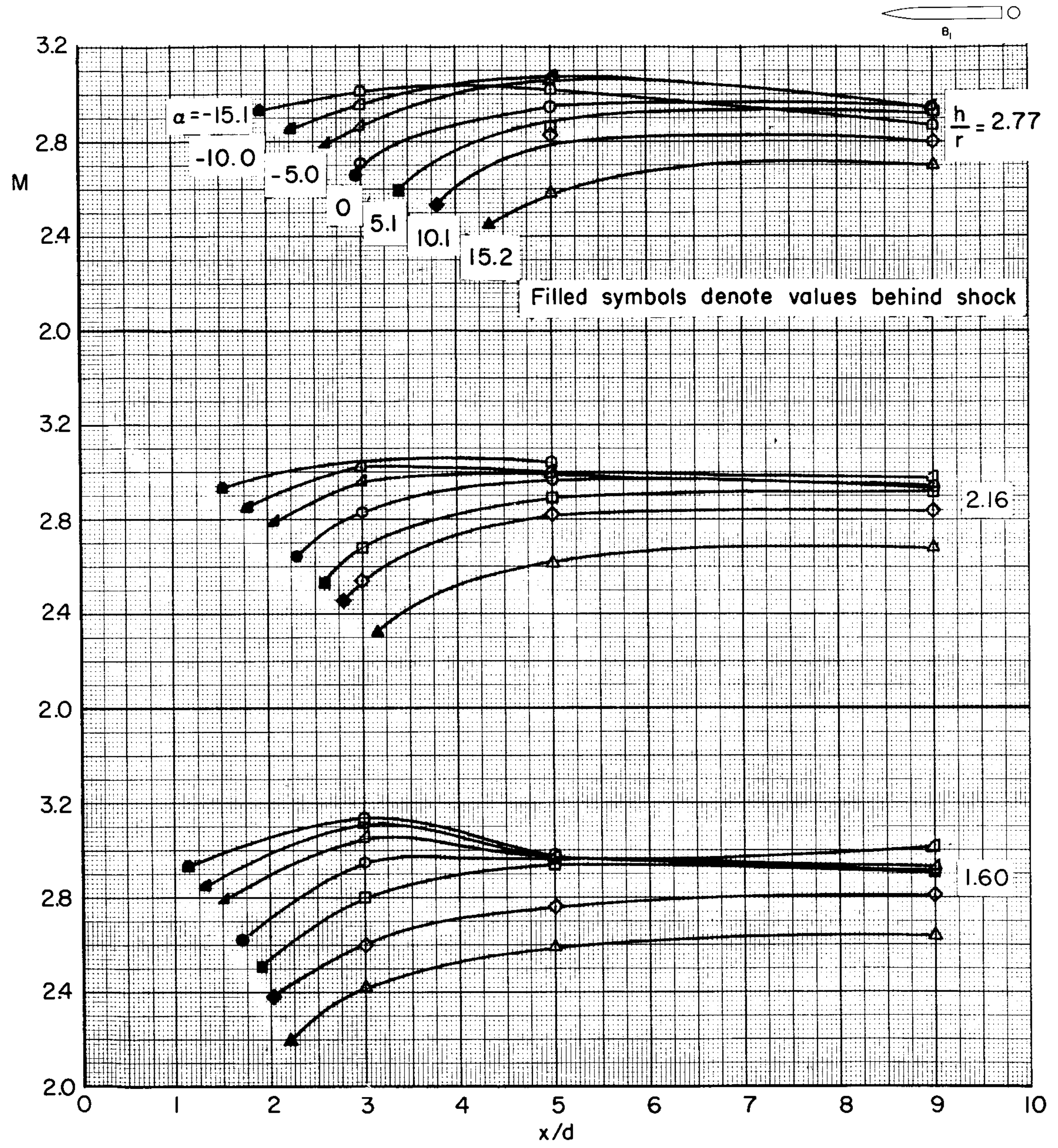

(a) B_1

Figure 11.- Mach number in vertical plane of symmetry for $\beta = 0^\circ$ and $M_\infty = 2.95$.

[redacted]

[redacted]

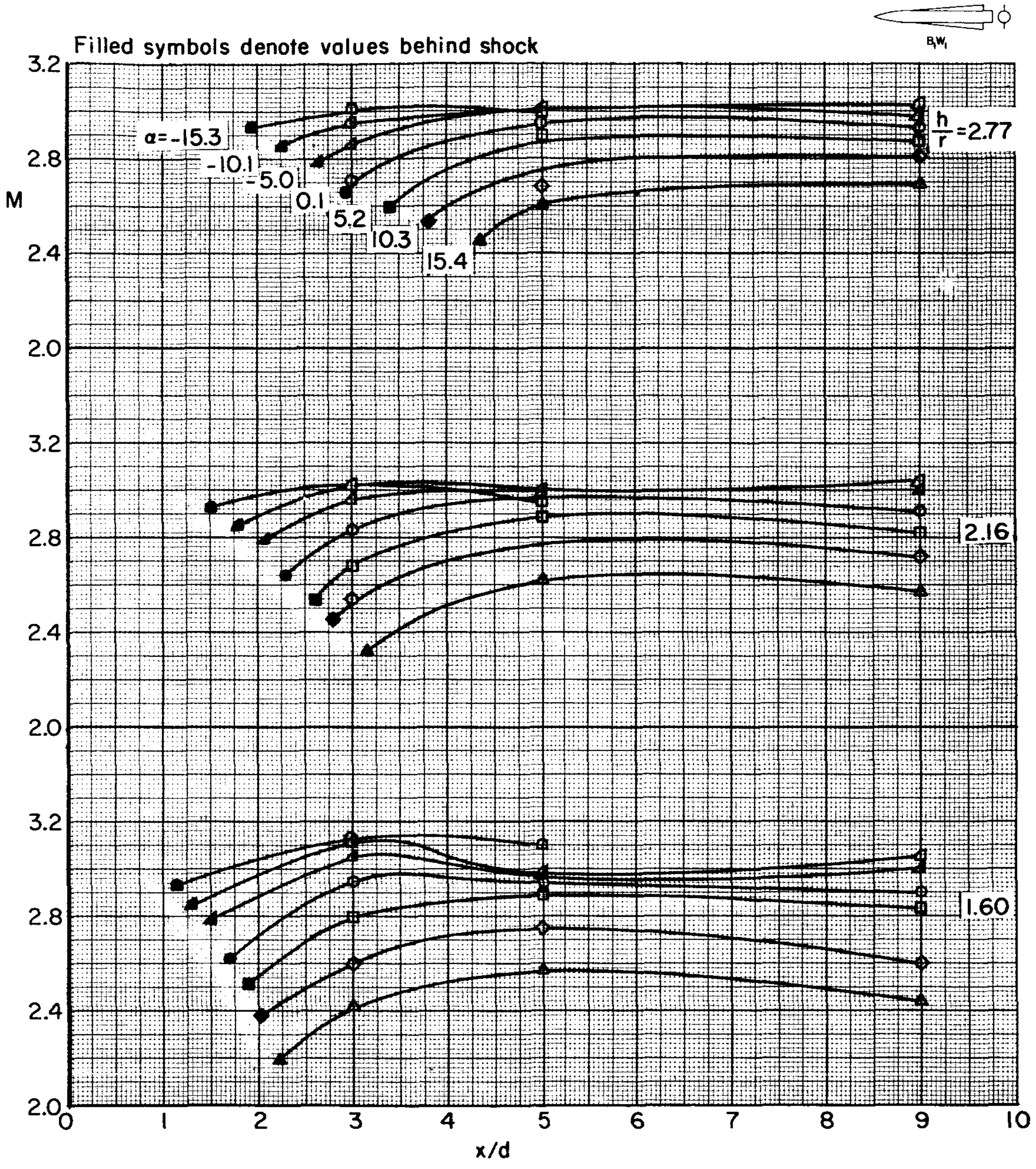

(b) B_1W_1

Figure 11.- Continued.

[redacted]

[redacted]

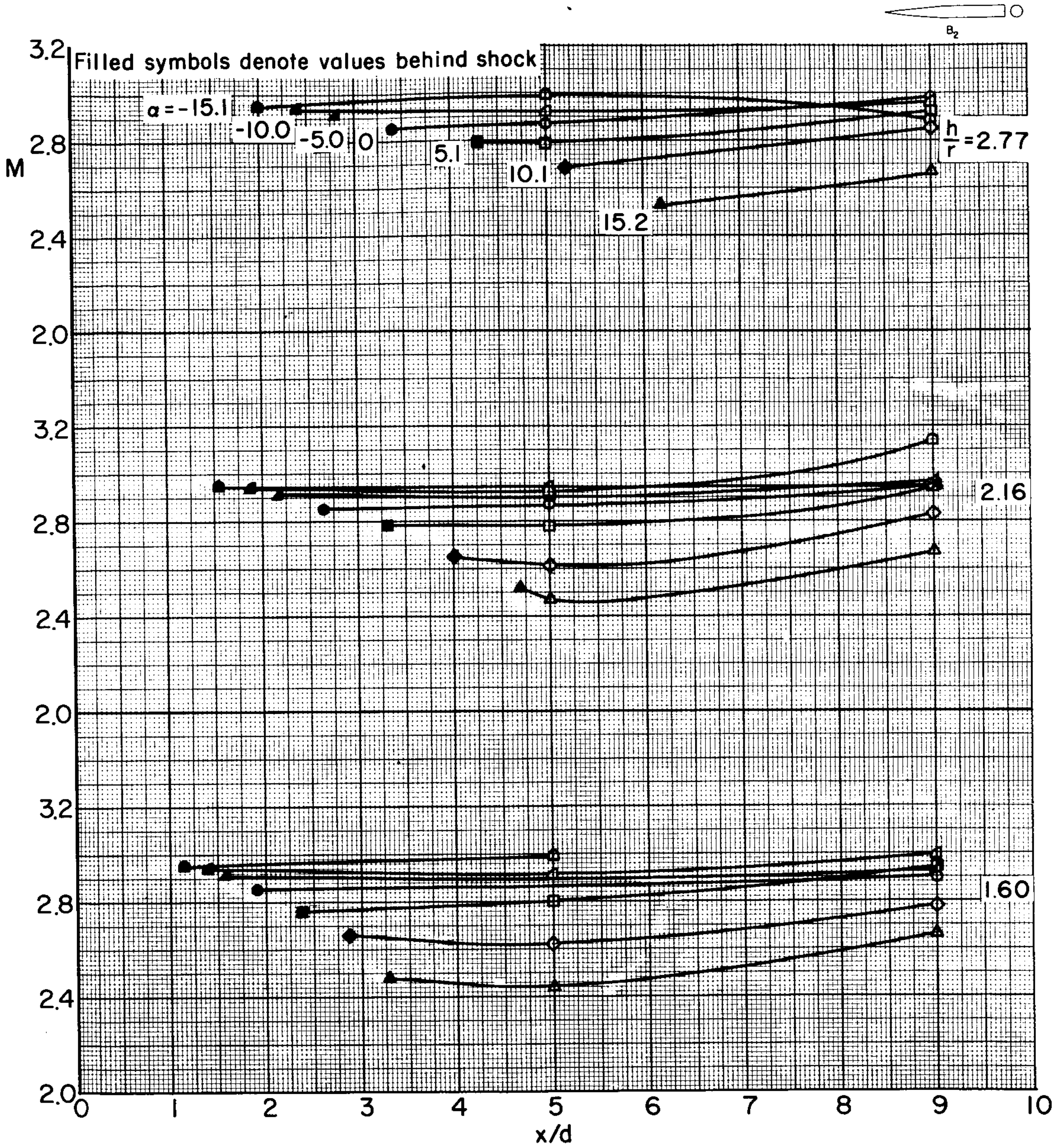

(c) B_2

Figure 11.- Continued.

[redacted]

[redacted]

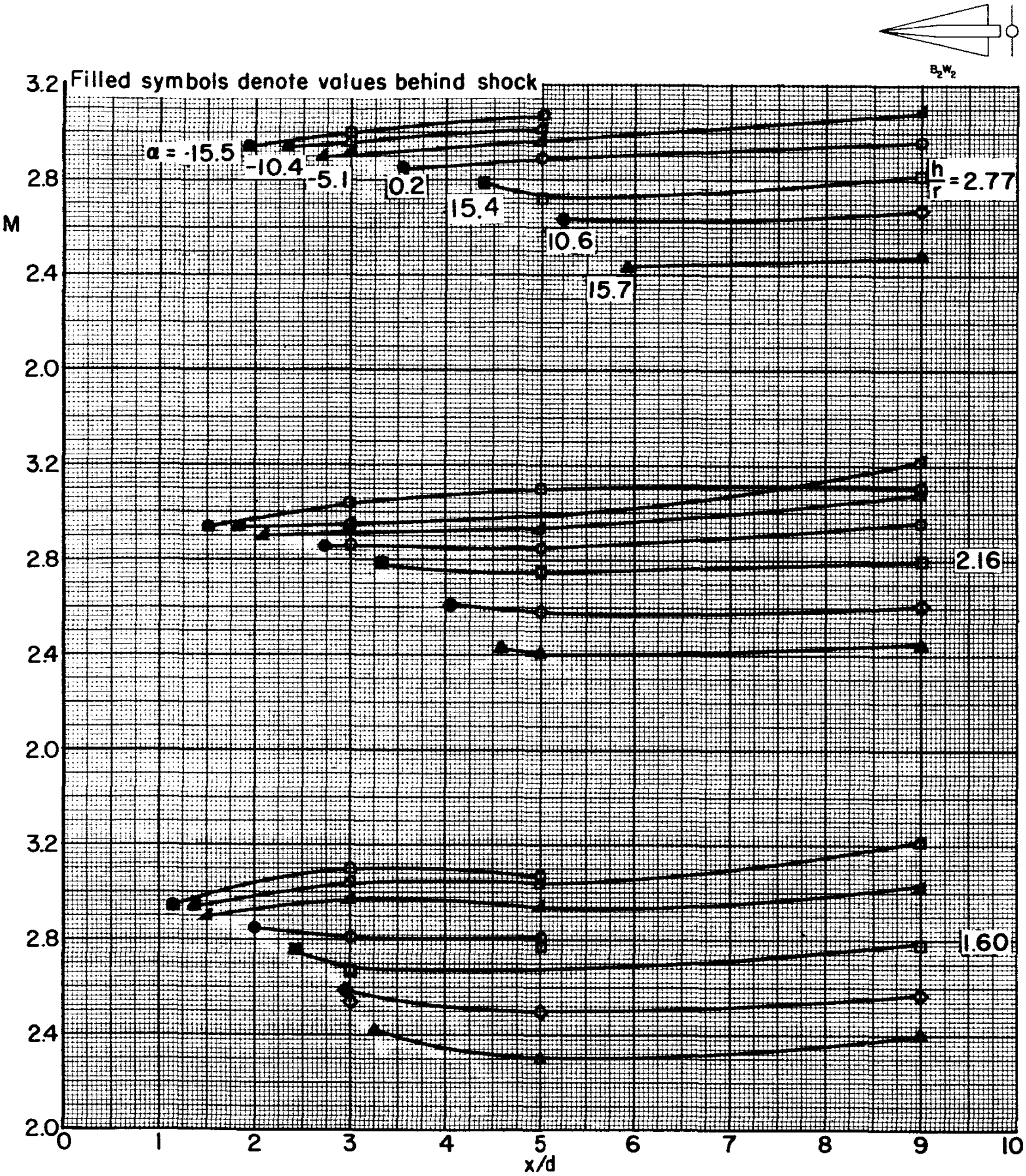

(d) B_2W_2

Figure 11.- Concluded.

[redacted]

[redacted]

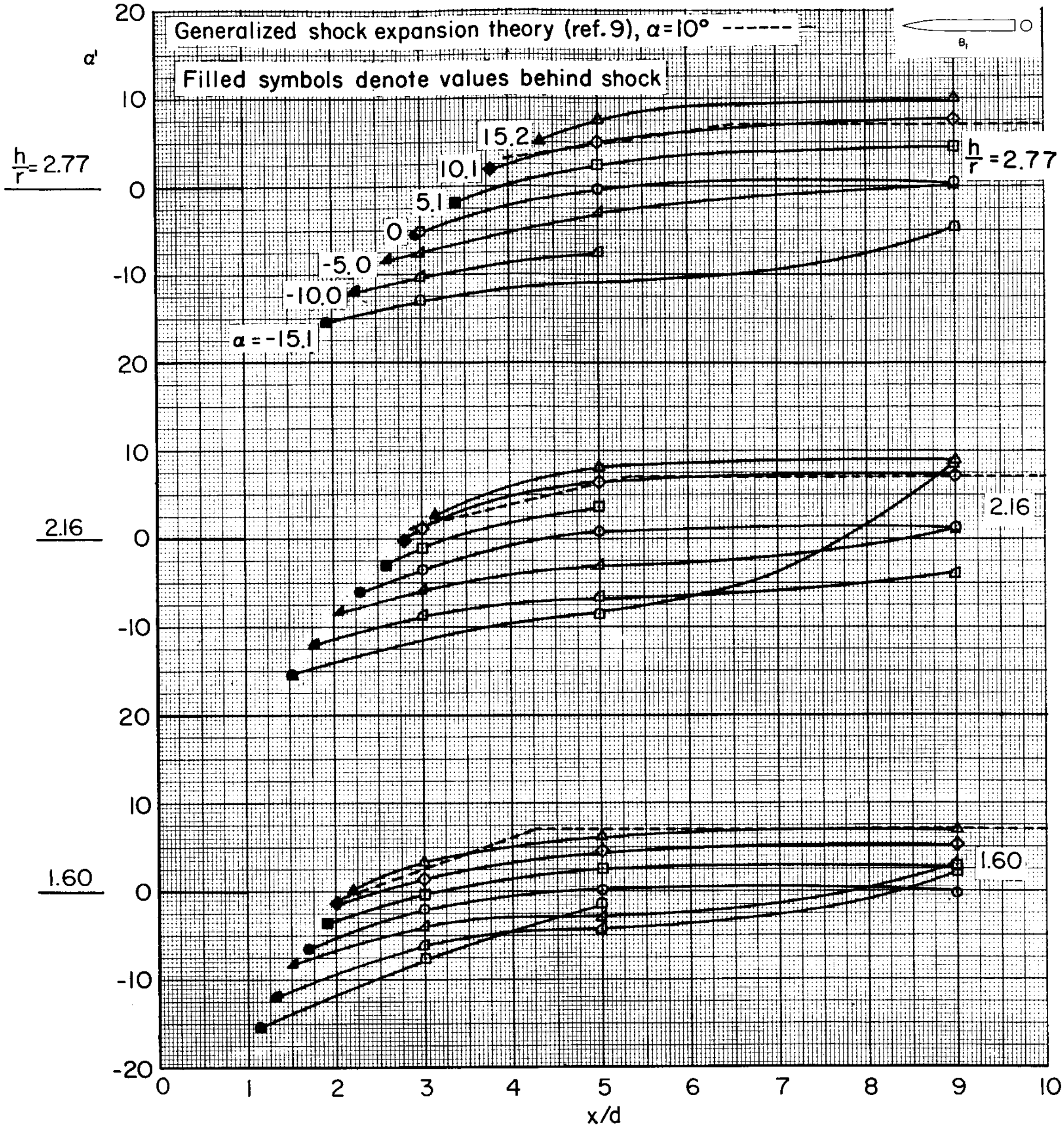

(a) B_1

Figure 12.- Local angle of attack in vertical plane of symmetry for $\beta = 0^{\circ}$ and $M_\infty = 2.95$.

[redacted]

[redacted]

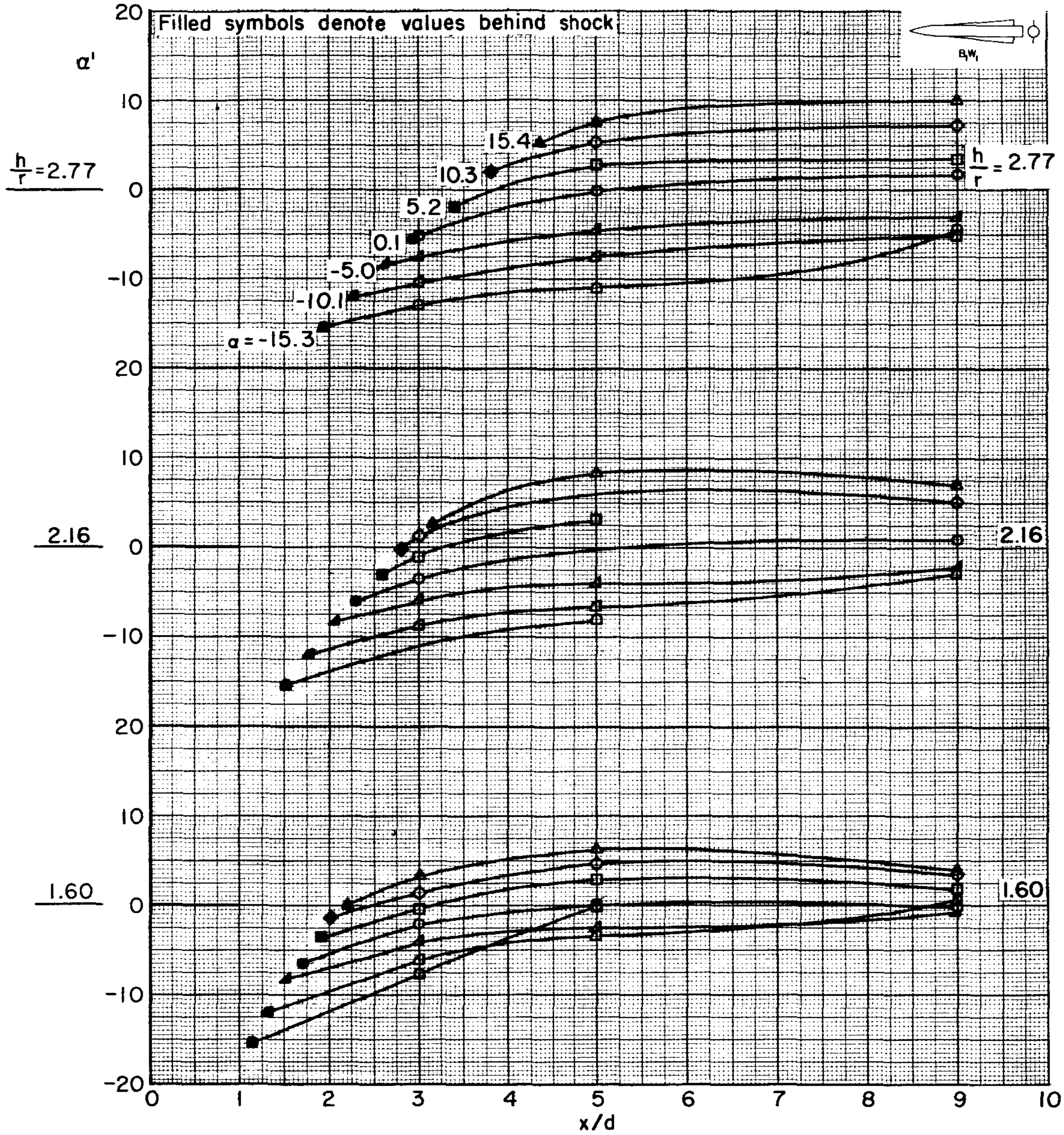

(b) B_1W_1

Figure 12.- Continued.

[redacted]

[redacted]

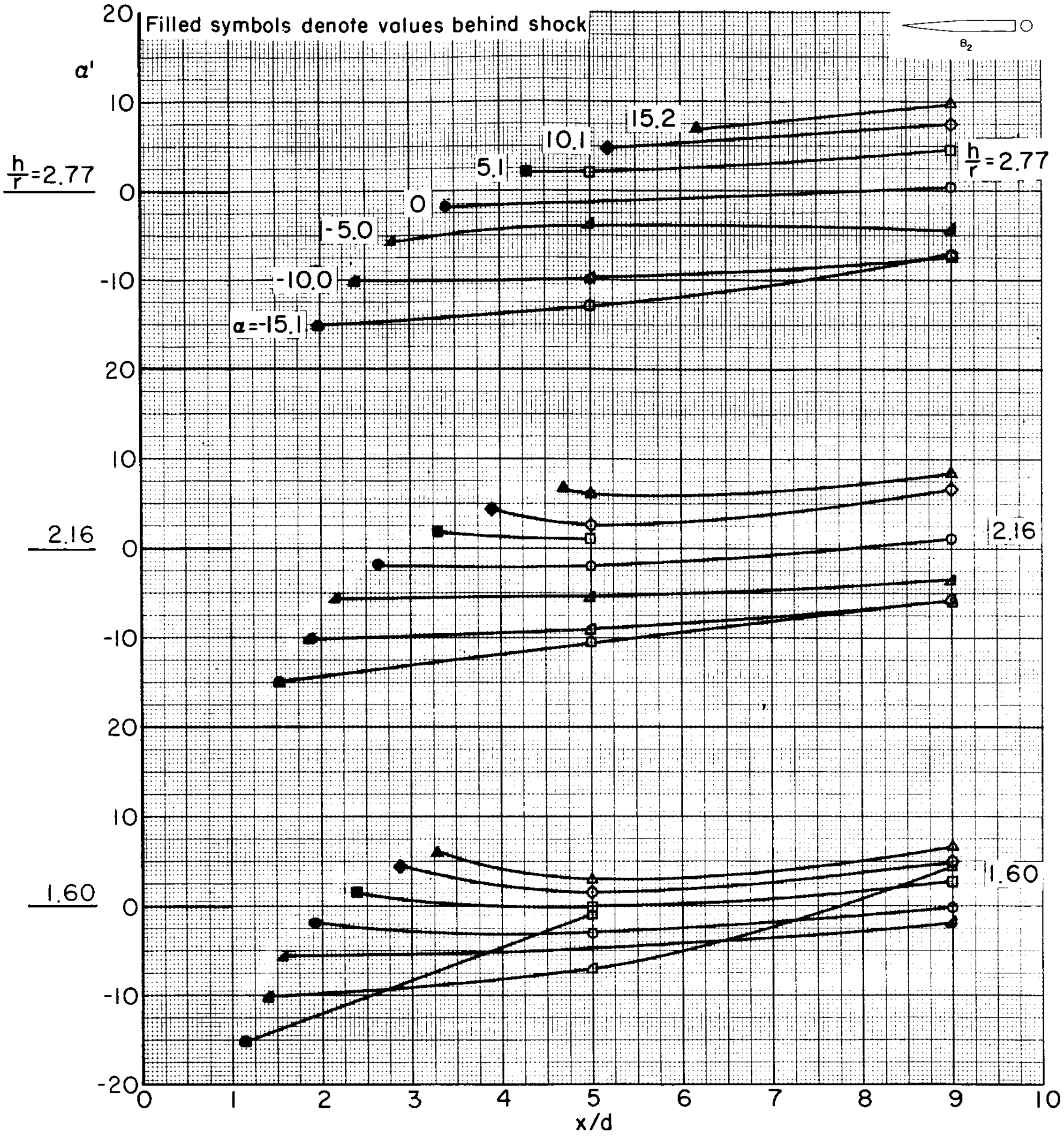

(c) B_2

Figure 12.- Continued.

[redacted]

[redacted]

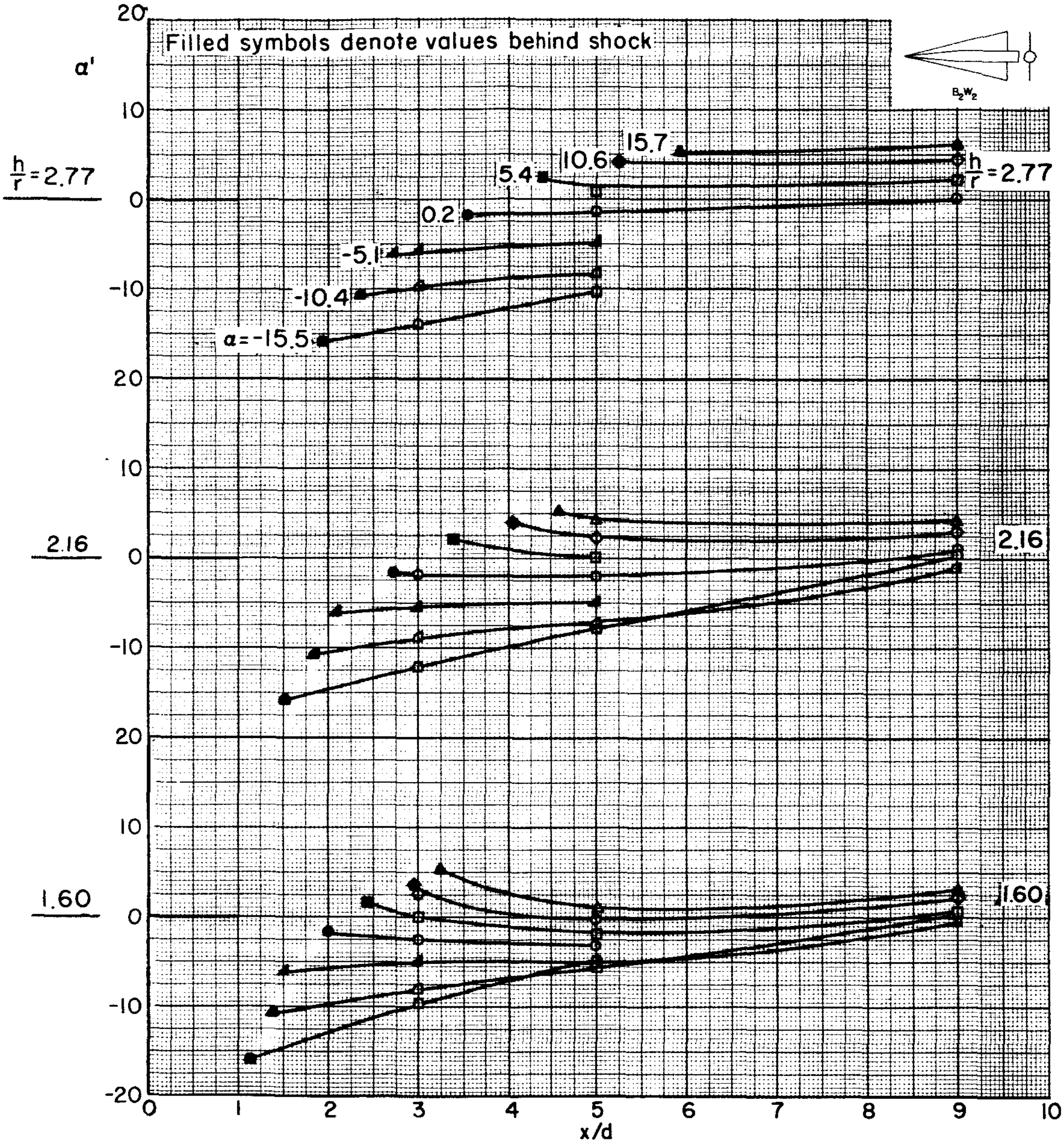

(d) B_2W_2

Figure 12.- Concluded.

A-176

[redacted]

[redacted]

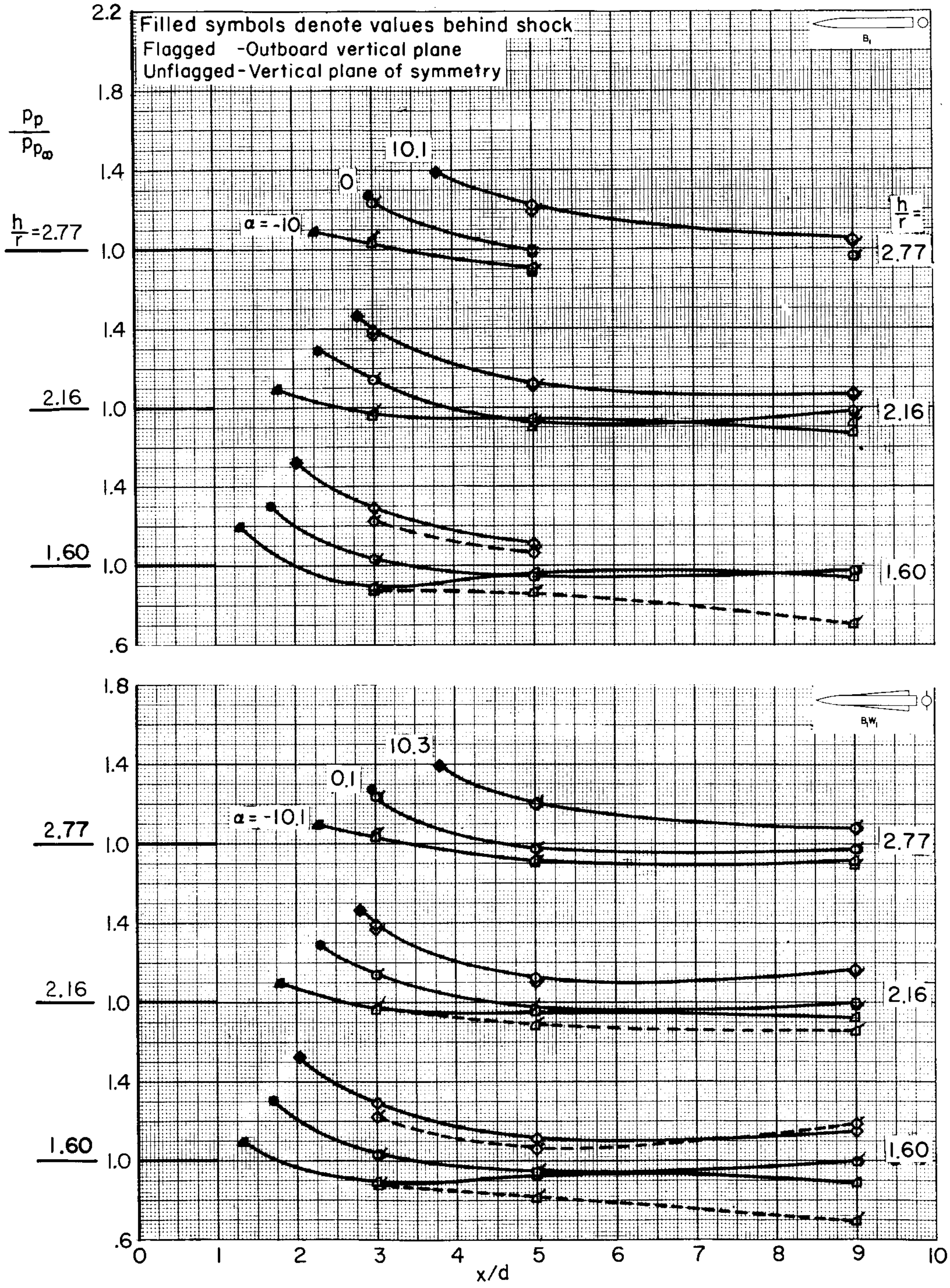

(a) B_1 and B_1W_1

Figure 13.- Comparison of pitot-pressure ratio in outboard plane and plane of symmetry for $\beta = 0^\circ$ and $M_\infty = 2.95$.

[redacted]

DECLASSIFIED

[redacted]

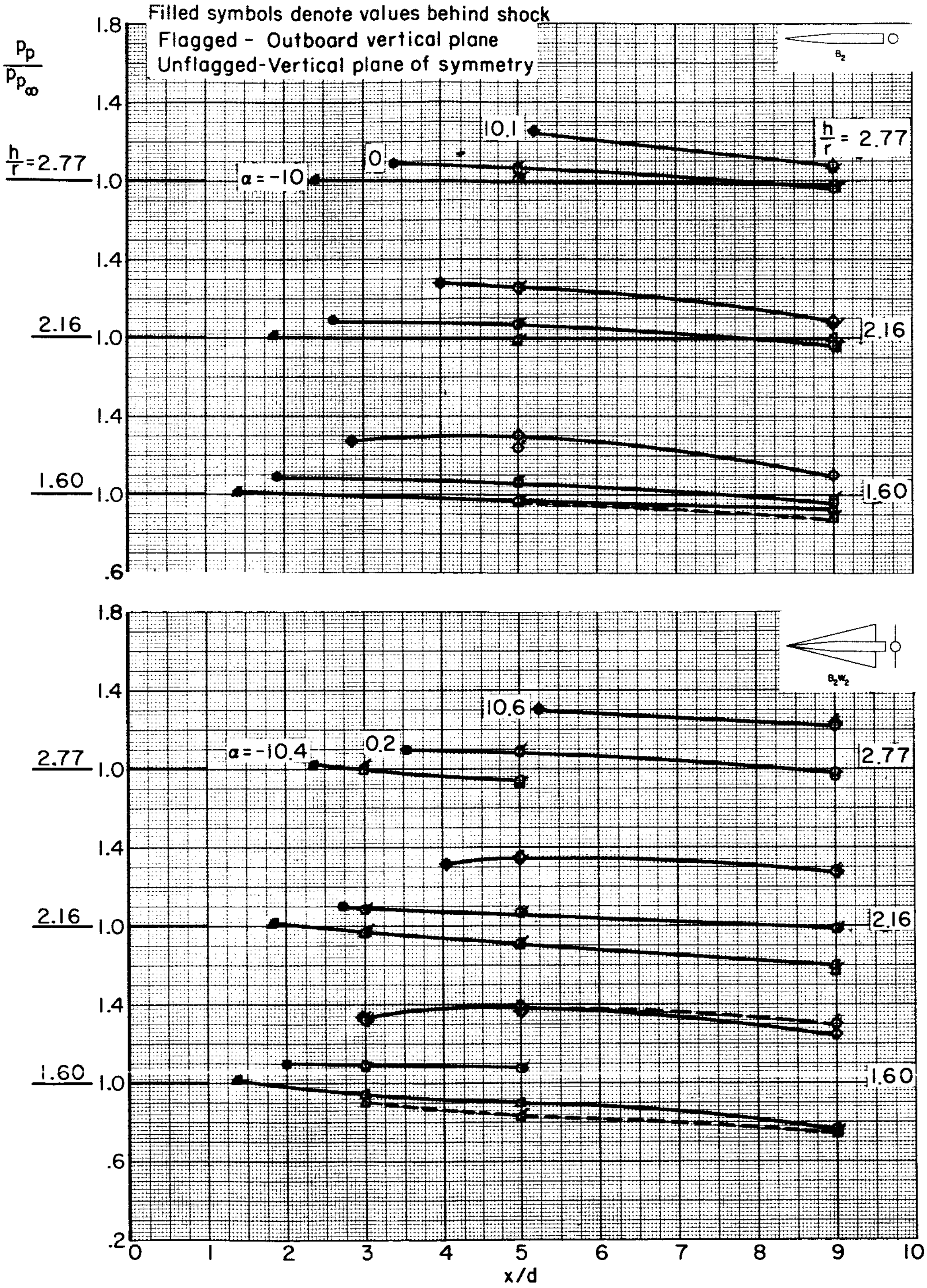

(b) B_2 and B_2W_2

Figure 13.- Concluded.

[redacted]

[redacted]

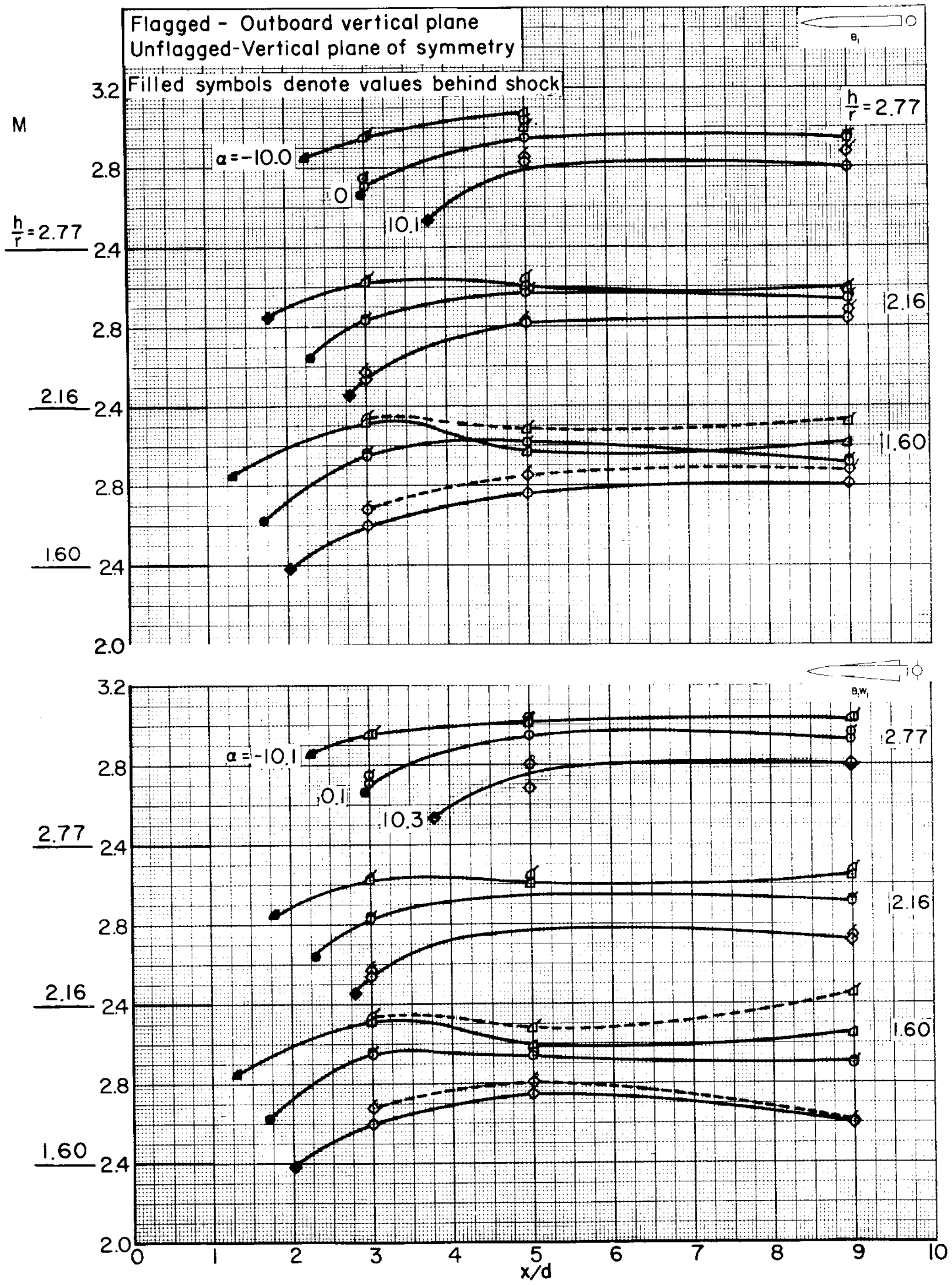

(a) B_1 and B_1W_1

Figure 14.- Comparison of Mach number in outboard plane and plane of symmetry for $\beta = 0^\circ$ and $M_\infty = 2.95$.

[redacted]

[redacted]

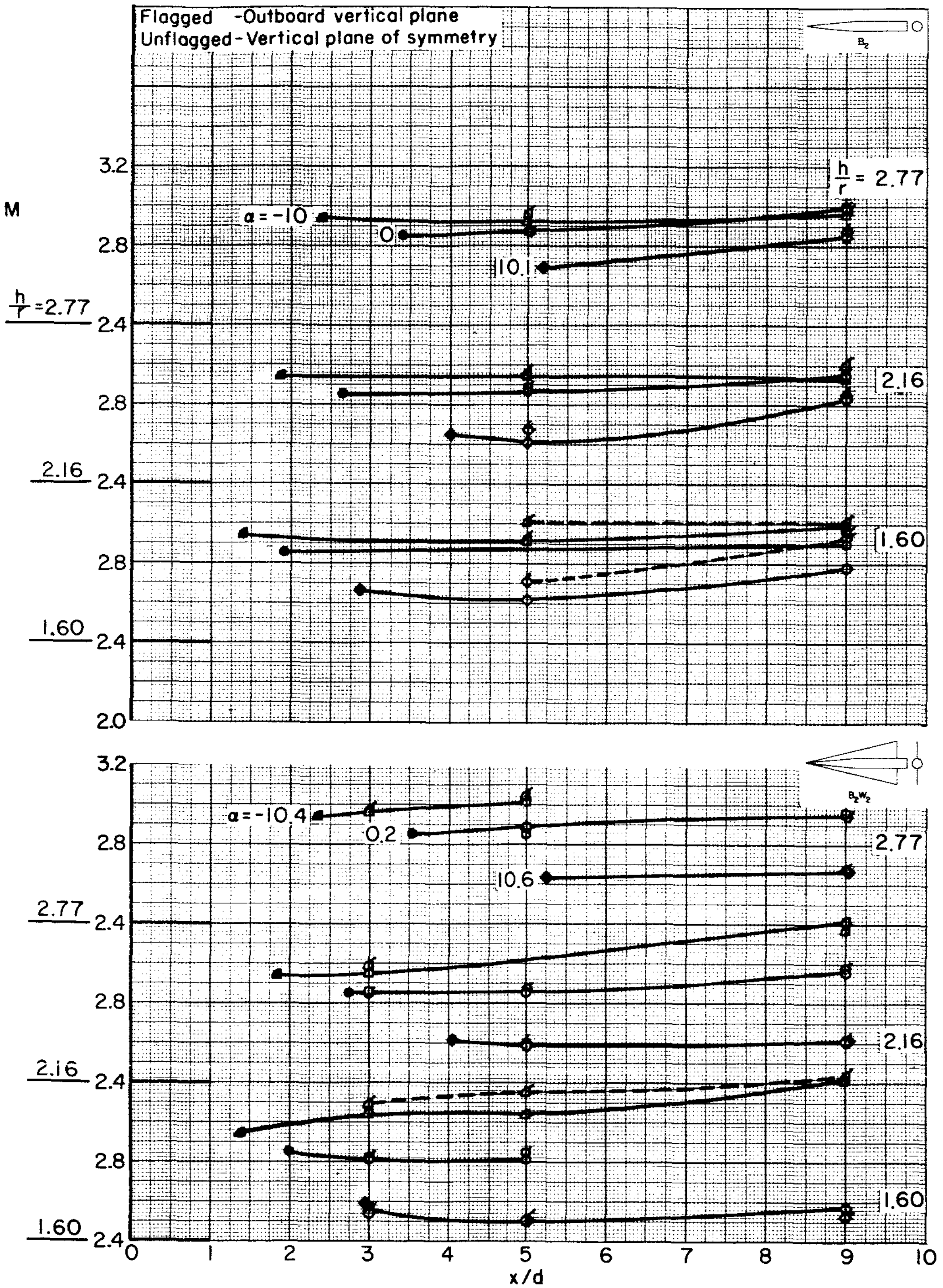

(b) B_2 and B_2W_2

Figure 14.- Concluded.

[redacted]

[redacted]

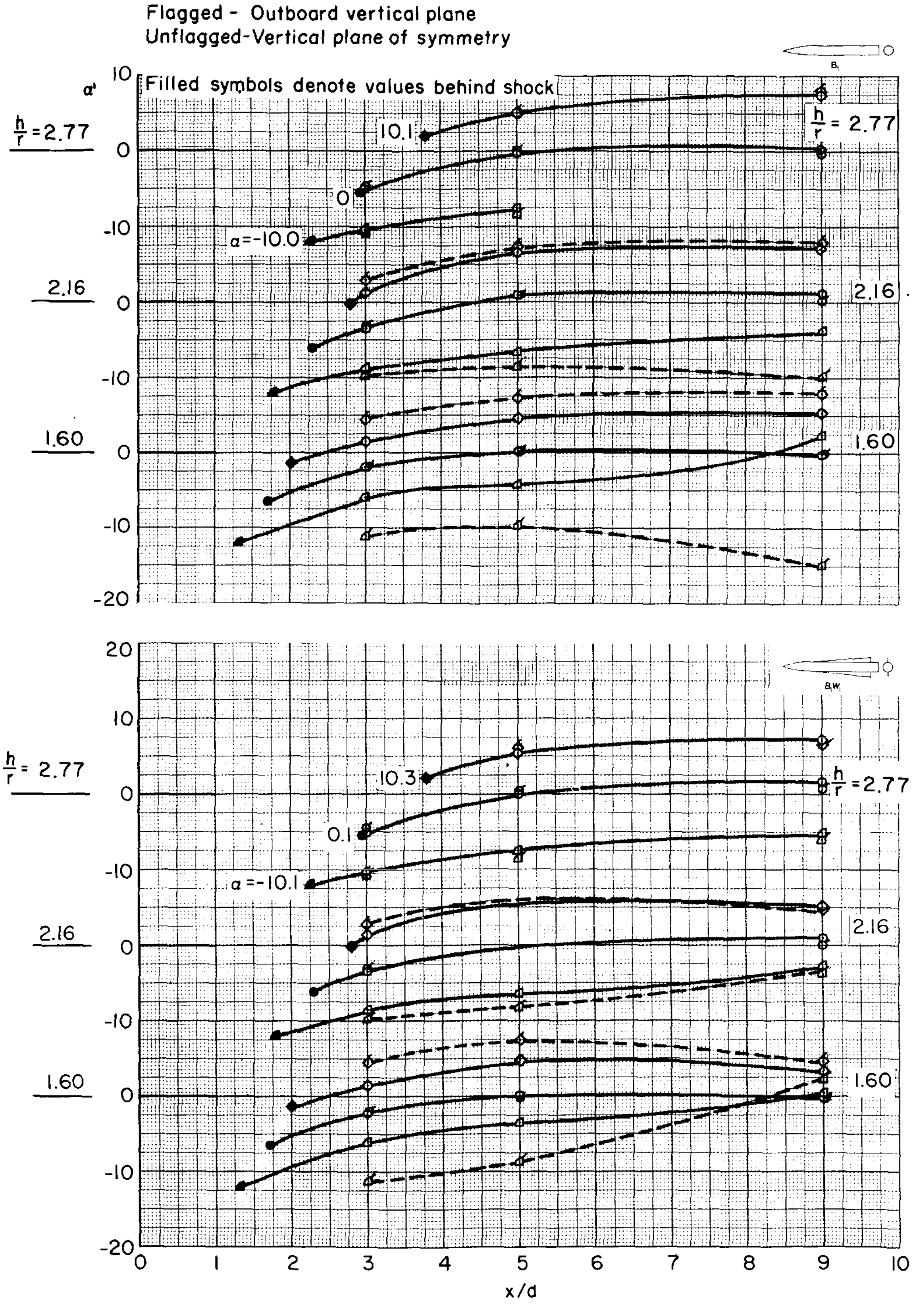

(a) B_1 and B_1W_1

Figure 15.- Comparison of local angle of attack in outboard plane and plane of symmetry for $\beta = 0^{\circ}$ and $M_{\infty} = 2.95$.

[redacted]

DECLASSIFIED

[redacted]

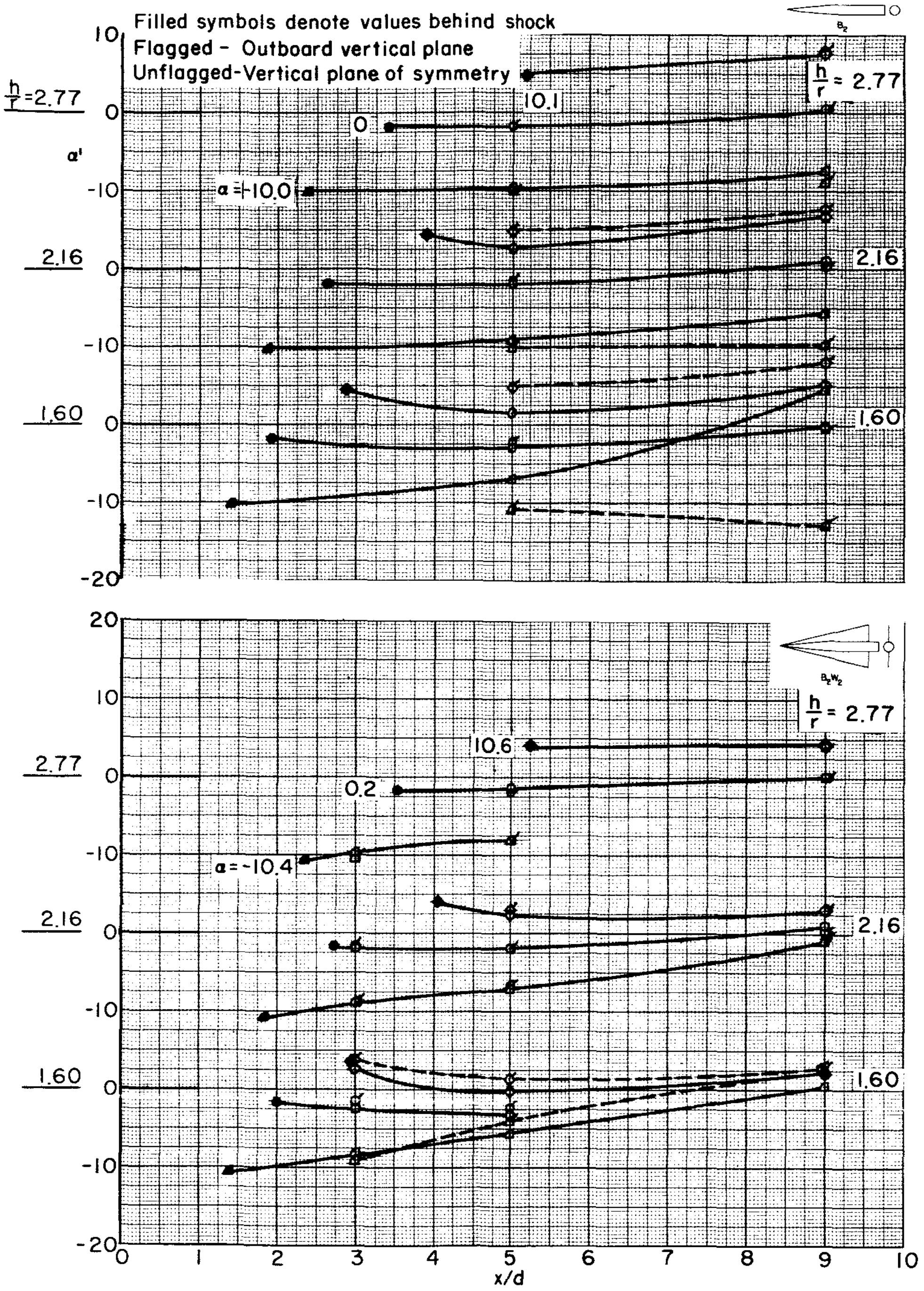

(b) B_2 and B_2W_2

Figure 15.- Concluded.

[redacted]

[redacted]

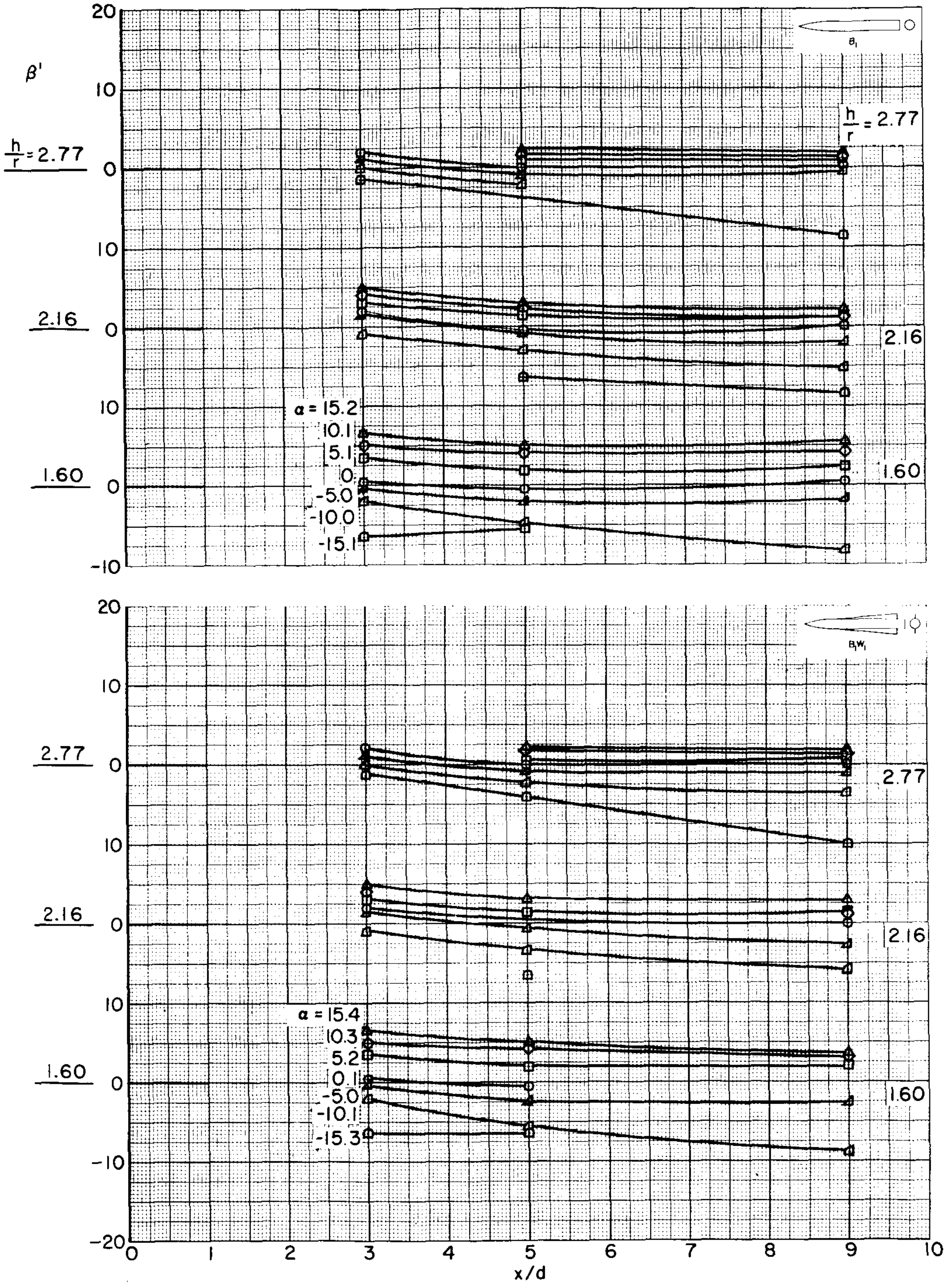

(a) B_1 and B_1W_1

Figure 16.- Local sideslip angle in left outboard vertical plane for $\beta = 0^{\circ}$ and $M_\infty = 2.95$.

[redacted]

[redacted]

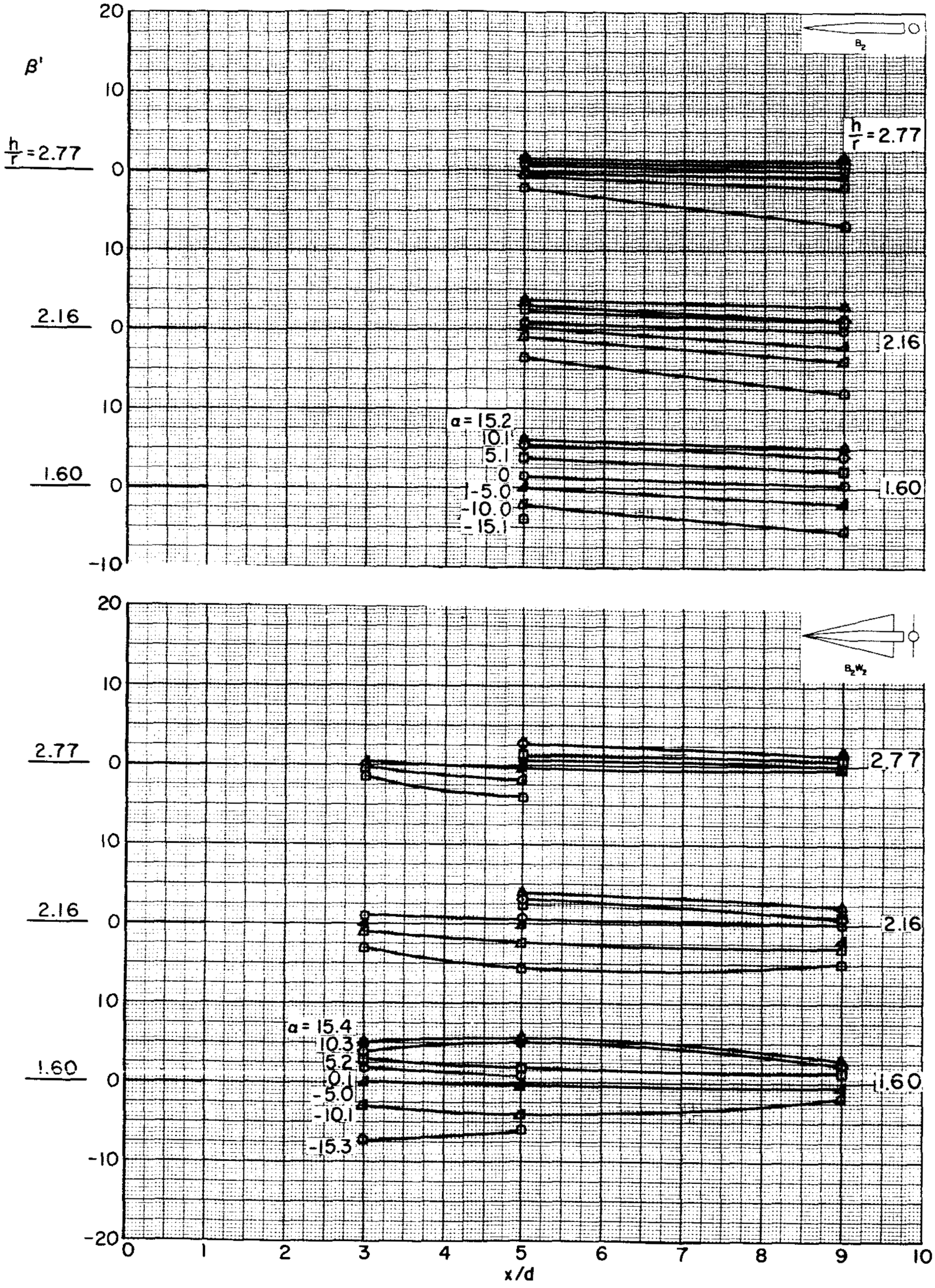

(b) B_2 and B_2W_2

Figure 16.- Concluded.

[redacted]

[redacted]

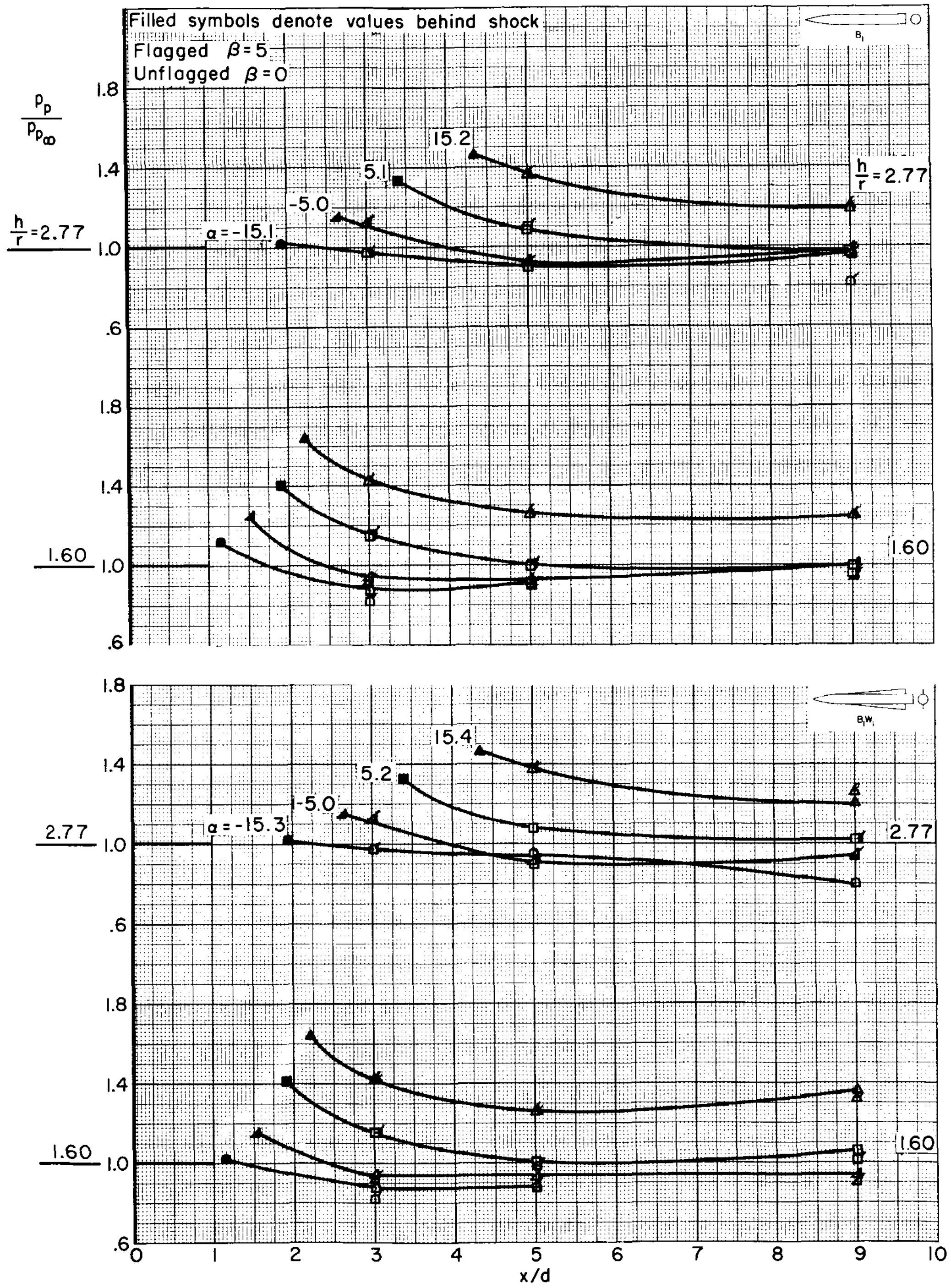

(a) B_1 and B_1W_1

Figure 17.- Comparison of pitot-pressure ratio in vertical plane of symmetry for $\beta = 0^\circ$ and 5°, and $M_\infty = 2.95$.

[redacted]

[redacted]

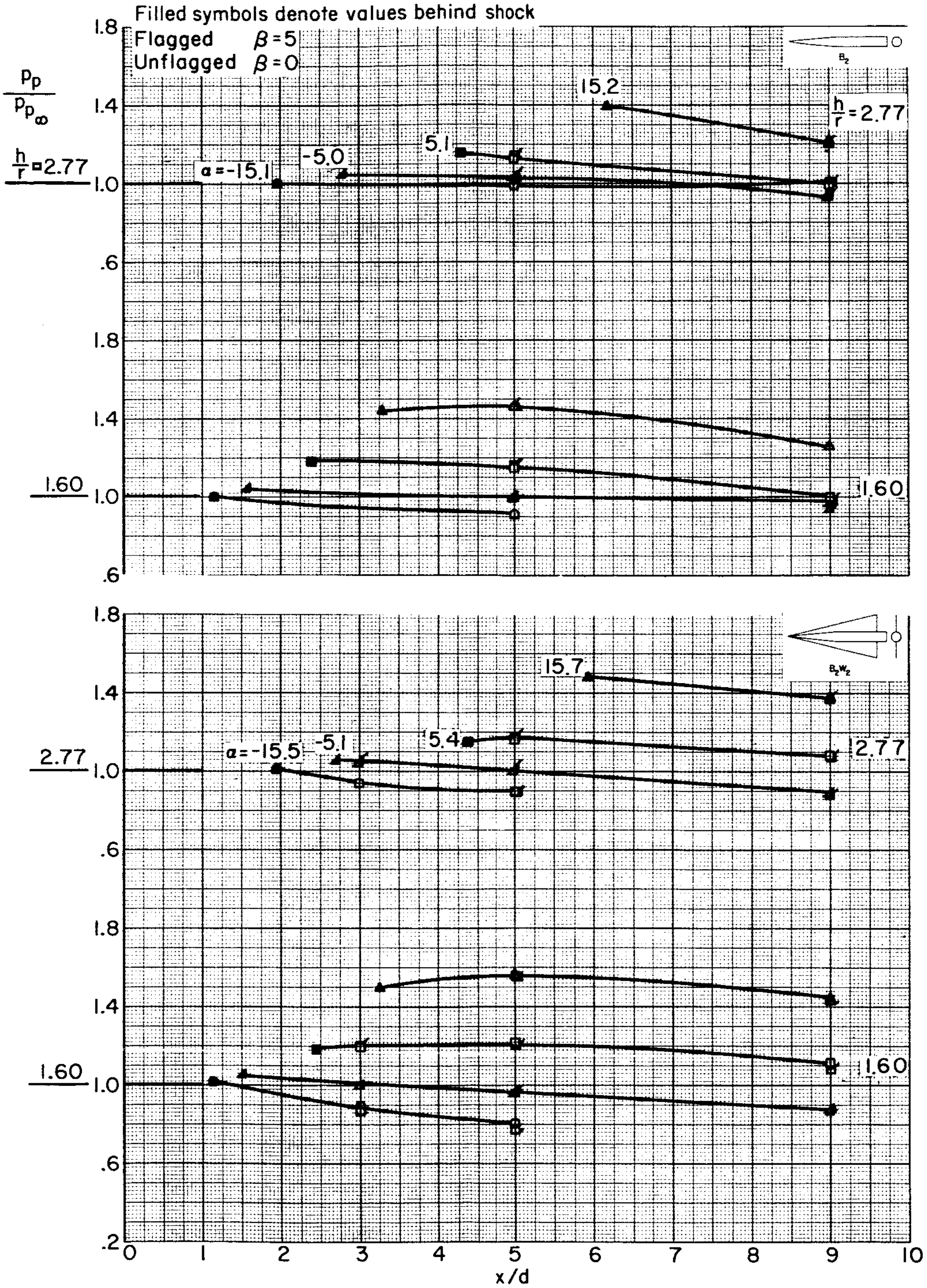

(b) B_2 and B_2W_2

Figure 17.- Concluded.

[redacted]

[redacted]

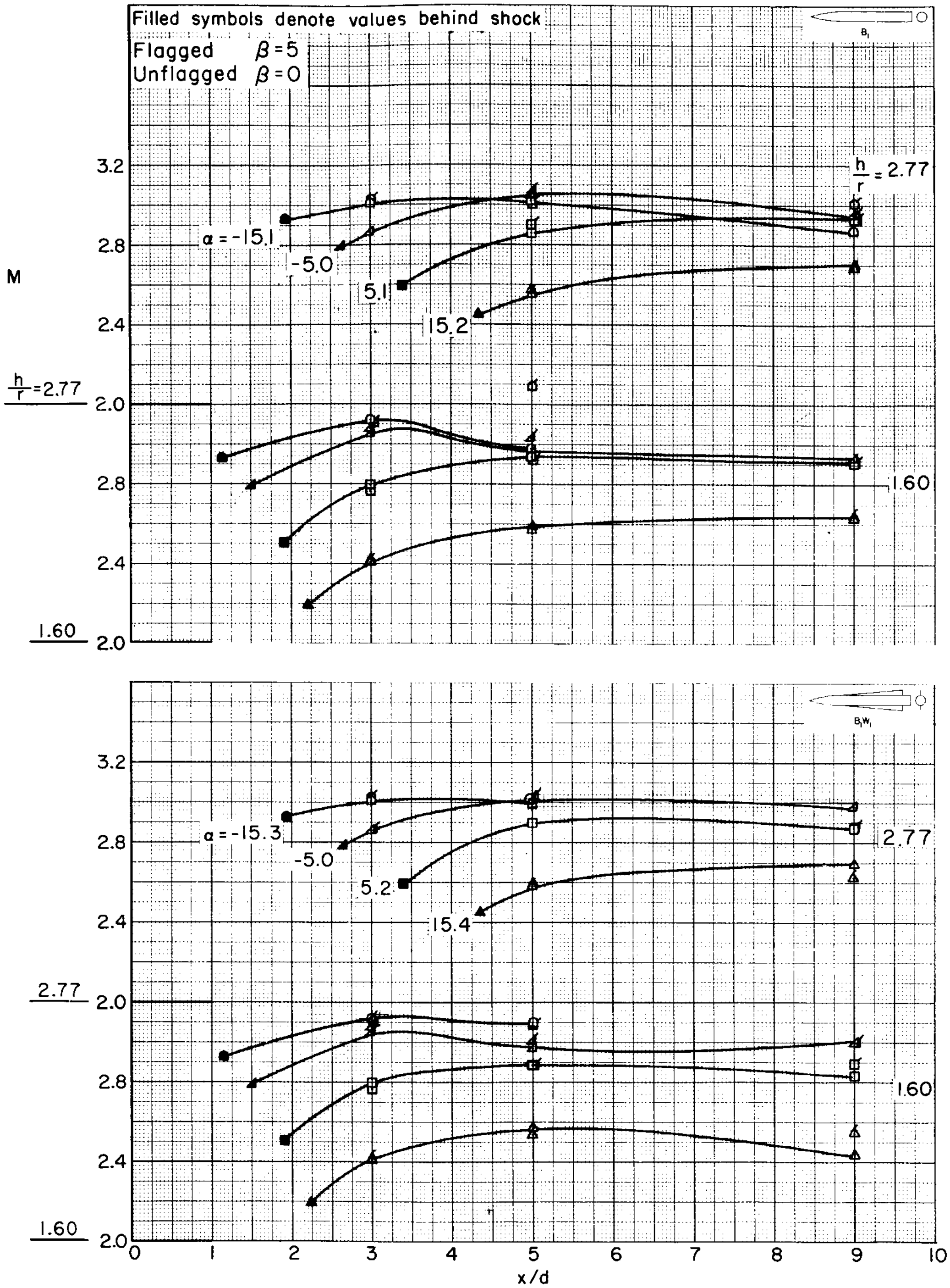

(a) B_1 and W_1

Figure 18.- Comparison of Mach number in vertical plane of symmetry for $\beta = 0^{\circ}$ and 5°, and $M_{\infty} = 2.95$.

[redacted]

DECLASSIFIED

[redacted]

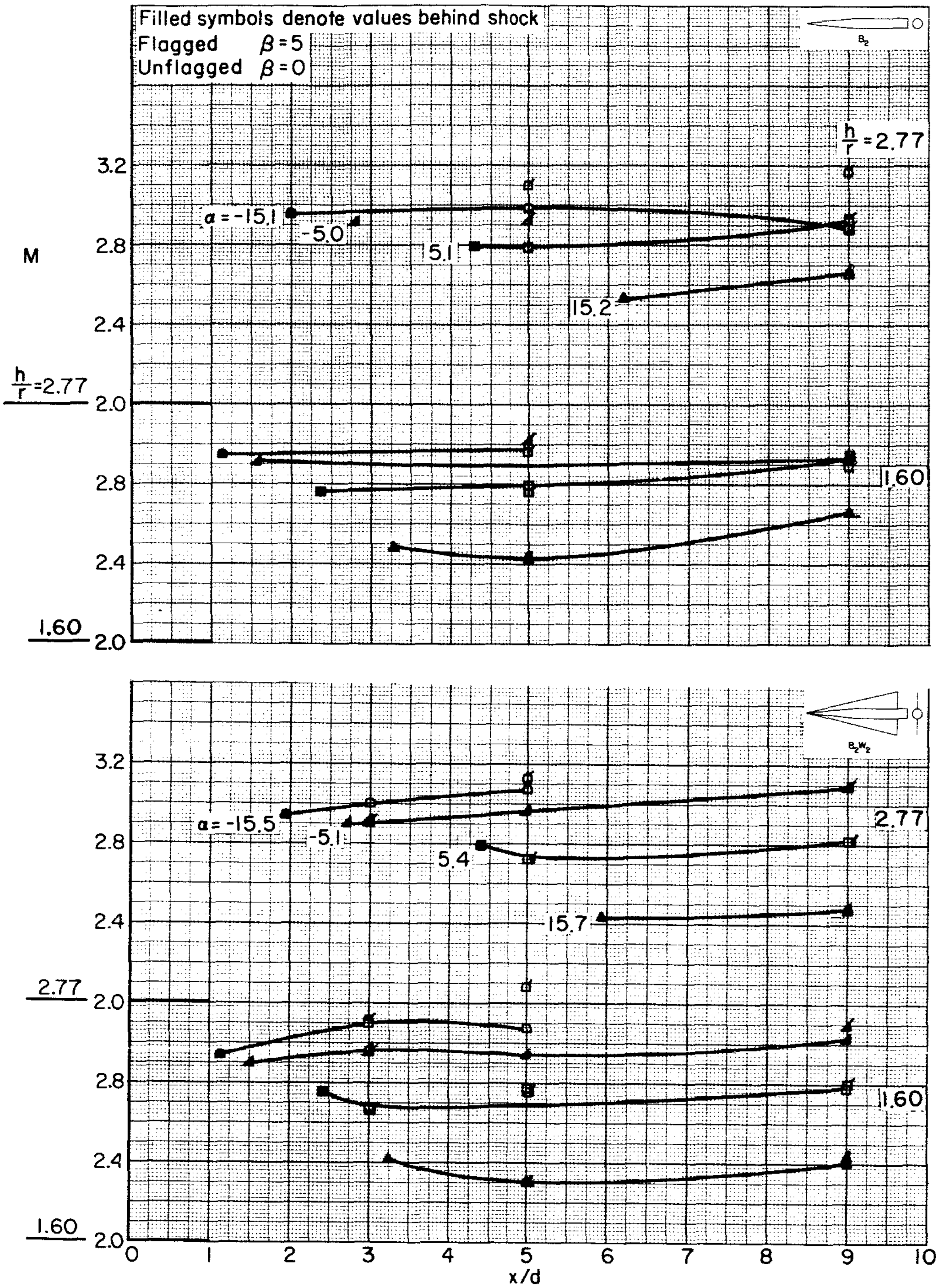

(b) B_2 and B_2W_2

Figure 18.- Concluded.

[redacted]

[redacted]

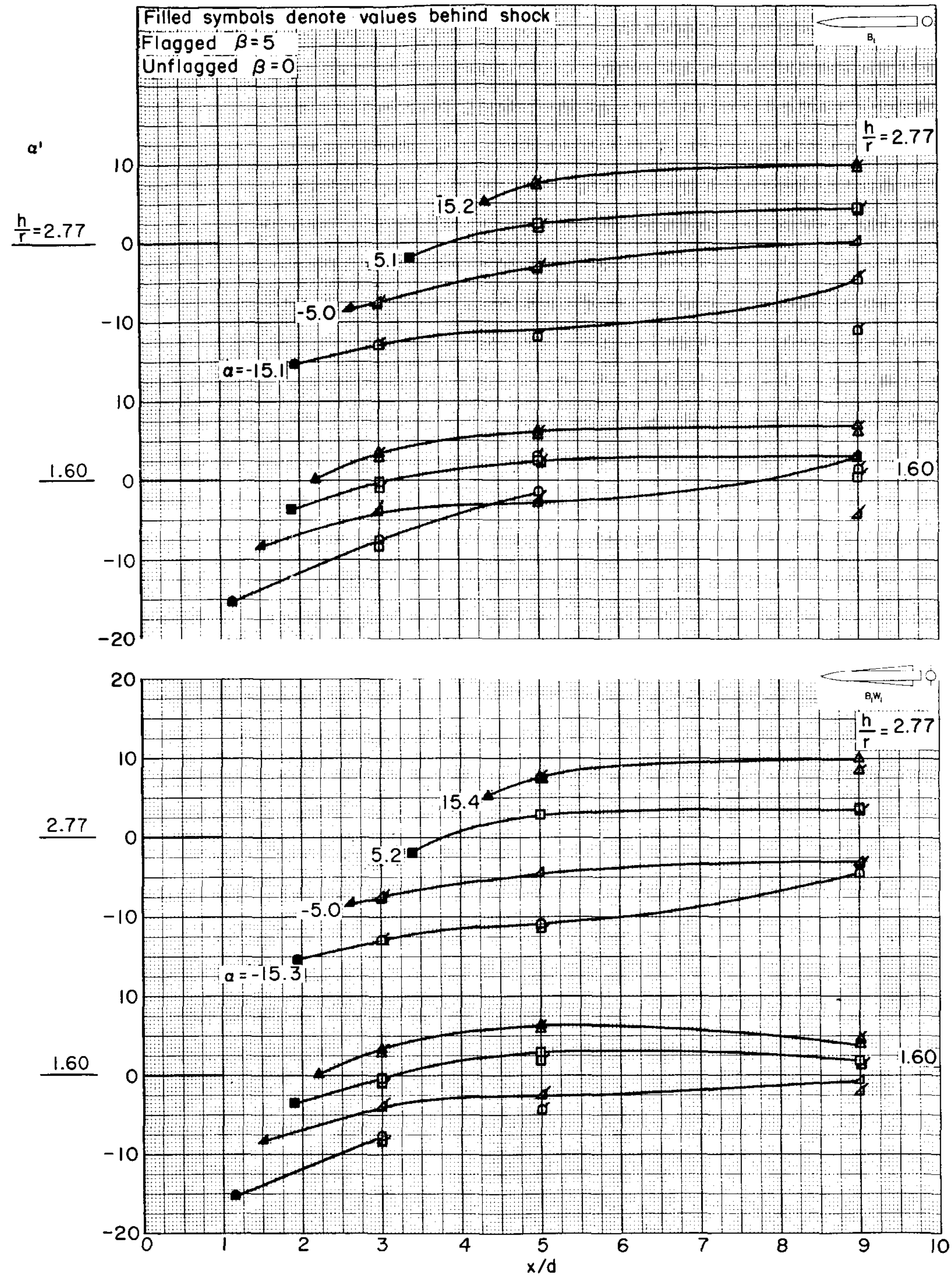

(a) B_1 and B_1W_1

Figure 19.- Comparison of local angle of attack in vertical plane of symmetry for β = 0° and 5°, and M_∞ = 2.95.

[redacted]

[redacted]

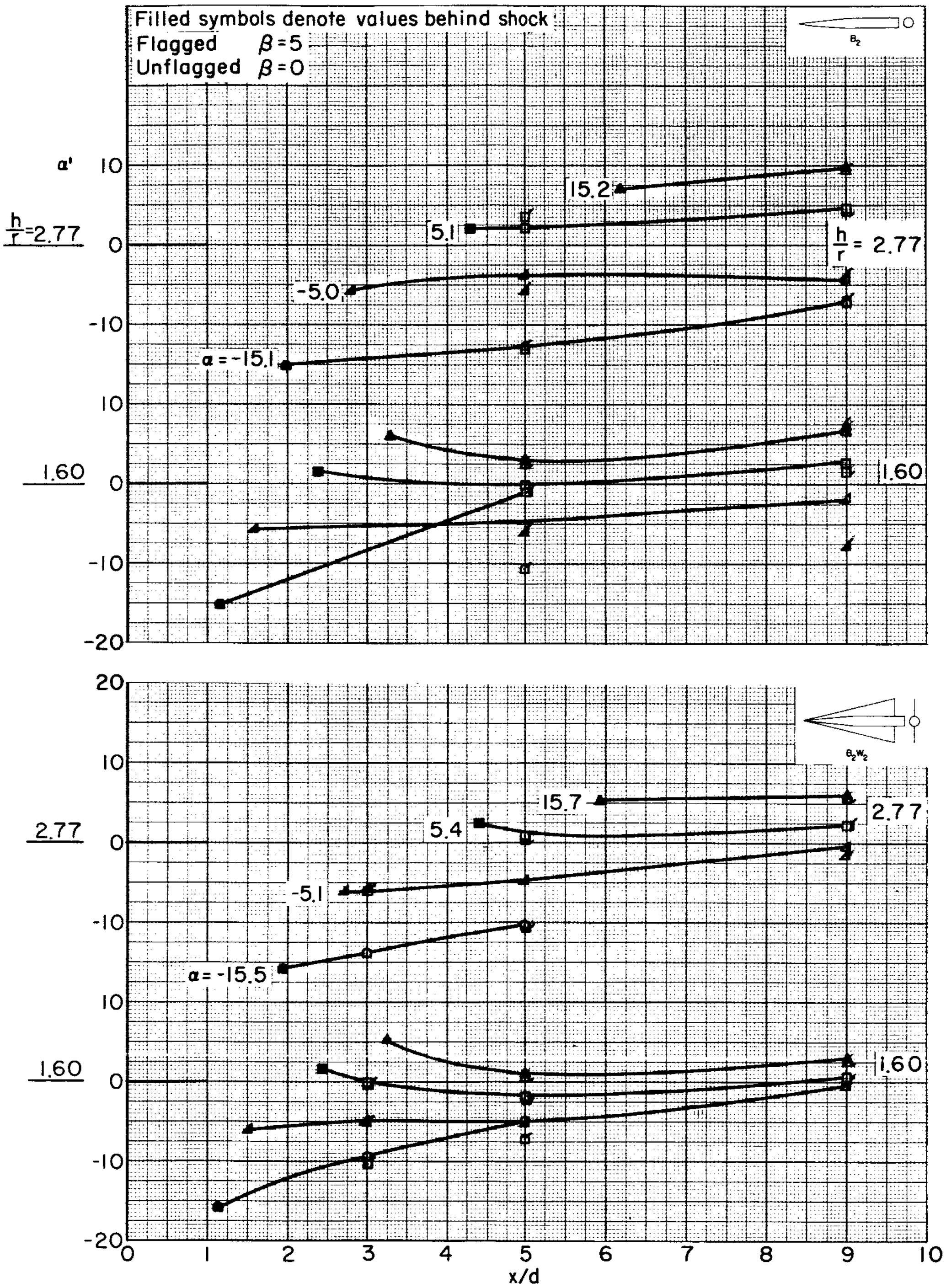

(b) B_2 and B_2W_2

Figure 19.- Concluded.

[redacted]

[redacted]

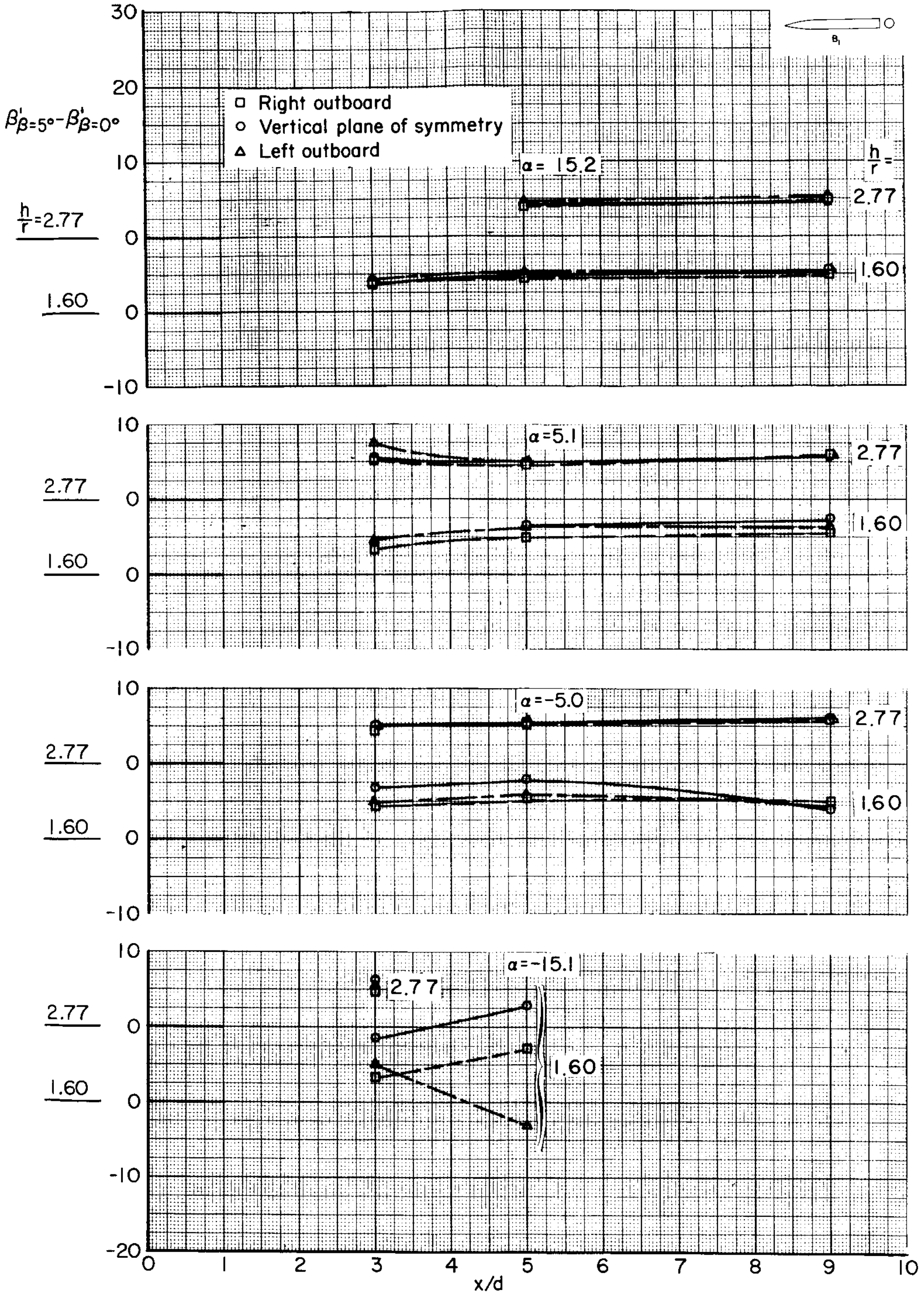

(a) B_1

Figure 20.- Change in local sideslip angle due to 5° change in β; vertical plane of symmetry and outboard planes; $M_\infty = 2.95$.

[redacted]

DECLASSIFIED

[redacted]

A-176

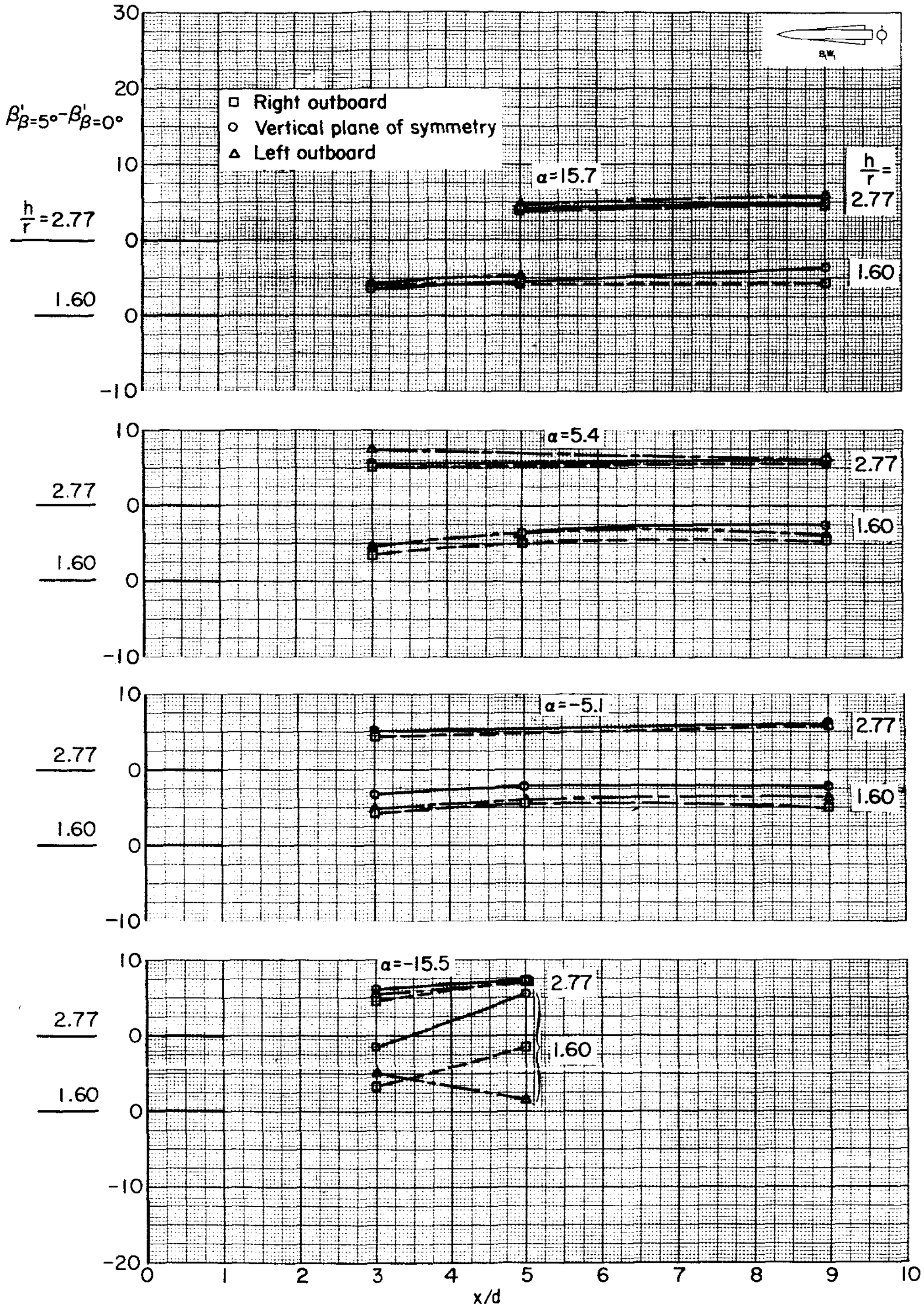

(b) B_1W_1

Figure 20.- Continued.

[redacted]

[redacted]

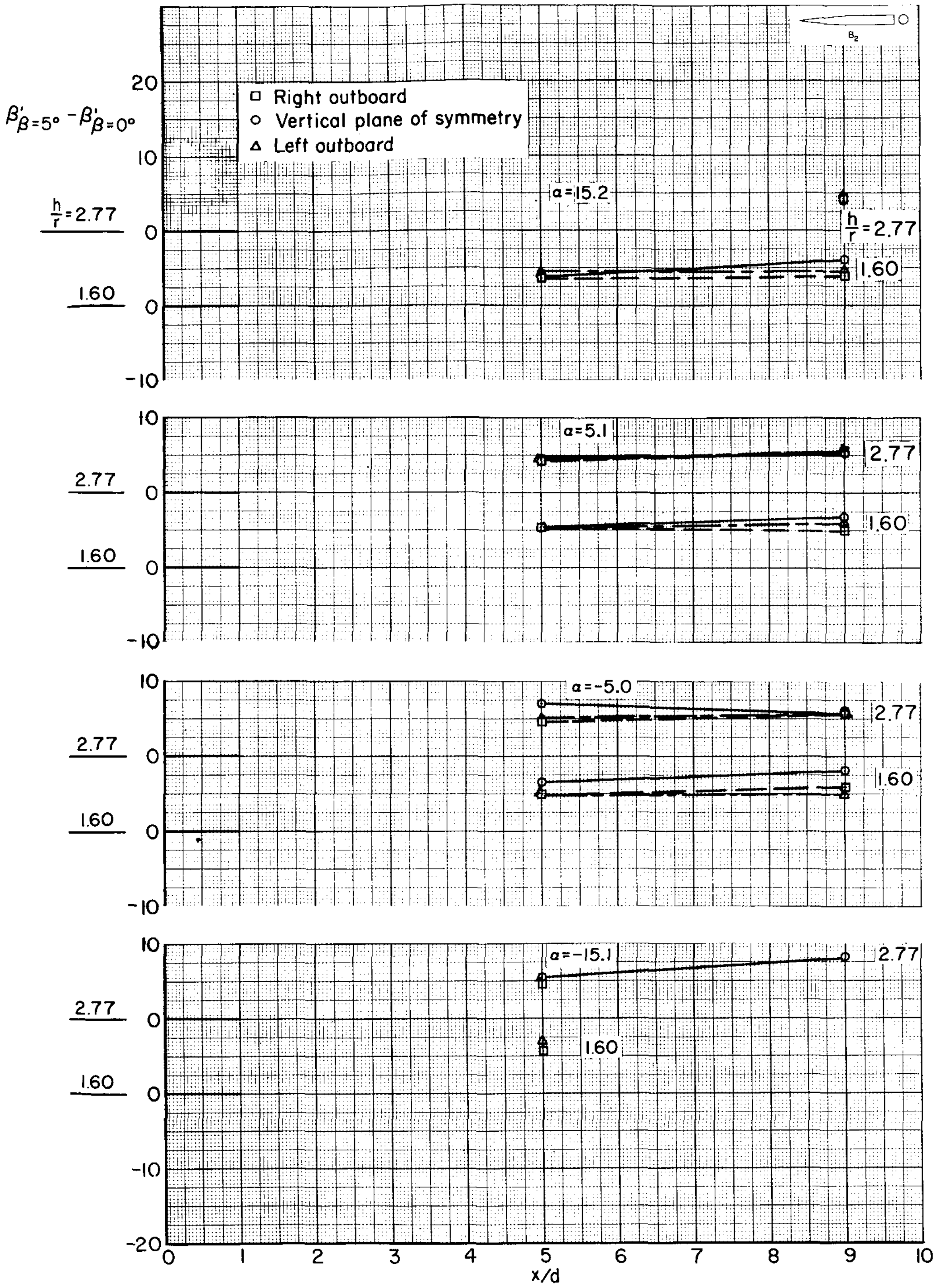

(c) B_2

Figure 20.- Continued.

[redacted]

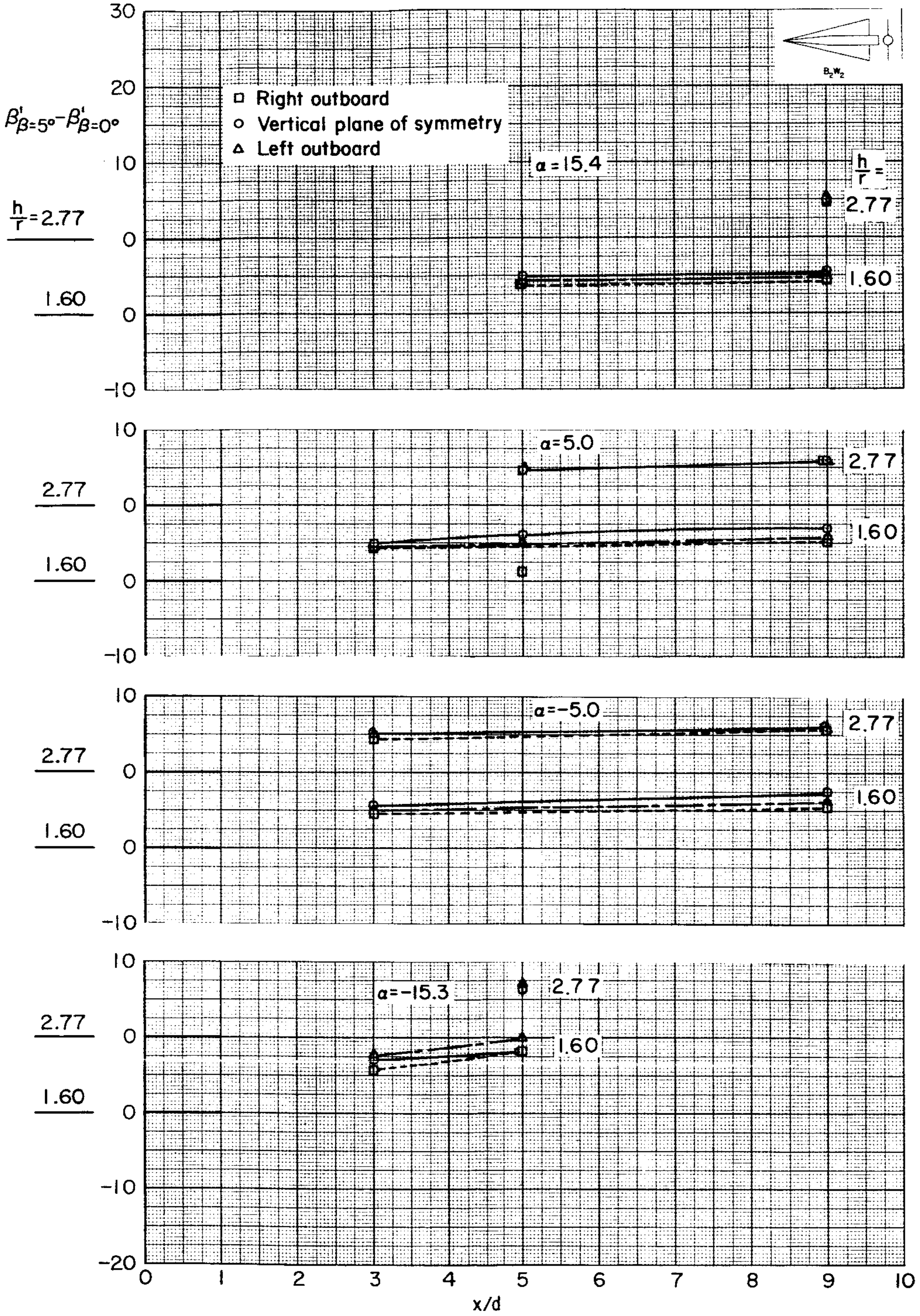

(d) B_2W_2

Figure 20.- Concluded.

[redacted]

[redacted]

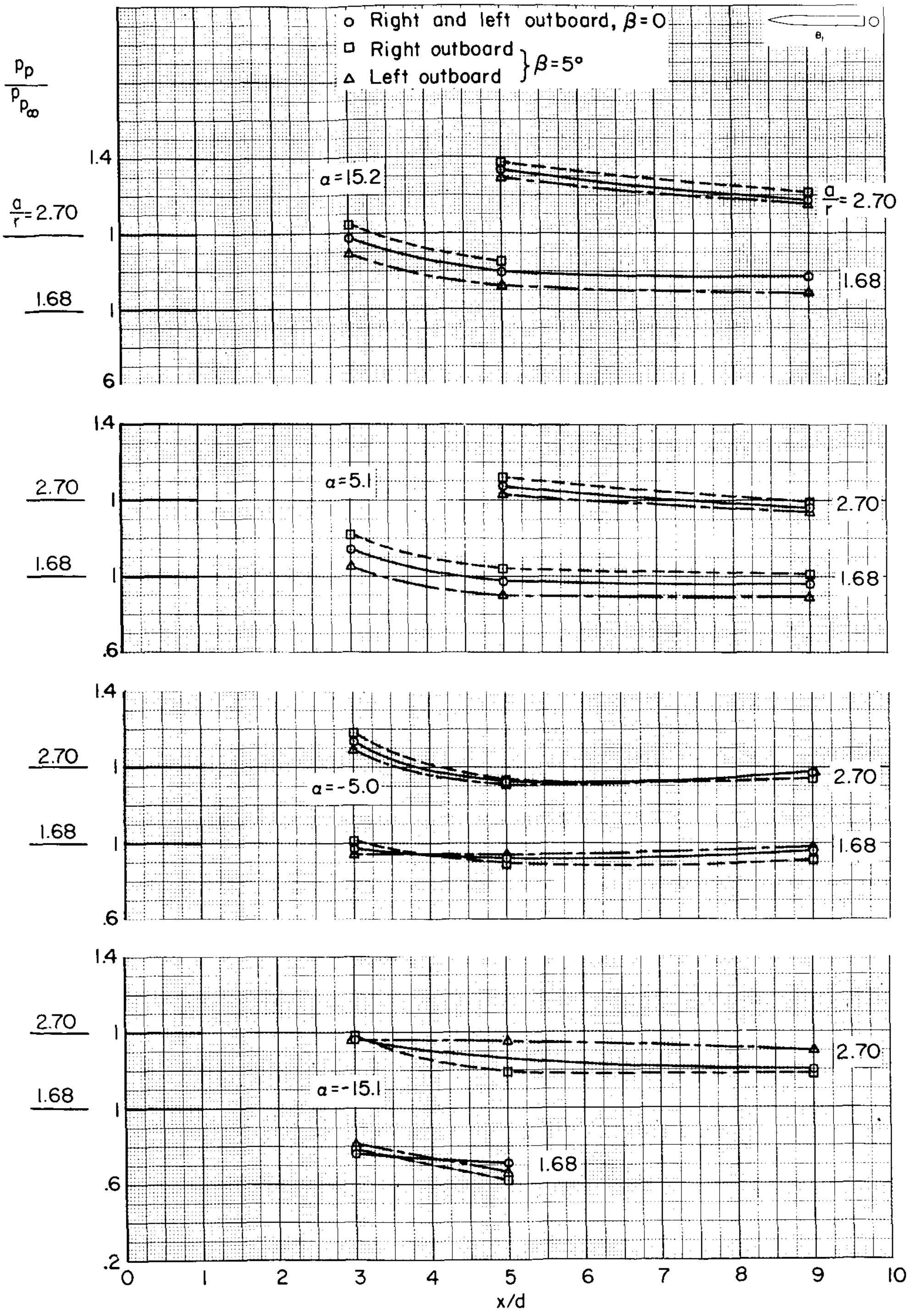

(a) B_1

Figure 21.- Comparison of pitot-pressure ratio in outboard vertical planes for $\beta = 0^\circ$ and 5°, and $M_\infty = 2.95$.

[redacted]

DECLASSIFIED

[redacted]

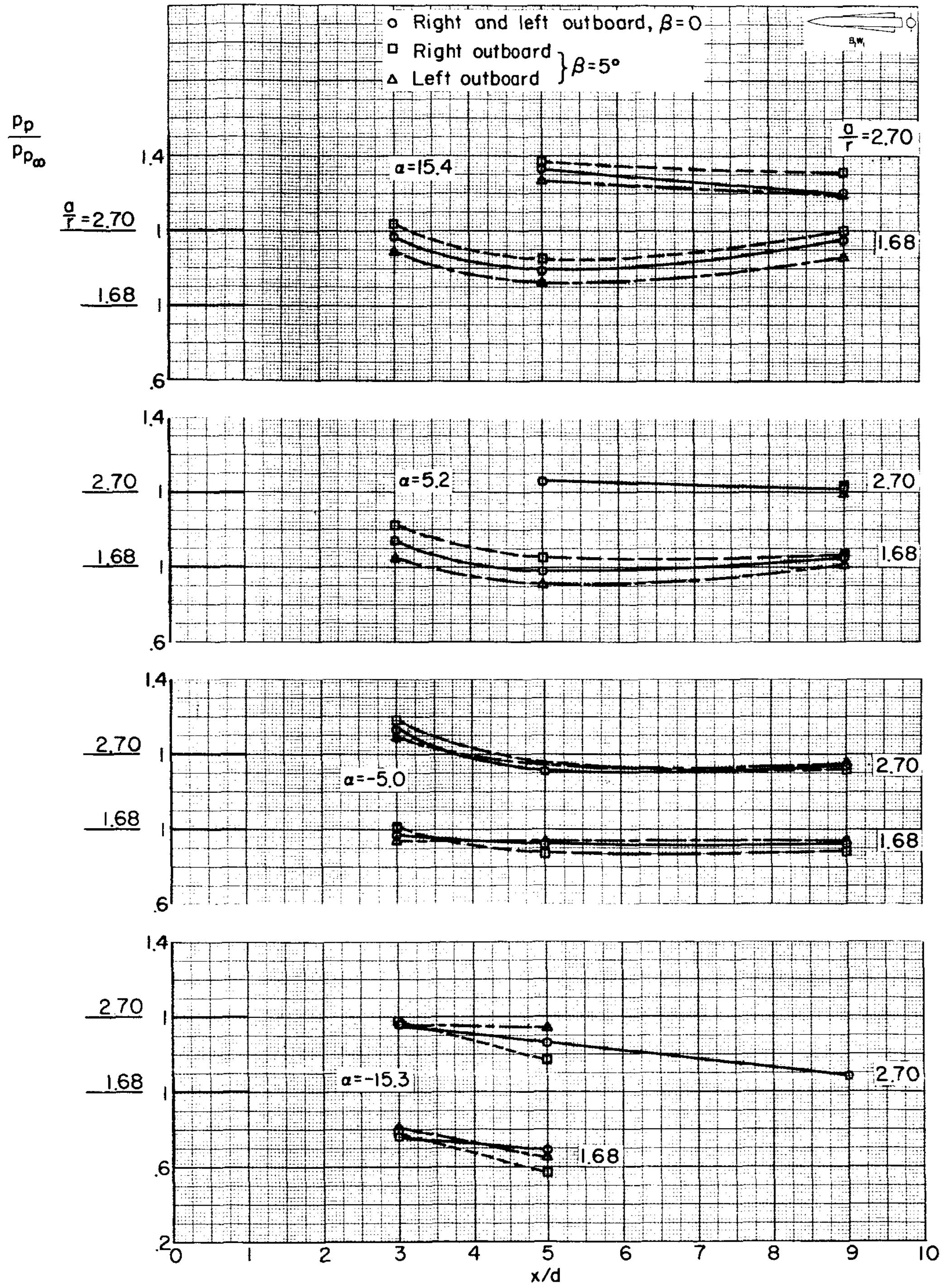

(b) B_1W_1

Figure 21.- Continued.

[redacted]

[redacted]

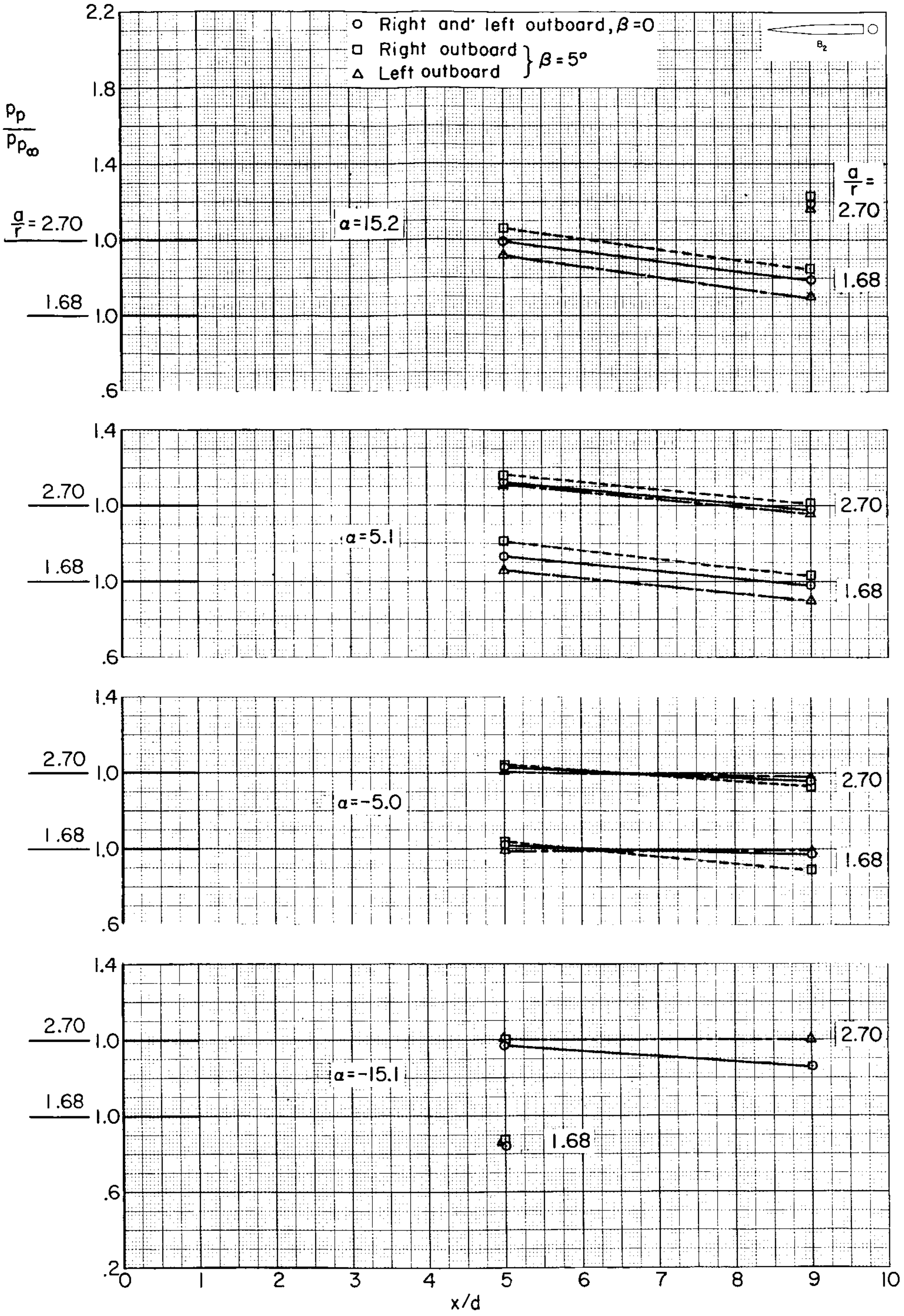

(c) B_2

Figure 21.- Continued.

[redacted]

[redacted]

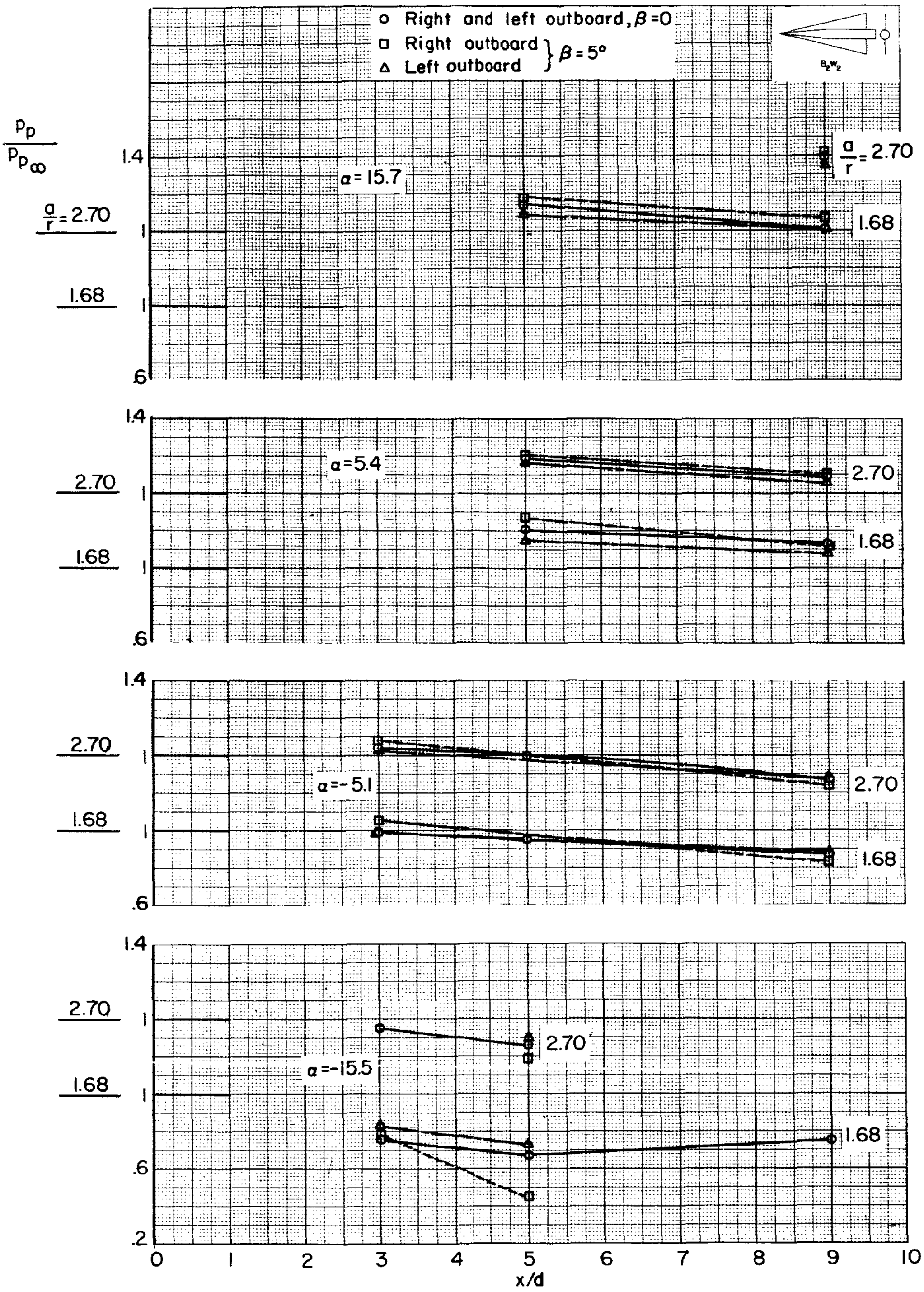

(d) B_2W_2

Figure 21.- Concluded.

[redacted]

[redacted]

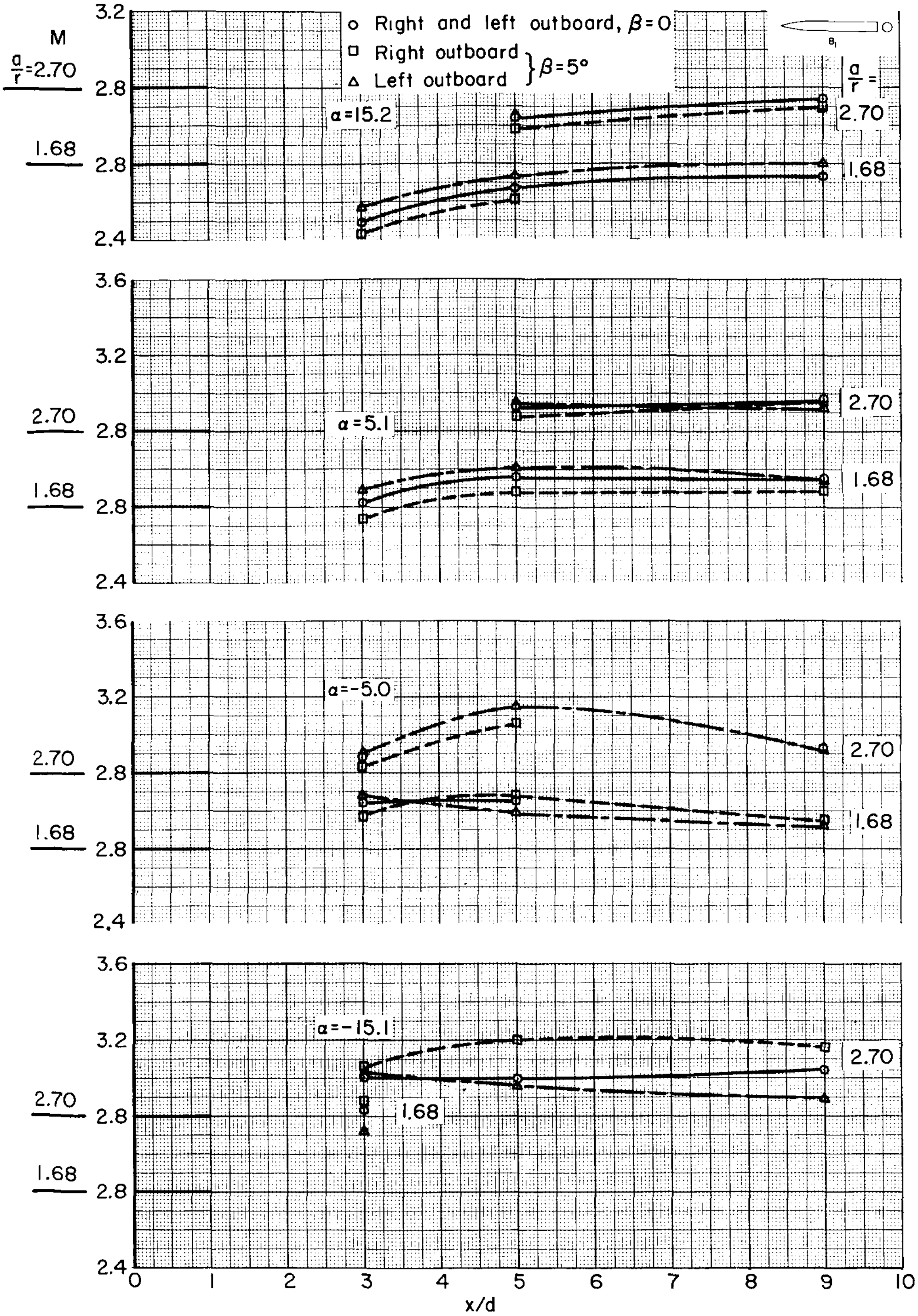

(a) B_1

Figure 22.- Comparison of Mach number in outboard vertical planes for $\beta = 0^{\circ}$ and 5°, and $M_{\infty} = 2.95$.

[redacted]

DECLASSIFIED

[redacted]

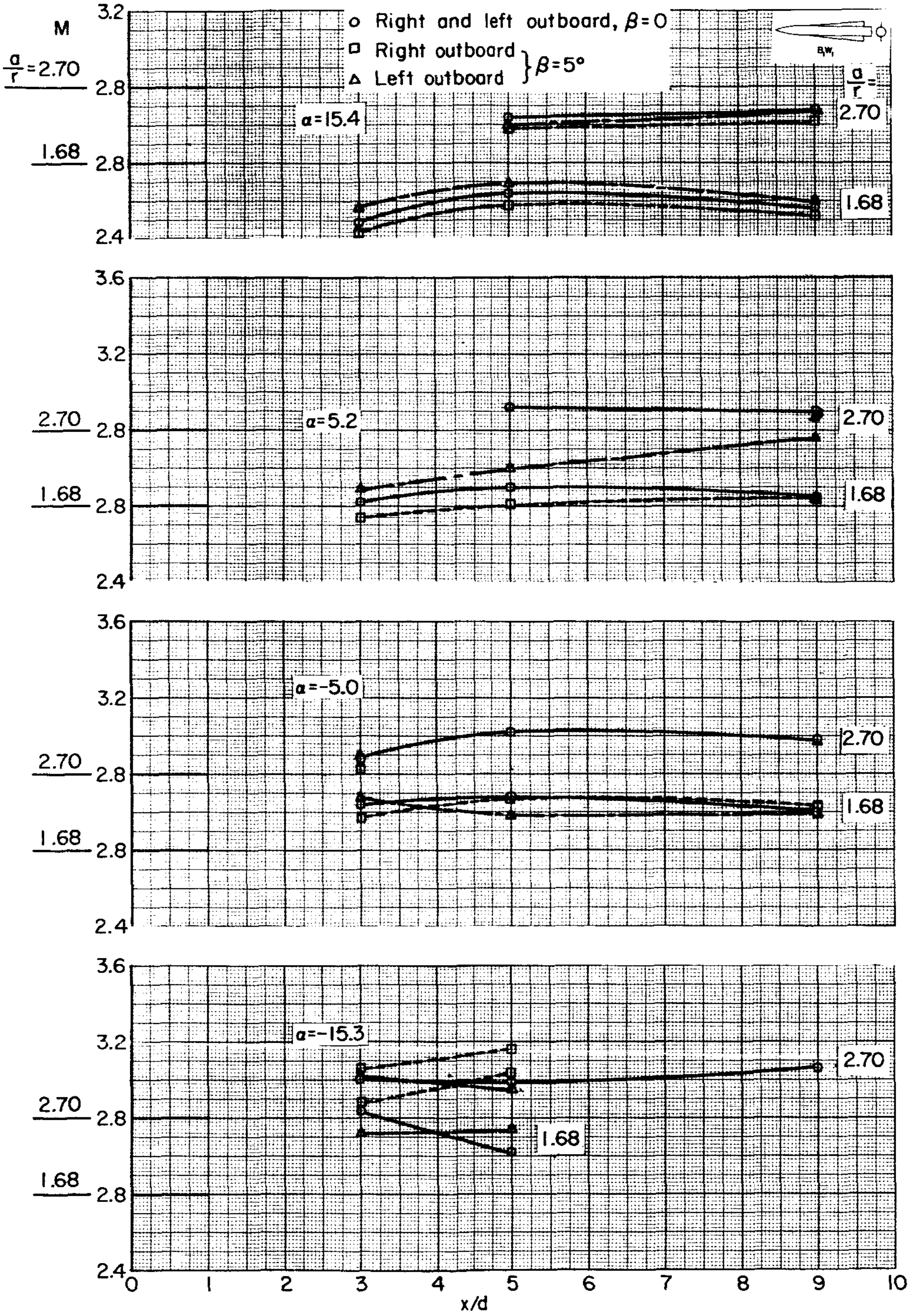

(b) B_1W_1

Figure 22.- Continued.

[redacted]

[redacted]

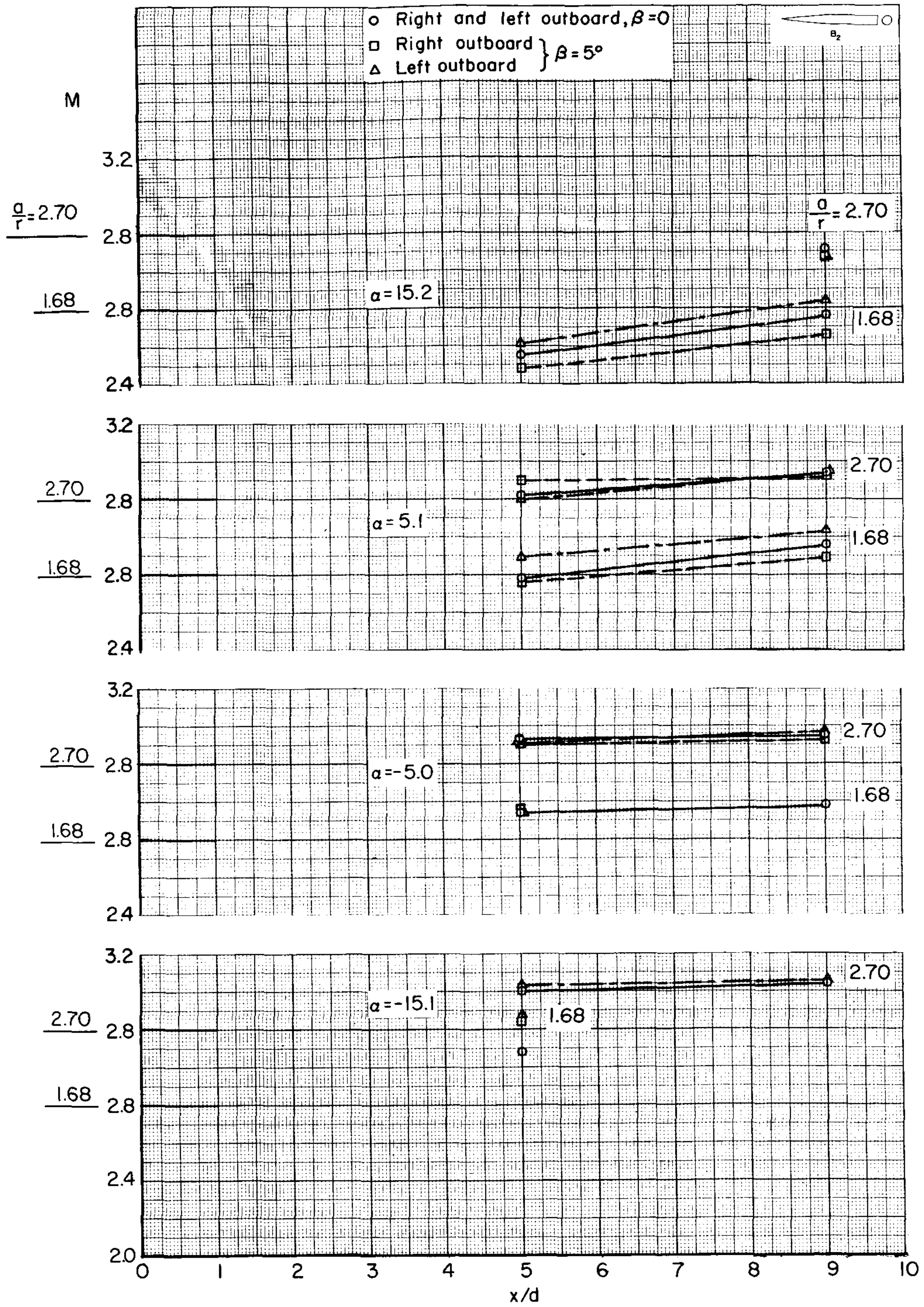

(c) B_2

Figure 22.- Continued.

[redacted]

[redacted]

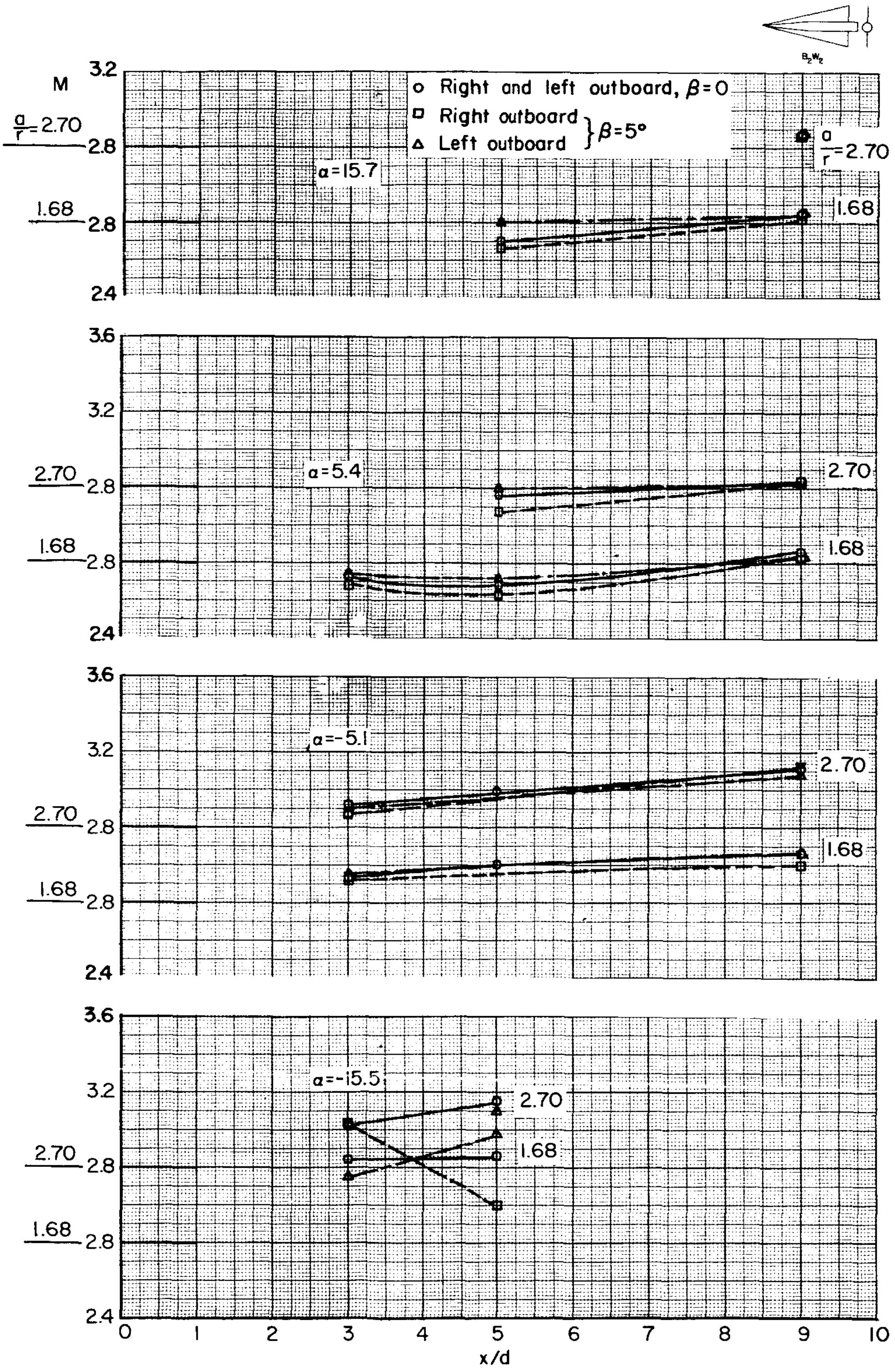

(d) B_2W_2

Figure 22.- Concluded.

[redacted]

[redacted]

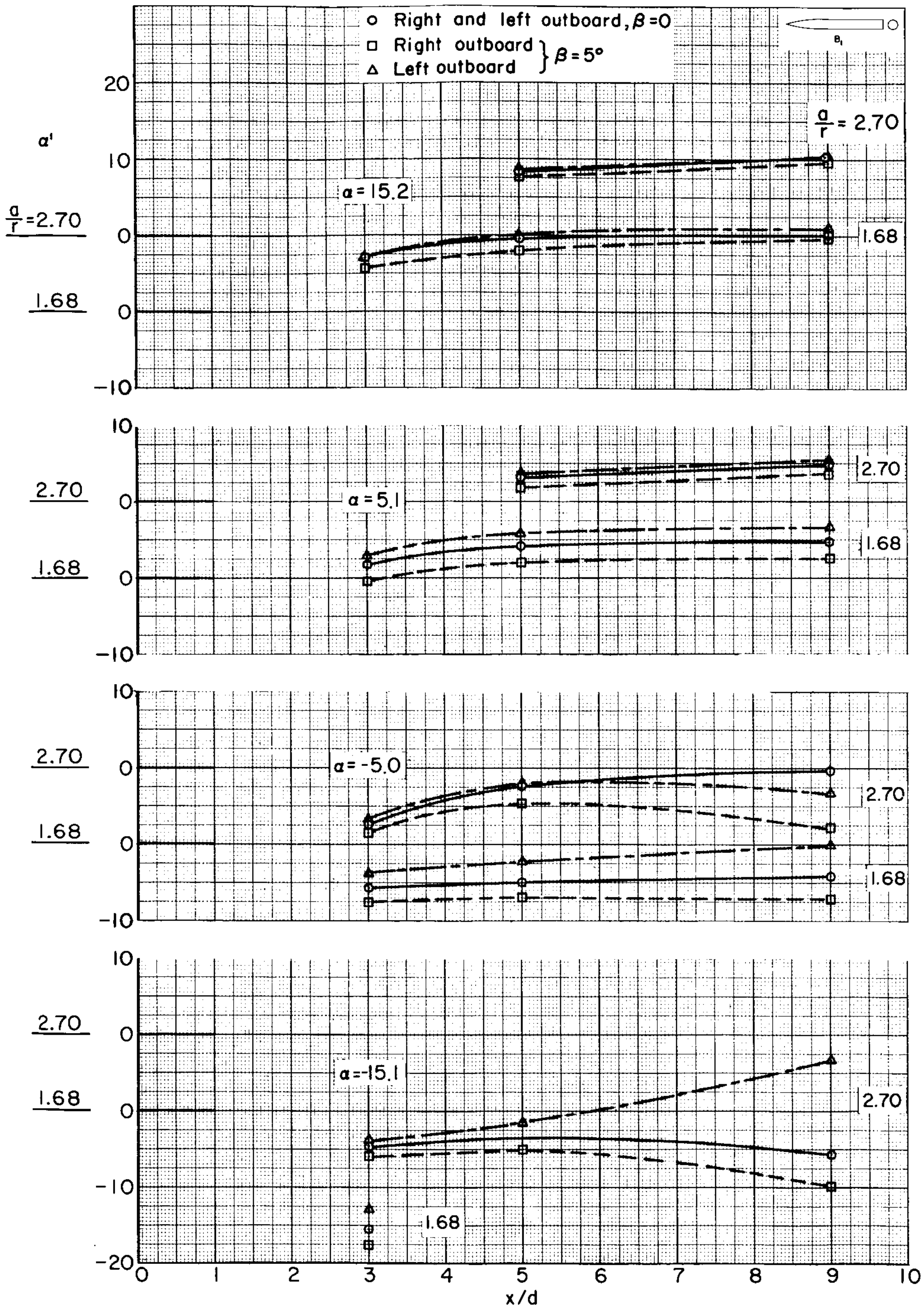

(a) B_1

Figure 23.- Comparison of local angle of attack in outboard vertical planes for $\beta = 0^{\circ}$ and 5°, and $M_{\infty} = 2.95$.

[redacted]

[redacted]

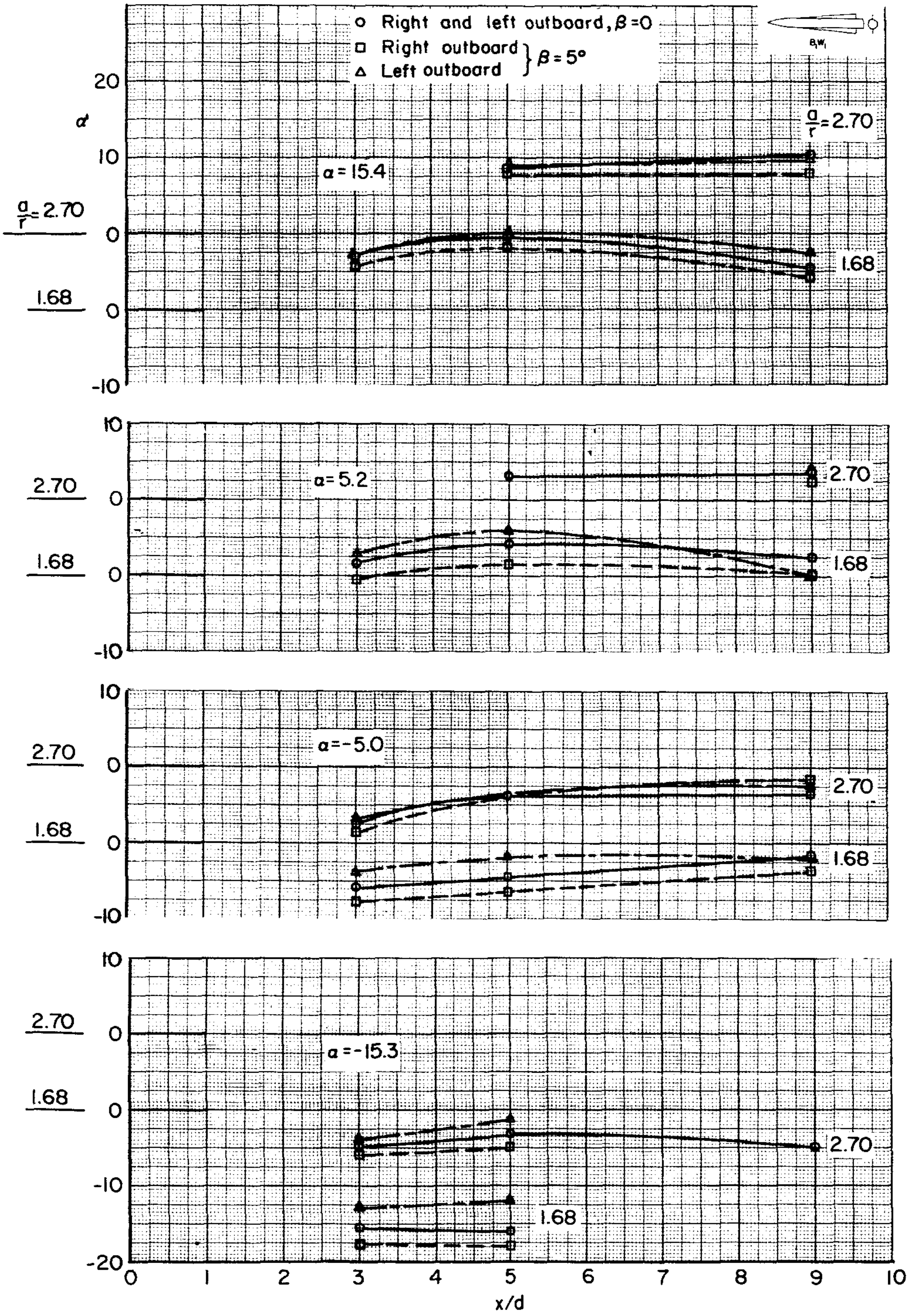

(b) B_1W_1

Figure 23.- Continued.

[redacted]

[redacted]

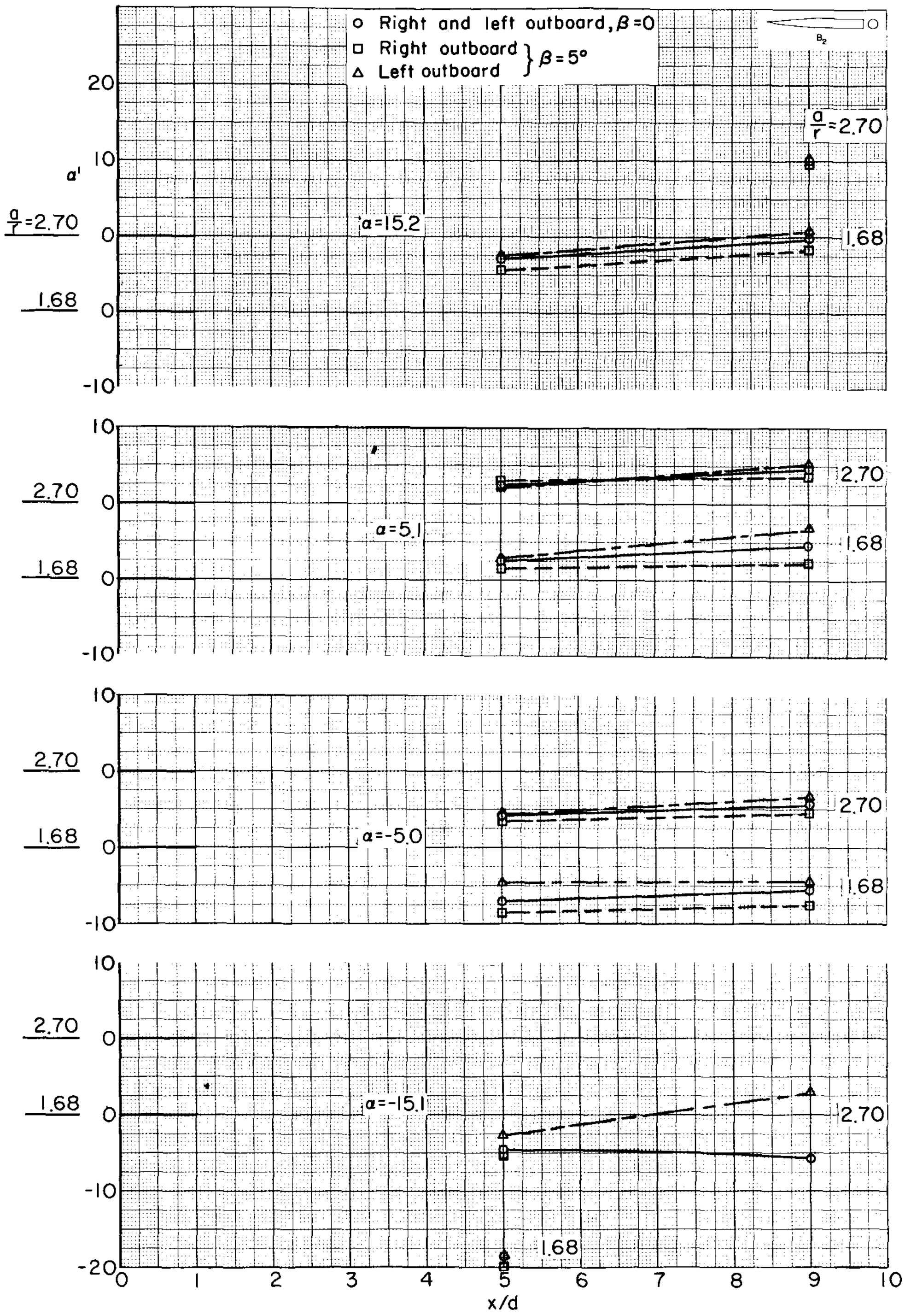

(c) B_2

Figure 23.- Continued.

[redacted]

1F

DECLASSIFIED

[redacted]

A-170

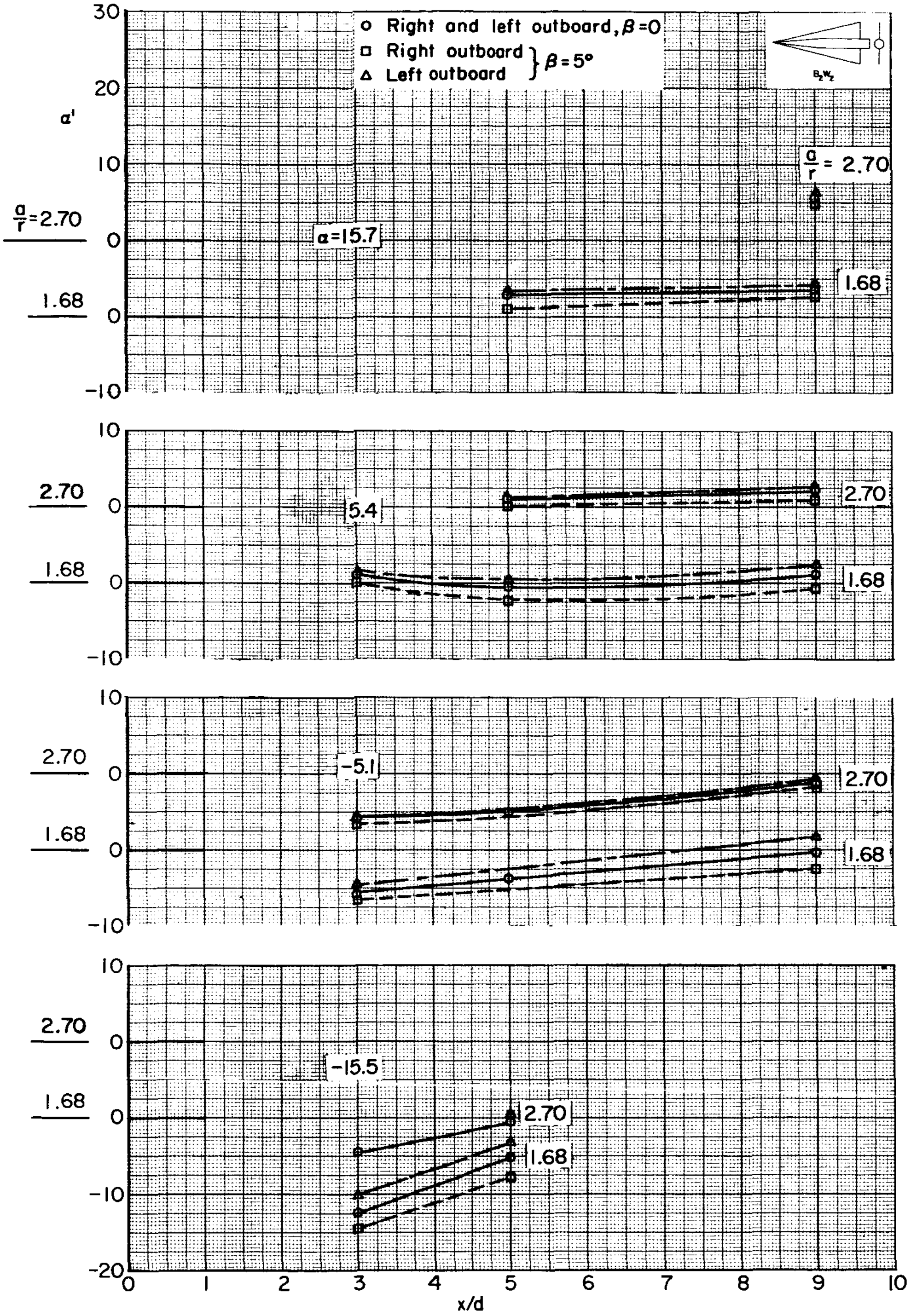

[redacted] (d) B_2W_2

Figure 23.- Concluded.

[redacted]

[redacted]

[redacted]

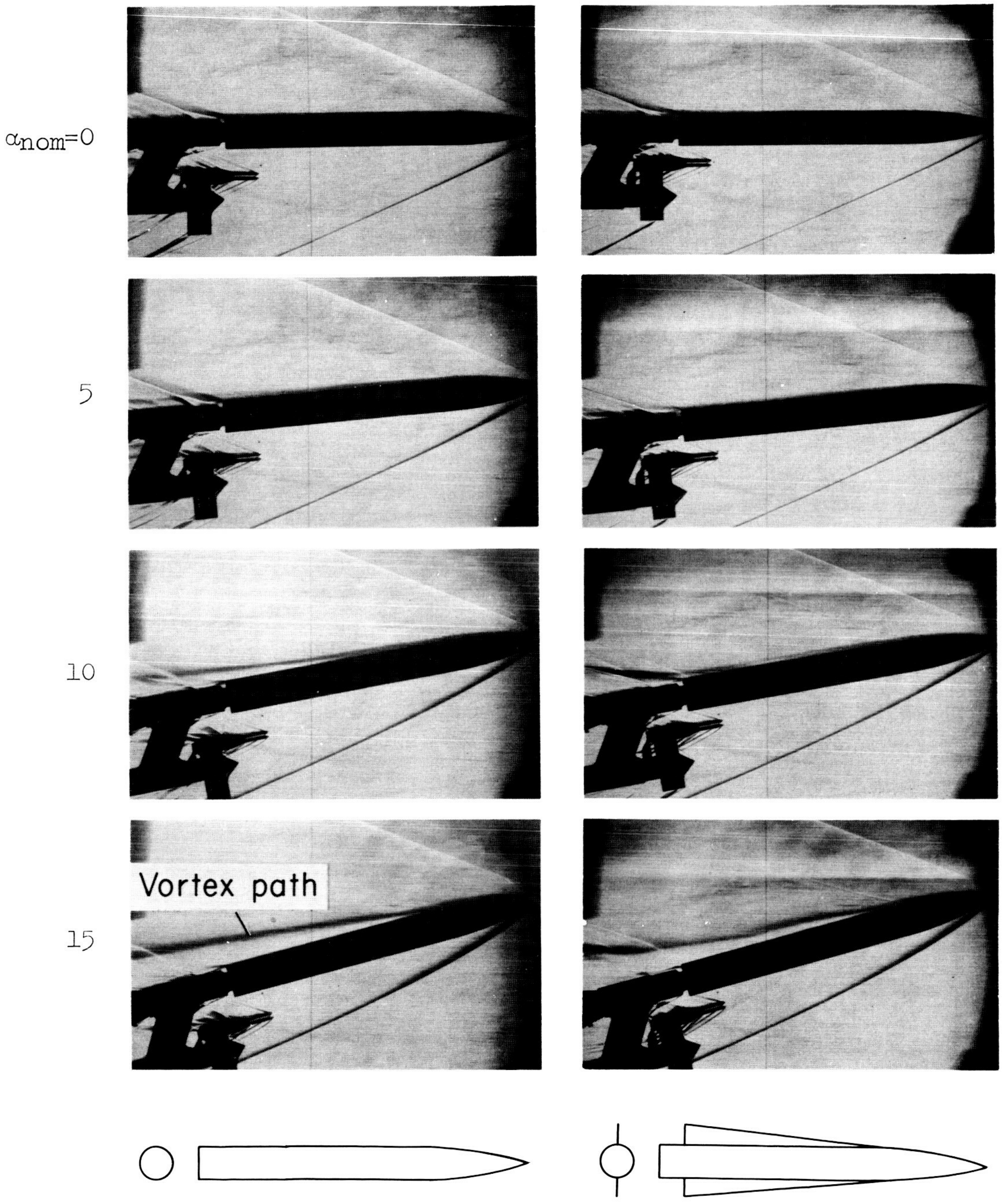

B_1 B_1W_1

(a) Models B_1 and B_1W_1.

Figure 24.- Schlieren photographs of models at $M_\infty = 2.95$ and $\beta = 0^\circ$.

[redacted]

DECLASSIFIED

[redacted]

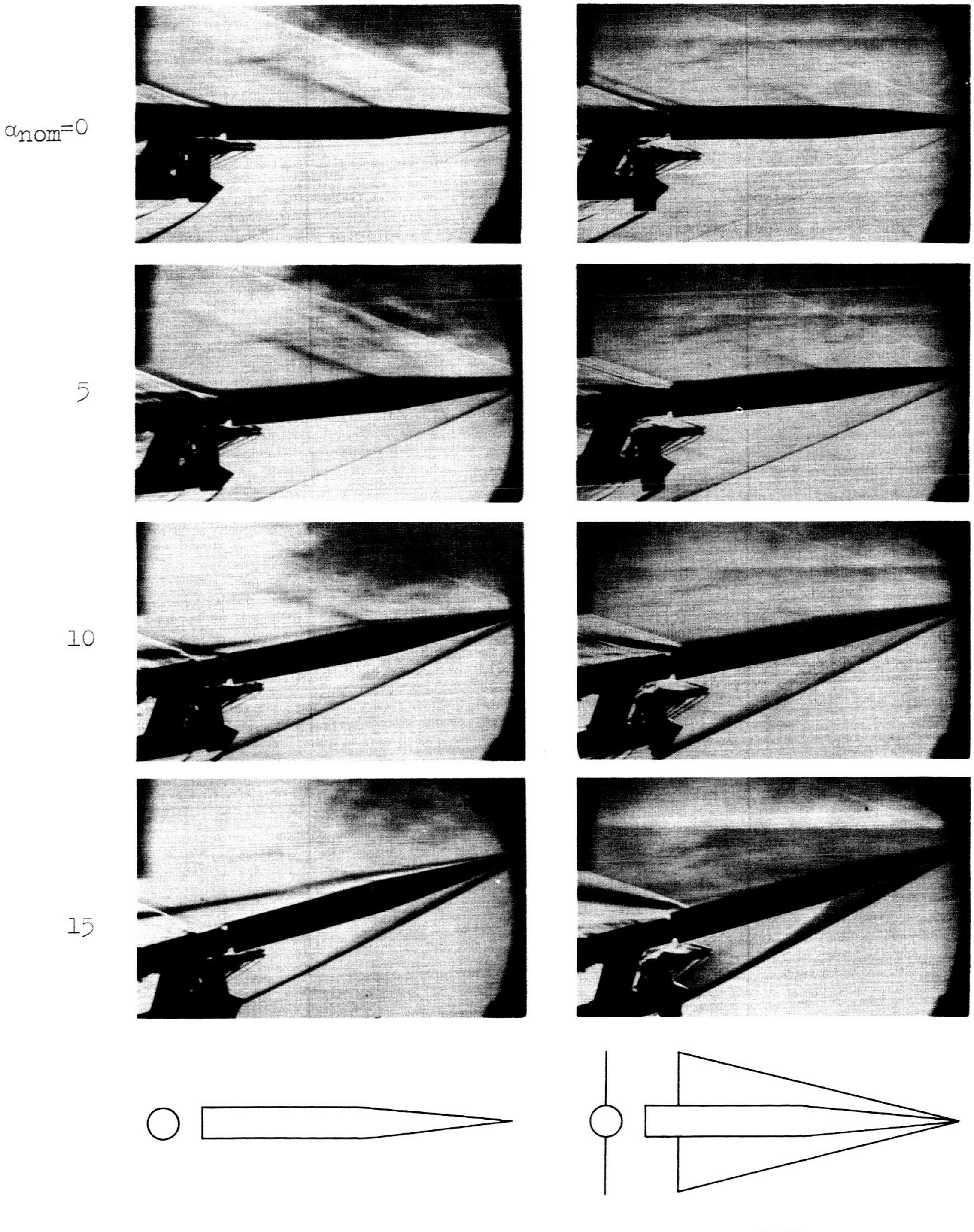

(b) Models B_2 and B_2W_2.

Figure 24.- Concluded.

[redacted]

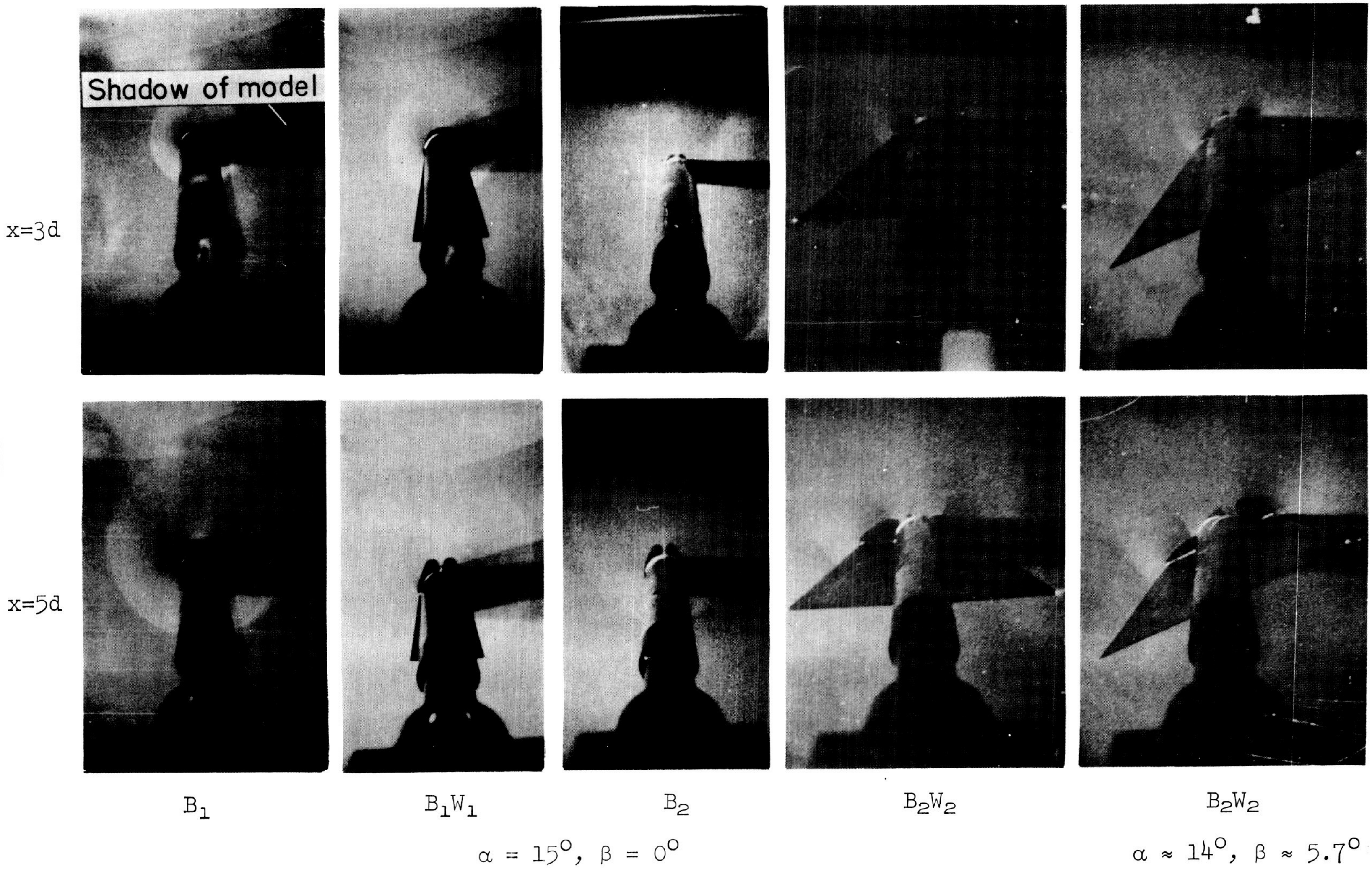

(a) $x = 3d$ and $5d$

Figure 25.- Vapor screen photographs of models: B_1 and B_1W_1 at $M_\infty = 3.3$; B_2 and B_2W_2 at $M_\infty = 2.95$.

[redacted]

[redacted]

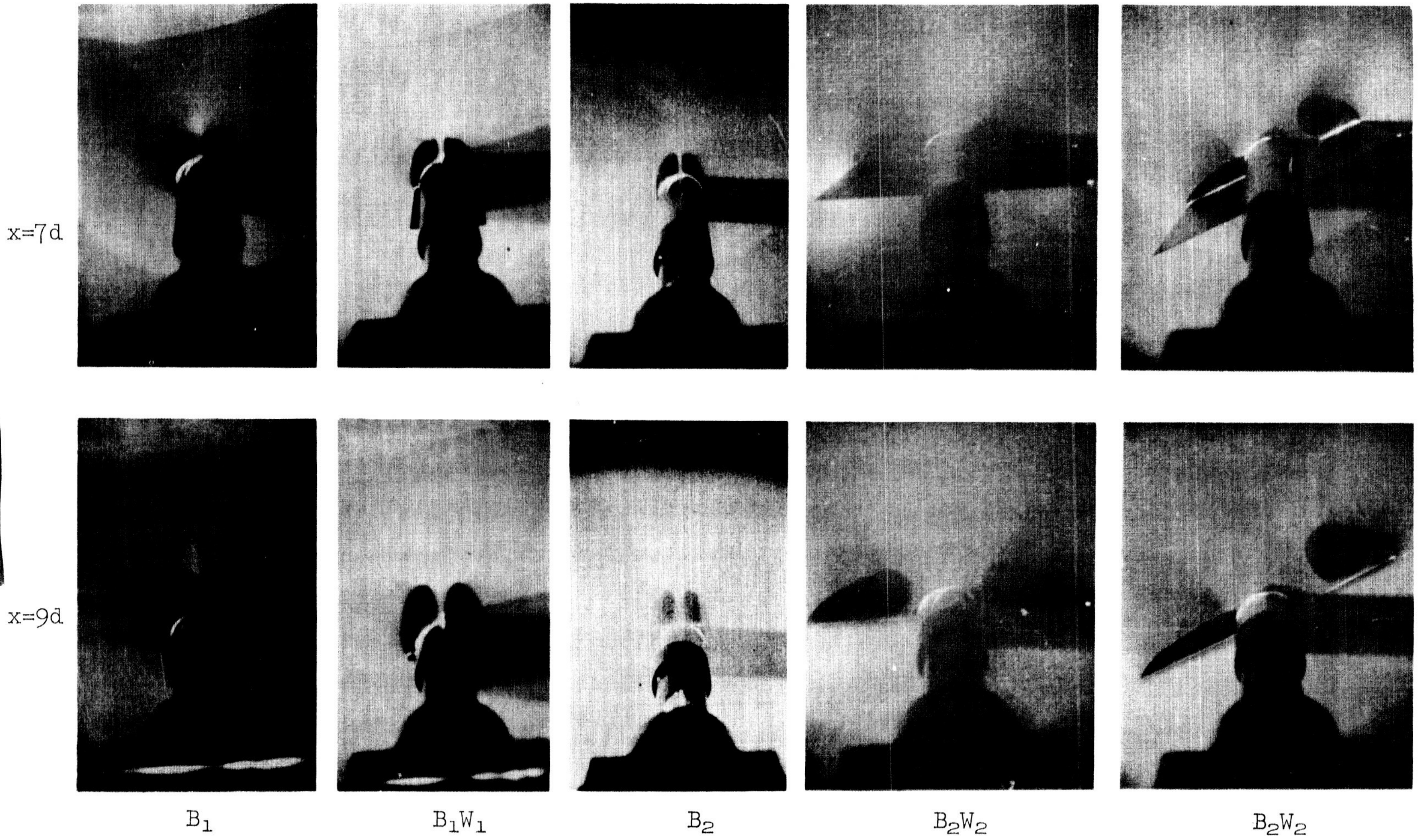

$\alpha = 15^\circ$, $\beta = 0^\circ$

$\alpha \approx 14^\circ$, $\beta \approx 5.7^\circ$

(b) x = 7d and 9d

Figure 25.- Concluded.

[redacted]

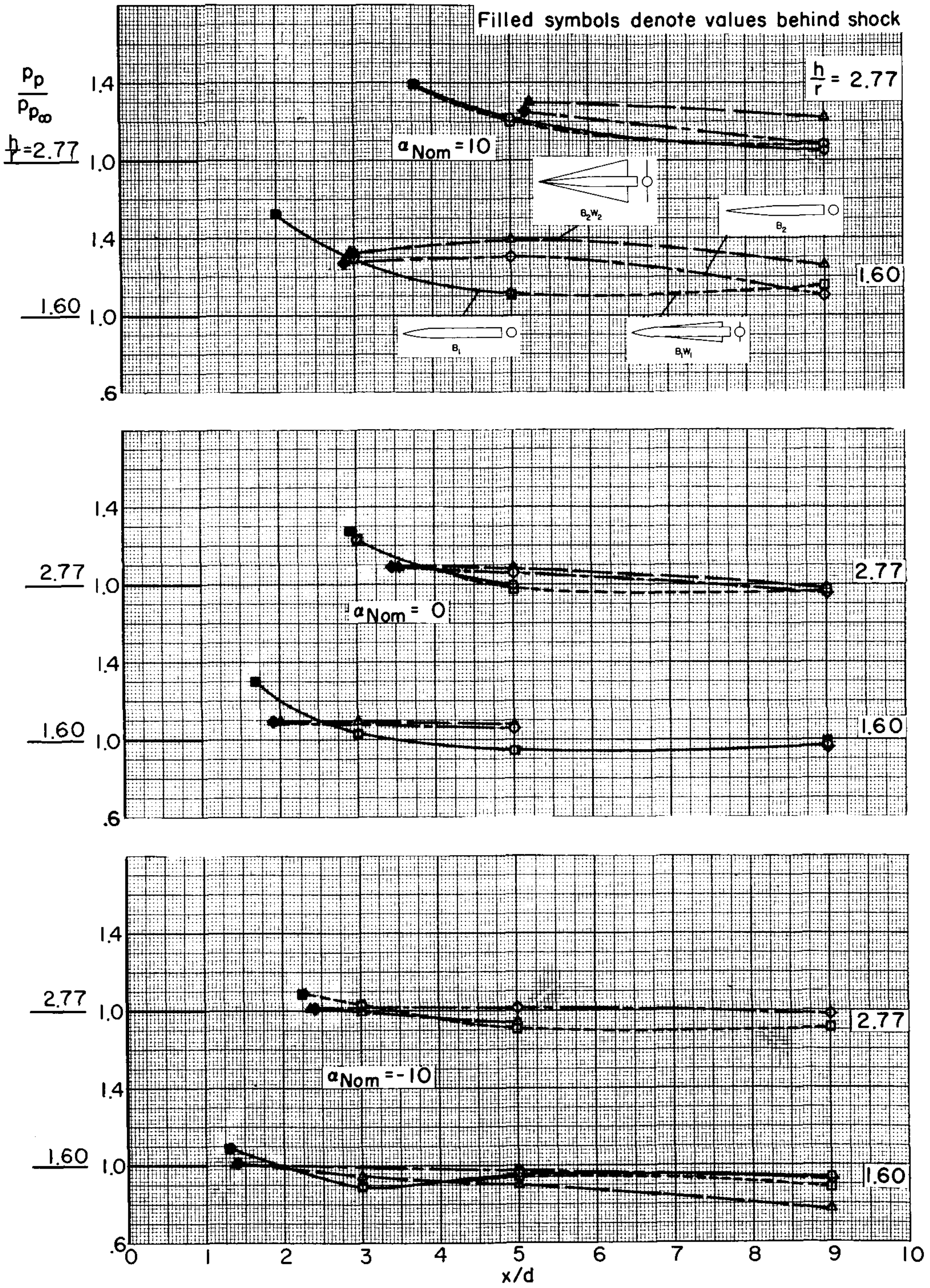

(a) Pitot-pressure ratio.

Figure 26.- Comparison between models of flow characteristics in vertical plane of symmetry for $\beta = 0^\circ$ and $M_\infty = 2.95$.

[redacted]

[redacted]

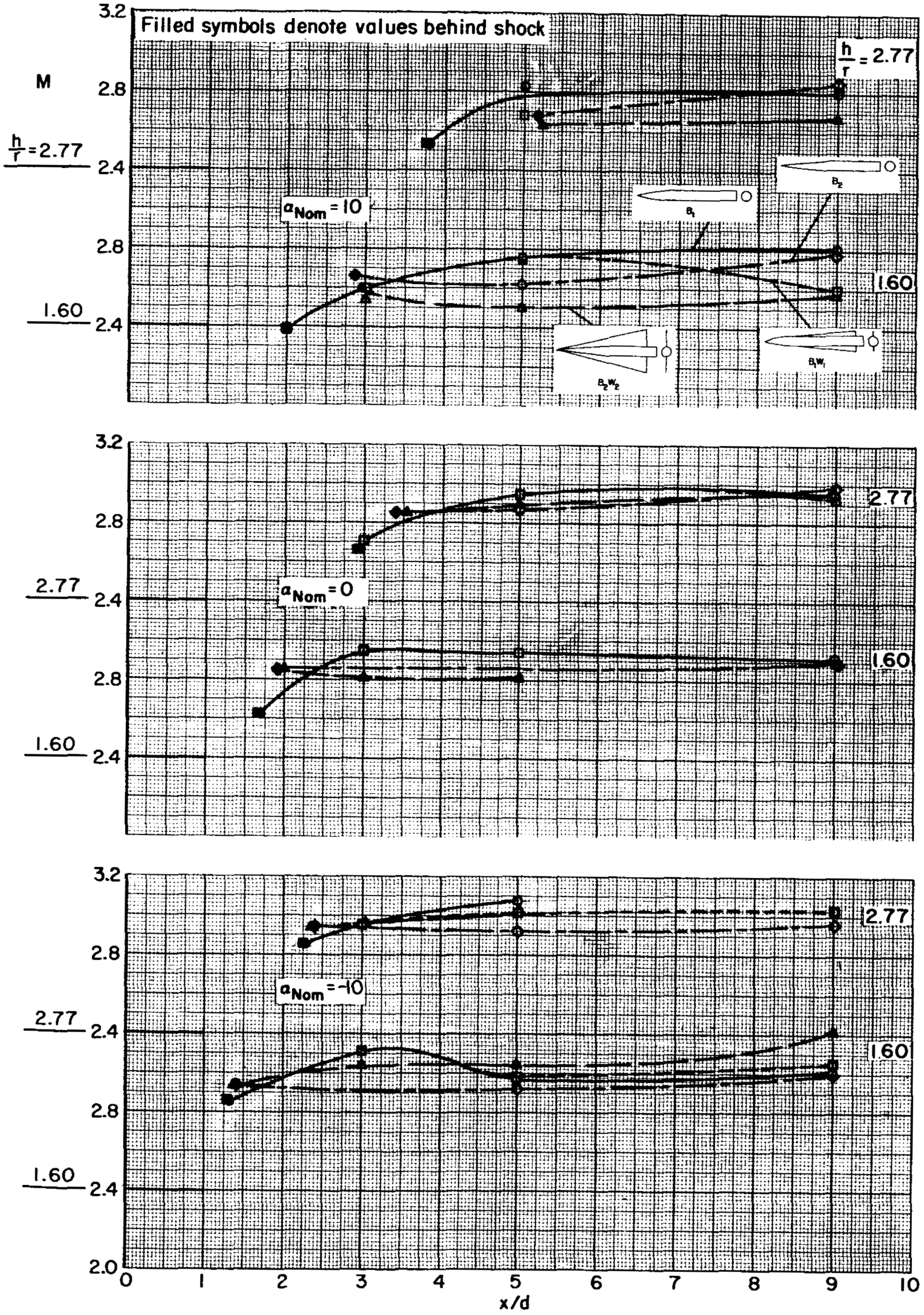

(b) Mach number.

Figure 26.- Continued.

[redacted]

[redacted]

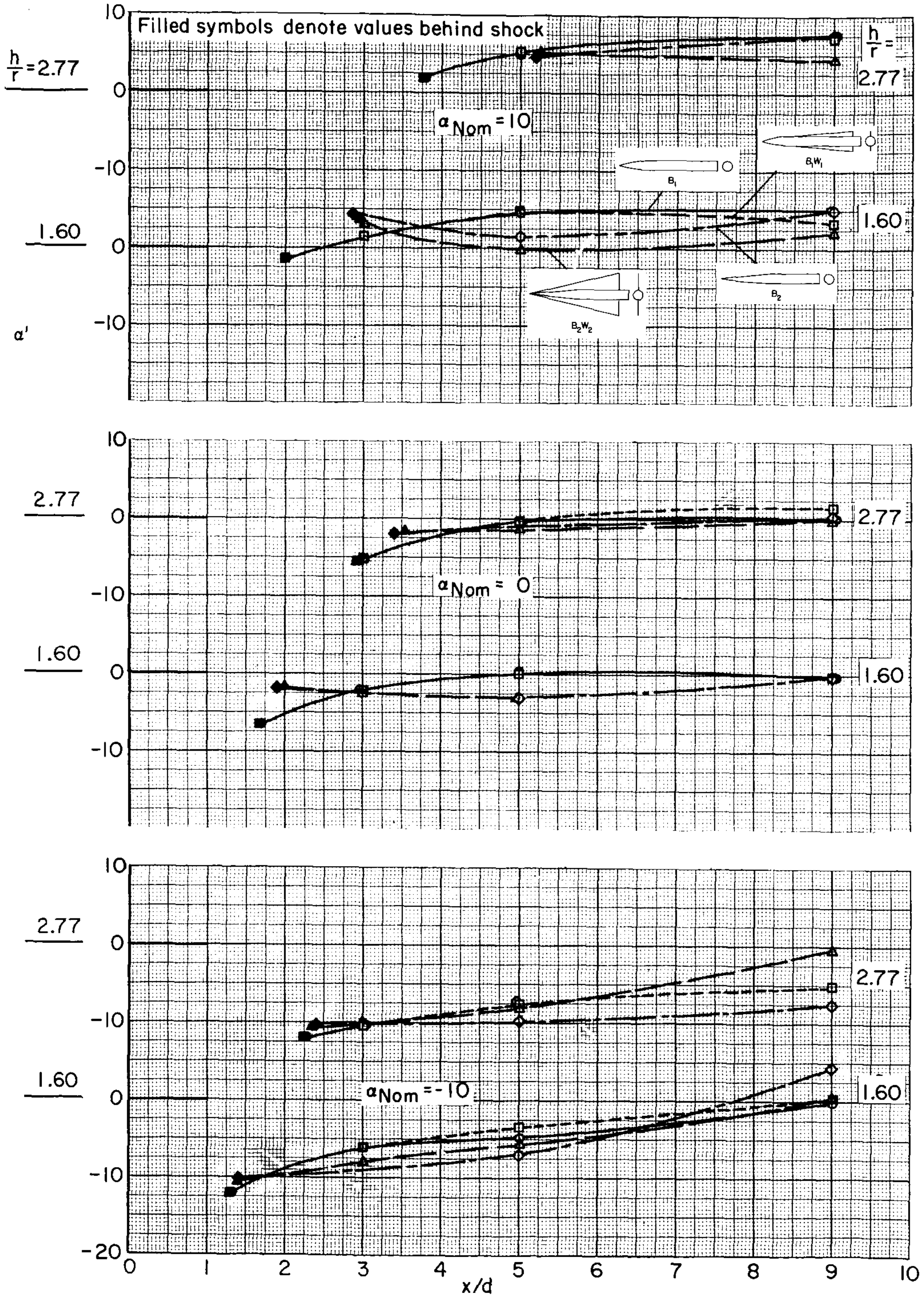

(c) Local angle of attack.

Figure 26.- Concluded.

[redacted]

[redacted]

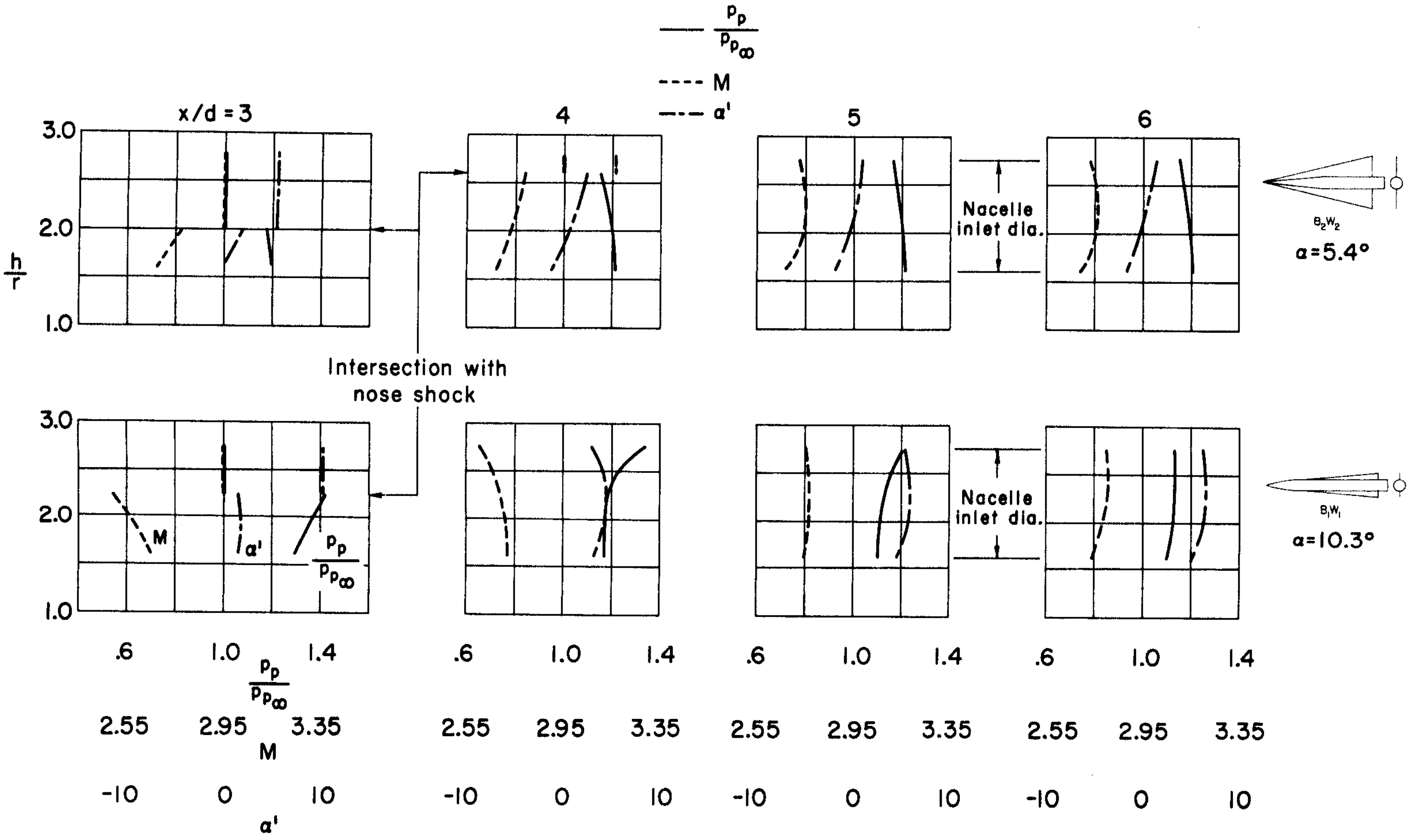

Figure 27.- Comparison of flow characteristics in vertical plane of symmetry of B_1W_1 and B_2W_2 at angles of attack corresponding to maximum lift-drag ratio; $M_\infty = 2.95$ and $\beta = 0^\circ$.

[redacted]

[redacted]

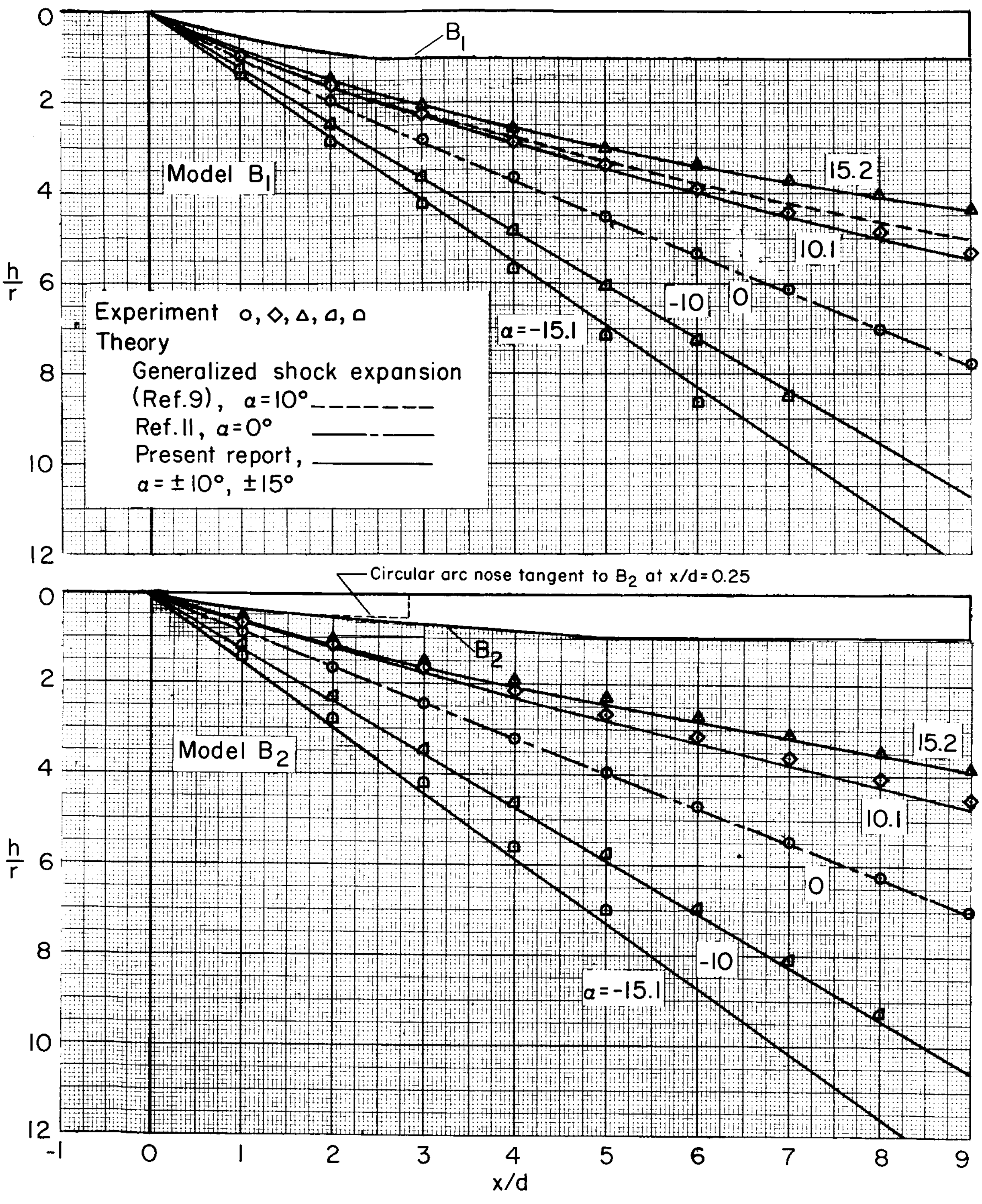

Figure 28.- Comparison of calculated and experimental shock-wave coordinates in vertical plane of symmetry below the bodies alone for $\beta = 0^{\circ}$ and $M_{\infty} = 2.95$.

[redacted]

[redacted]

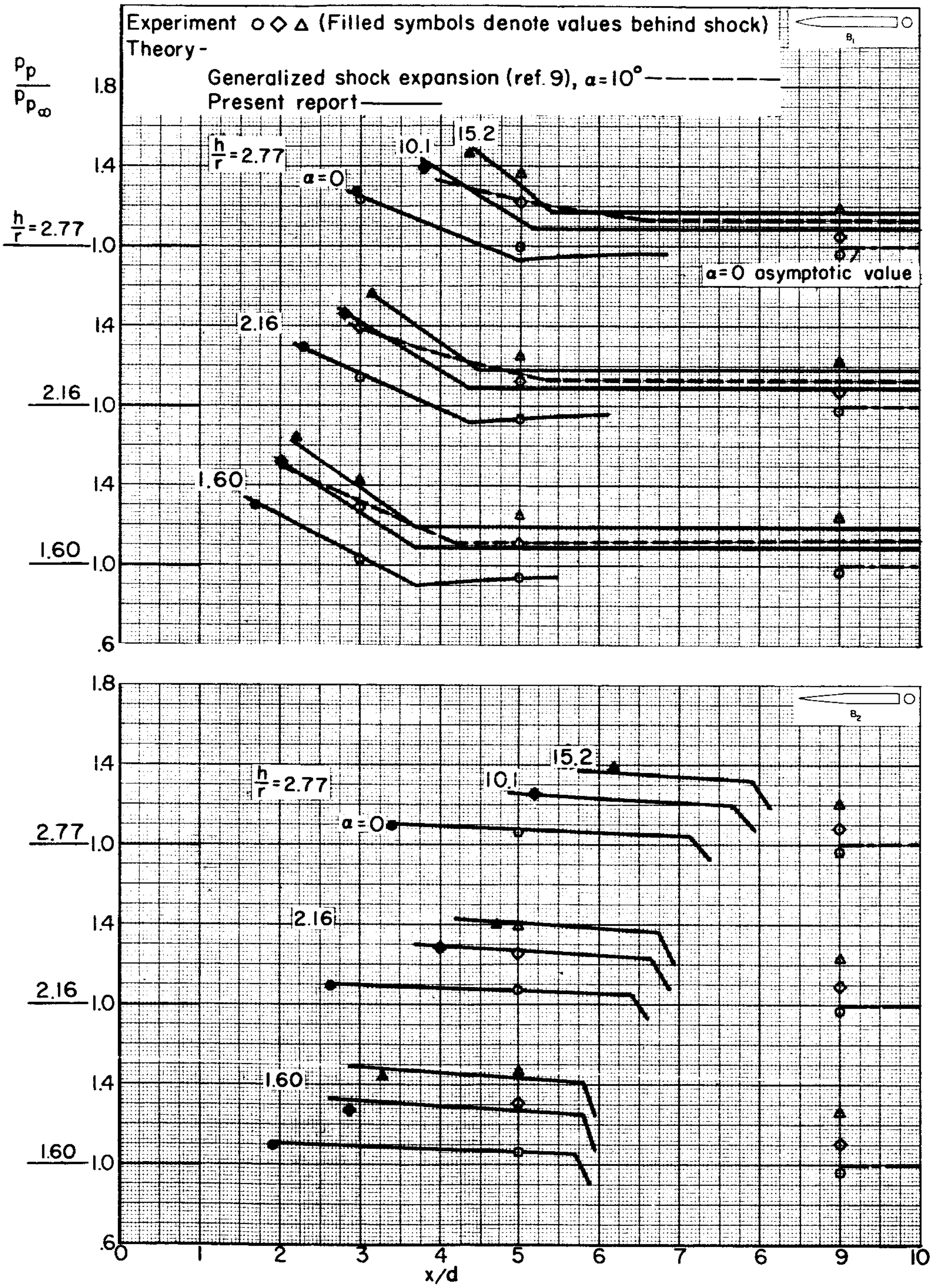

(a) Pitot-pressure ratio.

Figure 29.- Comparison of calculated and experimental flow characteristics in vertical plane of symmetry of bodies alone for $\beta = 0^\circ$ and $M_\infty = 2.95$.

[redacted]

[redacted]

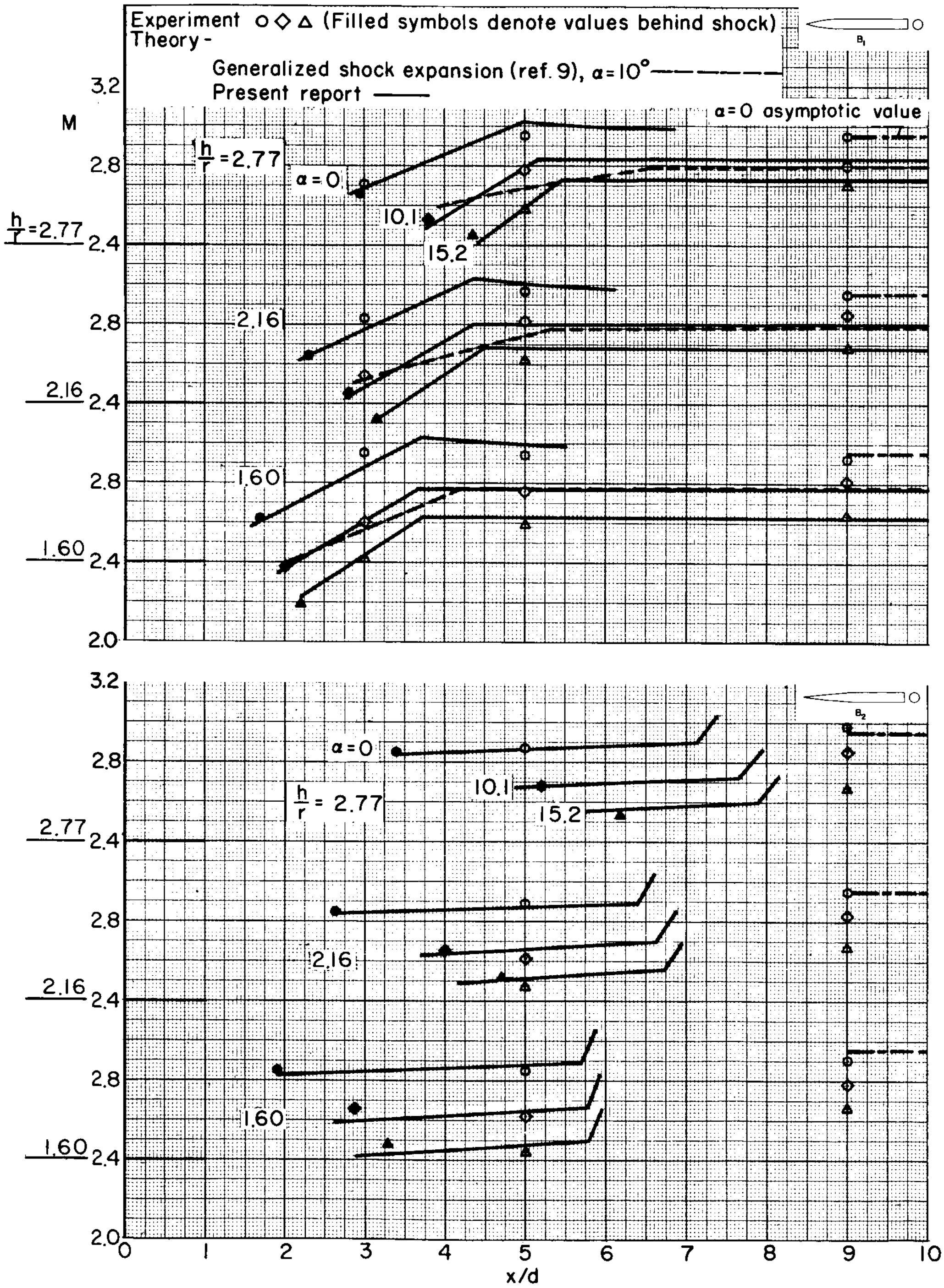

(b) Mach number.

Figure 29.- Concluded.

[redacted]